



UNIVERSITÀ DEGLI STUDI ROMA TRE  
Facoltà di Scienze Matematiche, Fisiche e Naturali  
Dipartimento di Fisica “E. Amaldi”  
**Dottorato di Ricerca in Fisica XXV Ciclo**

---

## **The complex environment of AGN**

Andrea Marinucci

---

Relatori:  
Prof. Giorgio Matt  
Dott. Stefano Bianchi

Gennaio 2013

---

---

# Contents

<b>Introduction</b>	<b>1</b>
<b>1 Active Galactic Nuclei and their environment</b>	<b>5</b>
1.1 Classification of AGN . . . . .	5
1.1.1 Seyfert Galaxies . . . . .	7
1.2 Fueling the central engine . . . . .	7
1.2.1 Accretion efficiency . . . . .	9
1.2.2 The accretion disc . . . . .	10
1.2.3 Eddington Luminosity . . . . .	10
1.2.4 Radiatively-inefficient discs . . . . .	11
1.3 Geometry of the inner structure: is the Unification Model still valid?	11
1.3.1 Alternative Models . . . . .	13
1.4 The continuum emission . . . . .	16
1.4.1 Optical/UV . . . . .	16
1.4.2 Infrared . . . . .	17
1.4.3 Radio . . . . .	19
1.4.4 X-rays . . . . .	19
1.5 Signatures of the circumnuclear environment . . . . .	22
1.5.1 The reflection component . . . . .	24
1.5.2 The Iron $K\alpha$ . . . . .	25
1.6 The profile of the Iron Line . . . . .	29
1.7 Ionized absorption . . . . .	30
1.8 Soft X-ray emission in obscured sources . . . . .	32
1.9 Column density variability . . . . .	34
<b>2 The link between the Hidden Broad Line Region and the accretion rate</b>	<b>35</b>
2.1 The Sample . . . . .	36
2.1.1 The BH mass sub-selection . . . . .	36
2.1.2 The X-ray Sub-Selection and the Final Sample . . . . .	39
2.2 Data Analysis . . . . .	39

2.2.1	X-ray Data Reduction and Analysis . . . . .	39
2.2.2	Nuclear 2-10 keV Luminosity for Compton-Thick Sources	42
2.2.3	Bolometric Luminosities and Eddington Ratios . . . . .	44
2.3	Results . . . . .	46
2.3.1	Comparison with other Works and Methodologies . . . . .	46
2.4	Discussion on the origin of the BLR . . . . .	49
<b>3</b>	<b>The circumnuclear geometry of Sy2 galaxies</b>	<b>55</b>
3.1	The Compton-thick Sy2 NGC 4945 . . . . .	56
3.1.1	Observations and data reduction . . . . .	57
3.1.2	The reflector geometry from time and spectral variability .	58
3.1.3	The reflector geometry from direct imaging . . . . .	62
3.1.4	The structure of the innermost regions . . . . .	66
3.2	The Compton-thin Sy2 NGC 4507 . . . . .	66
3.2.1	Observations and data reduction . . . . .	67
3.2.2	Data analysis . . . . .	67
3.2.3	Discussion on the column density variability . . . . .	72
3.2.4	The circumnuclear environment . . . . .	79
<b>4</b>	<b>Conclusions</b>	<b>81</b>
<b>5</b>	<b>Future perspectives</b>	<b>87</b>
<b>A</b>	<b>X-ray Satellites</b>	<b>95</b>
A.1	XMM-Newton . . . . .	95
A.2	Chandra . . . . .	96
A.3	Suzaku . . . . .	99
A.4	Swift . . . . .	101
	<b>Acknowledgements</b>	<b>103</b>
	<b>References for this thesis</b>	<b>105</b>

# Introduction

A few percent of bright galaxies host an active nucleus with emission due to non-stellar processes: they are called Active Galactic Nuclei (AGN) and are powered by accretion of matter onto a supermassive black hole (ranging from  $10^6 - 10^9$  solar masses). Accretion occurs via an accretion disc that efficiently converts gravitational energy into radiation.

Seyfert galaxies are a sub-class of the wide variety of AGN. A further classification is based on their optical/UV spectra: broad and narrow emission lines are both present in Seyfert 1s while only the latter are visible in Seyfert 2s.

The standard Unification Model for AGN assumes the same internal structure for both Seyfert 1 and Seyfert 2 galaxies (Antonucci 1993), with all observational differences ascribed to an axisymmetric distribution of gas, located between the Broad Line Region (BLR) and the Narrow Line Region (NLR), in order to obscure the former, but not the latter. A natural geometrical and physical scenario is that of a homogeneous torus on a parsec scale (Krolik & Begelman 1988). If the so-called torus intercepts our line of sight the primary emission and the BLR are obscured with a resulting lack of broad lines in the optical/UV spectrum and a classification as Seyfert 2. On the contrary, if the nucleus is unobscured, the source is classified as a Seyfert 1 and every component of the spectrum is visible. This scenario came into existence after the discovery of polarized broad permitted emission lines in the optical/UV spectrum of one of the brightest Seyfert 2 galaxies, NGC 1068 (Antonucci & Miller 1985; Miller & Antonucci 1983), suggesting a geometry in which: (a) BLRs are confined in a relatively small region ( $\sim$  light-days) surrounding the central source, (b) their direct view (in Seyfert 2s) is obscured by a flat distribution of distant material coplanar with the disc-plane, and (c) their line emission is Compton-scattered into the line of sight by a population of warm electrons extending at large radii above and below the accretion disc.

A further discrimination among Seyfert 2 galaxies is based on the column density of the absorbing circumnuclear material in the torus ( $N_H$ ): Compton thick ( $N_H > 10^{24} \text{cm}^{-2}$ ) and Compton thin ( $N_H < 10^{24} \text{cm}^{-2}$ ) AGN. The latter class of objects have an observed flux much higher than the former one because the circumnuclear material becomes transparent to the radiation in the 2-10 keV band.

In the X-ray spectra the reprocessing of the primary emission from the circumnuclear gas gives origin to a cold neutral reflection of the nuclear radiation and emission lines, in particular the neutral Fe  $K\alpha$ .

However in the past few years, exceptions to orientation-based unification models have been found, suggesting the possibility that not all Seyfert 2 galaxies host a Seyfert 1 nucleus. Indeed, spectropolarimetric surveys find that only about 50% of the brightest Seyfert 2 galaxies show hidden broad-line regions (HBLR) in their optical-polarimetric spectra (Tran 2001, 2003). Several authors have suggested that the presence of BLRs in Seyfert 2s can be linked to the luminosity of the active nucleus, and may disappear at low luminosities (Lumsden & Alexander 2001; Laor 2003; Elitzur & Ho 2009), or low accretion rates (Nicastro 2000). In both cases, the presence of the BLR is not an inescapable feature of all Seyfert galaxies, as postulated by the unification model, but it is tightly linked to a physical parameter of the AGN, either the luminosity or the accretion rate.

Furthermore, recent studies on X-ray absorbing column density changes performed with *Chandra*, *XMM-Newton* and *Suzaku* satellites ruled out a universal geometrical structure of the circumnuclear absorber, as postulated by the Unified Model. Absorption variability has been found to be common (almost ubiquitous) when we compare observations months to years apart (Risaliti 2002), and, most notably, on time scales of hours to days in several sources, such as NGC1365 (Risaliti et al. 2005, 2007, 2009), NGC 4388 (Elvis et al. 2004), NGC 4151 (Puccetti et al. 2007) and NGC 7582 (Bianchi et al. 2009).

In the framework of this complex scenario, my work will be focused on the connection between the Hidden Broad Line Region and the accretion rate in Seyfert 2 galaxies and on the study of the geometrical structure of two galaxies that showed very peculiar characteristics in their spectral properties. In particular, I will address two different, complementary, approaches to study the circumnuclear medium of AGN: a statistical analysis of a small sample of both Compton Thin and Compton Thick Seyfert 2 galaxies and via a detailed X-ray spectral investigation of two among the brightest Seyfert 2 galaxies known.

With concern to the former topic we will use the observed X-ray (2-10 keV) continuum emission as a direct probe of the AGN activity. We select a sample of type 2 Seyfert galaxies with good quality spectropolarimetric and X-ray observations, for which we can give a good estimate of the mass of the central supermassive black hole. By doing so, we find evidence suggesting that accretion rate is the main parameter that sets the existence of HBLRs in Seyfert 2 galaxies, confirming the model presented by Nicastro (2000) and suggesting a revision of the Unified Model.

Then we will investigate the geometrical structure of the circumnuclear environment in two nearby Seyfert 2 galaxies: NGC 4945 and NGC 4507. We will perform a time, spectral and imaging analysis of the X-ray inner structure of NGC

4945, which reveals its geometrical and physical properties with unprecedented detail. NGC 4945 hosts one of the brightest AGN in the sky above 10 keV, but it is only visible through its reflected/scattered emission below 10 keV, due to absorption by a column density of  $N_H \simeq 4 \times 10^{24} \text{cm}^{-2}$ . A new *Suzaku* campaign of 5 observations spanning 6 months, together with past XMM-*Newton* and *Chandra* observations, show a remarkable constancy (within 10%) of the reflected component. Instead, Swift-BAT reveals strong intrinsic variability on time scales longer than one year. We show that the reflector is at a distance  $> 30\text{-}50$  pc, well within the imaging capabilities of *Chandra* at the distance of NGC 4945. Indeed, the *Chandra* imaging reveals a resolved, flattened, 150 pc-long clumpy structure, whose spectrum is fully consistent with cold reflection of the primary AGN emission. The clumpiness may explain the small covering factor derived from the spectral and variability properties. This study provides evidence for absorption variability at a parsec-scale distance and proves the fundamental importance of a broadband X-ray study of AGN.

We will then present a spectral analysis of an XMM-*Newton* and *Chandra* campaign of the obscured AGN in the Seyfert 2 galaxy NGC 4507, consisting of six observations spanning a period of six months. Using the *Epic* and the ACIS-S CCD cameras, we can detect strong absorption variability on time scales between 1.5 and 4 months in the circumnuclear material through a very detailed spectral analysis. The variation of the absorbing column density is the first one ever observed on these time scales for this source and it suggests that the obscuring material consists of gas clouds at parsec-scale distance. The lack of variability on shorter time scales rules out the possibility of absorption by broad line region clouds, which was instead found in other studies of similar sources. This shows that a single, universal structure of the absorber (either BLR clouds, or the parsec-scale torus) is not enough to reproduce the observed complexity of the X-ray absorption features of (at least) these two AGN.

This thesis is divided as follows:

- **Chapter 1:** a general view on Active Galactic Nuclei and Seyfert Galaxies is presented, with a description of the physics of accretion that fuels this peculiar class of galaxies and determines their emission. Particular emphasis will be placed on the components arising from the reprocessing of the X-ray primary continuum from the circumnuclear matter, since it is the main focus of this work;
- **Chapter 2:** the contribution of this work to the subject of a revision of the Unification Model of AGN will be presented, with a detailed description of our study on the relation between the accretion rate and the presence of polarized broad lines in Seyfert 2 galaxies;



- **Chapter 3:** the investigation of the circumnuclear structure of AGN will be described, through the X-ray spectral analysis of two bright galaxies, namely NGC 4945 and NGC 4507;
- **Chapter 4:** a discussion on the results of this work and their outcomes on the orientation-based Unification Model of AGN will be presented;
- **Chapter 5:** future perspectives on the investigation of the complex circumnuclear environment of AGN will be discussed.

# Chapter 1

## Active Galactic Nuclei and their environment

### 1.1 Classification of AGN

The term Active Galactic Nuclei (AGN) indicates the compact and inner regions, ranging from a few hundreds of parsecs down to the sub-parsec, of a few percent of bright galaxies whose energetic phenomena cannot be attributed to stellar processes.

A supermassive black hole (ranging from  $10^6 - 10^9$  solar masses) is present at the center of the nucleus, surrounded by an accretion disc that efficiently converts gravitational energy into radiation.

Indeed, this definition includes a wide variety of phenomenology. The resulting classification is very complex and is mainly based on luminosity, electromagnetic spectrum and spatial morphology.

A first classification comes from two main parameters of the spectrum of an AGN:

1. **Radio Emission:** AGN show a large distribution of radio ( $L_R$ ) and optical ( $L_O$ ) luminosities with a bimodal distribution of the ratio between the two luminosities, with  $\frac{L_R}{L_O} \sim 10$  as the dividing value. Objects below this value are called Radio-Quiet AGN, sources with a  $\frac{L_R}{L_O} > 10$  are indicated as Radio-Loud AGN. This last class of galaxies is 10-15% of the total. The intense radio emission in Radio-Loud AGN is believed to be related with the presence of relativistic, collimated flows of matter (jets). Since I will investigate only radio-quiet objects in this thesis, in the following I will focus on the characteristics of this subclass.

2. **Emission lines:** in the optical/UV spectrum of AGN emission lines much more intense and broader than in usual galaxies are usually present. They can be divided into:
  - Broad Emission Lines: lines corresponding to permitted transitions with FWHM of thousands of  $\text{km s}^{-1}$ ;
  - Narrow Emission Lines: lines from permitted and forbidden transitions with FWHM of hundreds of  $\text{km s}^{-1}$

Broad lines observed in the optical/UV spectra of Seyfert Galaxies have typical widths of  $\approx 5000 \text{ km s}^{-1}$ , but can be as large as  $10\,000 \text{ km s}^{-1}$  or more. Such widths are interpreted as being due to the keplerian velocities of a large number of clouds (the Broad Line Region: BLR) rotating around the BH at a distance of 0.01-0.1 pc (see figure 1.1). The density of this gas is believed to be very high, of the order of  $10^9 - 10^{11} \text{ cm}^{-3}$ , as required by the observed ratio between forbidden and permitted emission transitions. Still under debate is the origin of these clouds and several models have been proposed, see Sect. 1.3. The narrow lines have much smaller widths, typically a few times  $100 \text{ km s}^{-1}$ . This is easily explained if they are produced by gas (the Narrow Line Region: NLR) farther away from the BH, extending on the 100 pc scale (see figure 1.1), as often directly observed in the images. The gas has a density of  $10^3 - 10^6 \text{ cm}^{-3}$ , lower than that required for the BLR and low enough to explain the presence of forbidden lines. It is likely composed by the inner part of the Galactic disc, photoionized by the nuclear continuum (Bianchi et al. 2006; Bianchi & Guainazzi 2007).

A further classification depends on the presence or absence of Broad Emission Lines. Two different class of sources can be introduced:

1. Type 1 AGN: Broad Emission Lines and Narrow Emission Lines are both present in the optical spectrum;
2. Type 2 AGN: only narrow emission lines are present.

The column density of the absorbing matter around the central nucleus ( $N_{\text{H}}$ ) can be used as a further classification criterium:

1. Obscured AGN: evidence of intrinsic cold absorption in the X-ray band in excess to that due to the Milky Way;
2. Unobscured AGN: there is no excess cold absorption in the X-ray band.

A good correlation between this classification and the previous one is observed: type 2 AGN are usually absorbed, while type 1 AGN are not. Among the unobscured AGN a further discrimination can be introduced: even if classified as

## 1.2. Fueling the central engine

---

type 2 AGN, these objects have a nuclear luminosity which may not completely be absorbed in X-rays by the circumnuclear material. The following classification is based on the column density of the absorbing circumnuclear material in the torus ( $N_H$ ):

- **Compton Thin sources:** present a typical  $N_H < 10^{24} \text{ cm}^{-2}$ . They have a nuclear flux much higher than a Compton Thick object's one because the circumnuclear material is transparent to the radiation in the 2-10 keV band.
- **Compton Thick sources:** present a typical  $N_H > 10^{24} \text{ cm}^{-2}$ . Most of the radiation coming from the inner part of the galaxy is absorbed by the torus.

### 1.1.1 Seyfert Galaxies

This class of AGN shows a nuclear luminosity not exceeding the host galaxy's one,  $L < 10^{44} \text{ erg/s}$ .

Most of Seyfert galaxies are nearby ( $z < 0.1$ ) spiral galaxies (Adams 1977). From a spectroscopic point of view they show strong emission lines and faint absorption lines.

Like all other AGN Seyfert Galaxies are divided in two subclasses based on their optical/ UV spectra: Seyfert 1s show both broad and narrow emission lines, while only narrow lines are visible in Seyfert 2s, with intermediate classifications of 1.0, 1.2, 1.5 and 1.8, 1.9 and 2.0 .

The Unification Model (Antonucci 1993) postulates that the two classes are intrinsically the same, their observational differences being solely due to the presence of cold, absorbing gas along the line of sight. This material is usually supposed to be a molecular torus surrounding the accretion disc and the Broad Line Region (BLR). If the torus intercepts the line of sight, the primary emission is obscured and broad lines are invisible: only narrow lines, produced outside the torus, are present in the spectrum, leading to a classification as a Seyfert 2. Otherwise, every component of the spectrum is visible and the source is classified as a Seyfert 1.

## 1.2 Fueling the central engine

One of the main characteristics of AGN is their extreme luminosities, typically ranging between  $10^{42}$  and  $10^{48} \text{ erg s}^{-1}$  and produced in a very small region. Since the first quasar's (3C 273) redshift was measured in 1963 by Marteen Schmidt (Schmidt 1963) great efforts have been spent in understanding what mechanisms could be involved in producing such a great amount of radiation in such compact regions, without exceeding the Eddington luminosity to keep the process effective.

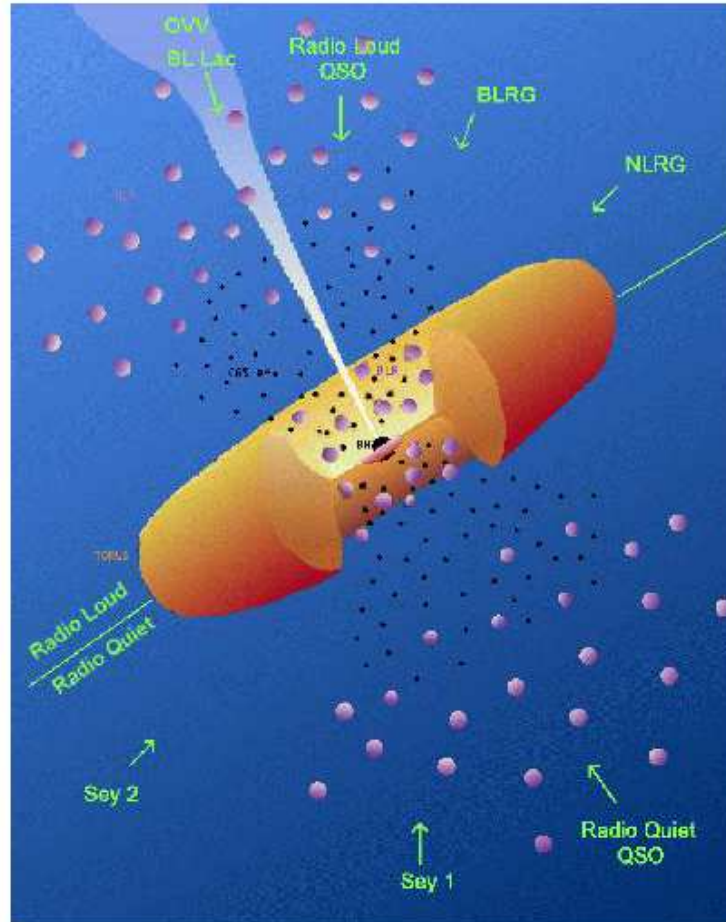


**Figure 1.1:** A cartoon illustrating the Unification Model. Credit: M. Polletta, Laurea Thesis, 1996, adapted from Urry and Padovani, 1995

The extreme compactness ( $M/R$ ) of the nuclei of active galaxies leads almost unambiguously to postulate the presence of supermassive black holes (SMBHs), in the range  $10^6 - 10^9 M_{\odot}$ .

In the following we will discuss the process of accretion, thought to be responsible for fueling the central engine of AGN and compact systems in general, through the conversion of gravitational energy into radiation.

### 1.2.1 Accretion efficiency

The mechanism of accretion on a supermassive black hole should be very efficient in order to produce such high luminosities in active galaxies. If the energy is converted so that  $E = \eta mc^2$ , the efficiency  $\eta$  needs to be very high. If we consider the standard nuclear processes that fuel stars we can only reach a maximum value of  $\eta = 0.007$ , in the case of Hydrogen burning. In the following we will show that the process of accretion can reach  $\eta = 0.42$ .

Let us consider an object with mass  $m$  which is falling onto a much more massive body with mass  $M$ . If the object of mass  $m$  is in a free-falling regime from infinity it gains kinetic energy at the expense of gravitational energy. If we consider a proton with mass  $m_p$  :

$$\frac{1}{2}m_p v_{ff}^2 = \frac{GMm_p}{r} \quad (1.1)$$

When matter reaches the surface of the compact object kinetic energy is transformed into heat, with a consequent irradiation. If the accretion rate is  $\dot{m}$ , the kinetic energy dissipation is  $\frac{1}{2}\dot{m}v_{ff}^2$  and hence the luminosity,  $L = \frac{dE}{dt}$  is:

$$L = \frac{1}{2}\dot{m}v_{ff}^2 = \frac{GM\dot{m}}{r}. \quad (1.2)$$

It is convenient to introduce the Schwarzschild's radius for an object with mass  $M$ :

$$r_s = \frac{2GM}{c^2}, \quad (1.3)$$

which corresponds roughly to  $3 \times 10^{13}$  cm or 0.01 light days for a  $10^8 M_\odot$  black hole. Inserting  $r_s$  in the expression 1.2 we get:

$$L = \frac{1}{2}\dot{m}c^2\left(\frac{r_s}{r}\right) \quad (1.4)$$

Defining  $\frac{r_s}{2r} = \eta$ , then:

$$L = \eta \dot{m} c^2. \quad (1.5)$$

It would then seem natural to assume that the accretion efficiency reaches its higher values in the vicinity of a BH. However, this is not necessarily true, because BHs do not have a surface and the accretion mechanism must be induced by the presence of an accretion disc of gas rotating around the BH.

The value of the efficiency factor  $\eta$  is of the order of 0.1 for a neutron star and it is very easy to show that it is proportional to the compactness of the hidden object. Considering a spinning BH, with a non null angular momentum, the accretion takes place not beyond the so called 'radius of marginal stability'  $r_{ms}$ . Since  $r_{ms}$  in a Kerr metric is strongly dependent from the BH spin we have  $\eta \simeq 0.06$  for a

non-rotating BH and  $\eta \simeq 0.42$  for a maximally rotating BH. We refer the reader to Shapiro & Teukolsky (1983) for a very elegant mathematical approach.

### 1.2.2 The accretion disc

Accretion via a disc consists in the extraction of energy and angular momentum from a distribution of matter gravitating around a central body by letting it slowly spiraling inwards. An accretion disc configuration can fully describe the loss of angular momentum and the conversion of gravitational energy into radiation. The main physical driver of such phenomenon is the viscosity arising from the differential rotation in the annuli of the disc. This topic has been widely discussed and debated in the past, presented for the first time by Shakura & Sunyaev (1973) and reviewed by Pringle (1981) some years later. We will refer mainly to these works in the following sections.

### 1.2.3 Eddington Luminosity

In order to have a stable system, the outward force due to the radiation pressure cannot exceed the inward gravitational force. The outflowing flux of energy at a distance  $r$  is  $F = L/4\pi r^2$ , where  $L$  is the luminosity (erg/s) of the source. Since the momentum of a photon with energy  $E = h\nu$  is  $p = E/c$ , the total outflowing momentum will be:

$$P_{rad} = \frac{F}{c} = \frac{L}{4\pi r^2 c}.$$

The outward radiation force on a single photon can be obtained multiplying  $P_{rad}$  times the interaction cross section of the photon:

$$F_{rad} = \sigma_e \frac{L}{4\pi r^2 c} \quad (1.6)$$

where  $\sigma_e$  is the Thomson cross section. The gravitational force on a proton-electron couple by an object with mass  $M$  is:

$$F_{grav} = \frac{-GM(m_p + m_e)}{r^2} \approx \frac{-GMm_p}{r^2}. \quad (1.7)$$

Since the gravitational force acting on the gas has to balance or exceed the outflowing radiation force to keep the system stable, from equation 1.6 and 1.7 we have:

$$\begin{aligned} |F_{rad}| &\leq |F_{grav}| \\ \sigma_e \frac{L}{4\pi r^2 c} &\leq \frac{GMm_p}{r^2} \end{aligned}$$

### 1.3. Geometry of the inner structure: is the Unification Model still valid?

---

$$L_{\text{Edd}} \leq \frac{4\pi G c m_p}{\sigma_e} M \approx 1.26 \times 10^{38} (M/M_\odot) \text{ erg/s} \quad (1.8)$$

The equation 1.8 is known as *Eddington luminosity* and it can be used to determine the minimum mass ( $M_{\text{Edd}}$ ) to produce a luminosity  $L_{\text{Edd}}$ . The Eddington luminosity can also be interpreted as the maximum luminosity of a source with mass  $M$  fueled by a spherical accretion.

#### 1.2.4 Radiatively-inefficient discs

A fundamental parameter is the accretion rate  $\dot{m}$  in the so-called standard model for accretion discs (Eq. 1.5). The physical scenario for accretion discs, presented in Shakura & Sunyaev (1973), stands true for accretion rates not too high or too low with respect to the critical value  $\dot{m}_{\text{cr}}$  (typically ranging between 0.1-1  $\dot{m}_{\text{cr}}$ ), corresponding to the Eddington luminosity. The fact that black holes do possess an event horizon instead of a hard surface leads to a family of solutions where a significant fraction of the dissipated energy  $D(R)$  is advected through the event horizon. Among this class we find Advection Dominated Accretion Flows (ADAFs: Ichimaru 1977; Abramowicz et al. 1995) models, also used to explain the emission from the Galactic Center (Narayan et al. 1995). The radiative efficiency  $\eta$  becomes rather low in both cases where  $\dot{m} \ll \dot{m}_{\text{cr}}$  or  $\dot{m} \gg \dot{m}_{\text{cr}}$ . In the former case the accretion rate is sufficiently small that the inflowing gas has low density and it is unable to cool down, all the energy resides in the ions and the coupling to electrons is so weak that very little radiation is emitted. In the latter case the accretion rate and gas density are so high that the flow is extremely optically thick and radiation cannot escape, being dragged down the black hole, producing a sub-Eddington luminosity.

### 1.3 Geometry of the inner structure: is the Unification Model still valid?

The unification model for active galactic nuclei (AGN) invokes a paradigm for Seyfert 2 and Seyfert 1 galaxies (Antonucci 1993) in which two different types of galaxies are believed to be intrinsically the same but differ, observationally, due to orientation effects only: Seyfert 1 galaxies are observed at low angles (face-on) while Seyfert 2 galaxies are seen edge-on through large column densities of obscuring material, which prevent the direct view of the nuclear regions of these sources.

This scenario was first proposed after the discovery of polarized broad permitted



emission lines in one of the brightest Seyfert 2 galaxies, NGC 1068 (Antonucci & Miller 1985; Miller & Antonucci 1983), suggesting a geometry in which:

- BLRs are confined in a relatively small region ( $\sim$  light-days) surrounding the central source;
- their direct view (in Seyfert 2s) is obscured by a flat distribution of distant material coplanar with the disc-plane;
- their line emission is Compton-scattered into the line of sight direction by a population of hot electrons extending at large radii above and below the accretion disc.

The key ingredient in such a model is therefore the geometrical structure of the obscuring medium. The need for a axisymmetric, toroidal structure of the absorber was initially inferred from the polarization of the reflected broad lines and from the measured polarization angles. If we had a simple cloud along the line of sight, reflection should come from all directions and hence the total polarization should be zero, by averaging from all angles. To break the symmetry of the polarization angles the absorbing structure should prevent the nuclear light to be scattered in a significant range of angles: a "torus" is the natural configuration that can take into account this effect (Fig. 1.1).

The size of the toroidal absorber was initially postulated to be on the parsec scale (Krolik & Begelman 1988). Such typical size was simply inferred by the need for the absorber to be large enough to obscure the BLR, which in Seyfert nuclei has a size well below a parsec, but small enough not to obscure the Narrow Line Region (NLR), which is distributed on the 10-100 pc scale. If the origin of the NLR can be ascribed to photoionization from the nuclear UV/X ray continuum hidden from our line of sight from the torus we should expect it to have a biconical morphology (Pogge 1988; Tadhunter & Tsvetanov 1989). Indeed, high resolution and narrow band imaging revealed such ionization cones in many nearby AGN (e.g. Wilson & Tsvetanov 1994; Bianchi et al. 2007; Barbosa et al. 2009, and references therein). The opening angle of the cones gives the fraction of the sky hidden to our line of sight, which is roughly in agreement with what inferred from the relative fraction between type 1 and type 2 AGN in the local universe (Maiolino & Rieke 1995). Since the first seminal models proposed to describe the physics of the toroidal absorbing medium many theoretical works have been proposed to reproduce all the observable properties. Instead of assuming a simple uniform distribution of gas and dust within a parsec-scale radius (e.g Krolik & Begelman 1988; Pier & Krolik 1992) alternative models suggested more extended geometries, up to 100 pc, to explain the observed infrared spectral energy distribution (Granato et al. 1997). Recently the hypothesis of a uniform gas and dust distribution has been revised,

### 1.3. Geometry of the inner structure: is the Unification Model still valid?

in favor of a clumpy structure of the absorbing material (Fig. 1.2 and Elitzur & Shlosman 2006; Nenkova et al. 2008; Hönig & Kishimoto 2010).

While the presence of non-spherically symmetric absorbers as explanation for the type 1/type 2 dichotomy remains still valid, throughout the years observational evidence showed that the geometry of the absorbing material is much more complex than the one postulated by the Unification Model. A uniform, single absorbing medium is likely not enough to explain all the observational features of a AGN and hence multiple absorbers should be present around the central source, possibly distributed on different physical scales.

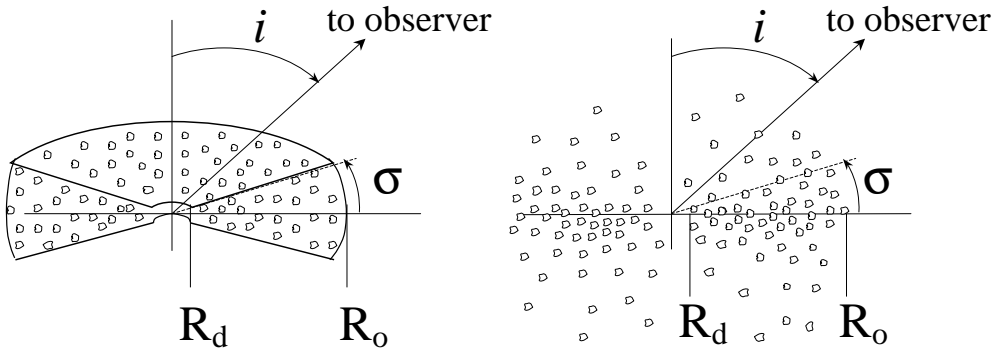


**Figure 1.2:** On the left panel the clumpy model for dust clouds with individual optical depth  $\tau$ , in a fixed toroidal volume is shown. The inner radius ( $R_d$ ) is determined by the dust-sublimation temperature. On the right panel the clumpy model where the dust clouds are not bound in a fixed volume is shown. For this particular geometry, there is a small, non-zero probability that a dust cloud may obscure the BLR when the incident angle of the observer is  $i=0$ . Figure adapted from Nenkova et al. (2008).

#### 1.3.1 Alternative Models

The important successes of Unified Models, together with the existence of a number of observational data which remain to be explained, justify all the efforts that have been spent to propose a number of alternatives. Among them, one of the most promising is the one discussed by Elvis (2000). In the proposed scenario, gas is thrown off the accretion disc vertically in a narrow band of radii. As this wind is hit by the inner primary radiation it bends radially outward, forming a funnel-shaped thin flow that can substitute the torus and offers this possibility to explain many other features observed in AGN (see Fig. 1.3). In order to produce

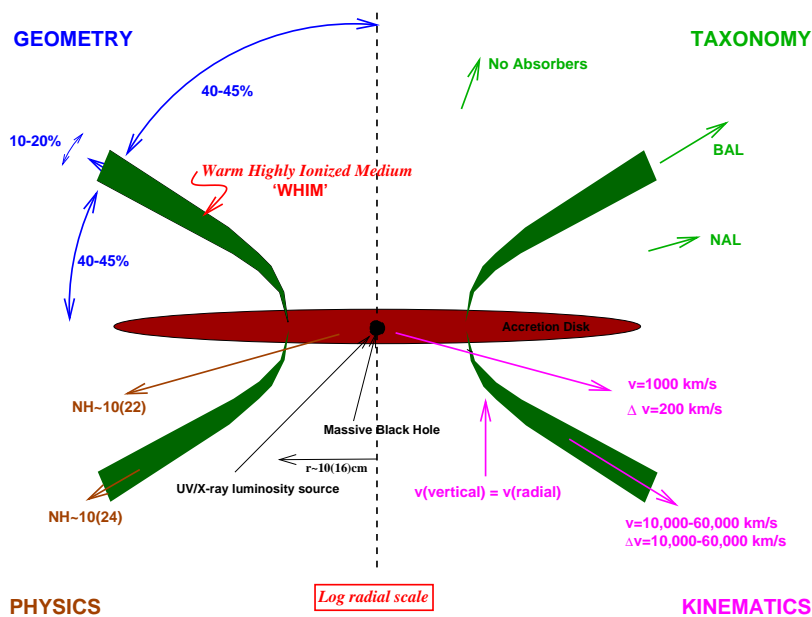


**Figure 1.3:** A cartoon depicting the alternative Unification Model proposed by Elvis (2000). The figure is divided in four quadrants which illustrate (clockwise from top left): the geometrical angles involved in the structure, the resulting classification for a distant observer, the outflow velocities for each line of sight and typical radii and column densities (from Elvis 2000).

them, the wind, arising radially from the disc, should bend outward to a cone angle of  $\approx 60$  deg with a divergence angle of  $\approx 6$  deg, ensuring a covering factor of  $\approx 10\%$ .

Several other exceptions to orientation-based unification models have been found in the past few years, suggesting the possibility that not all Seyfert 2 galaxies host a Seyfert 1 nucleus. Indeed, spectropolarimetric surveys find that only about 50% of the brightest Seyfert 2 galaxies show hidden broad-line regions (HBLR) in their optical-polarimetric spectra (Tran 2001, 2003). Several authors have suggested that the presence of BLRs in Seyfert 2s can be linked to the luminosity of the active nucleus, and may disappear at low luminosities (Lumsden & Alexander 2001; Tran 2001; Gu & Huang 2002; Martocchia & Matt 2002; Tran 2003; Laor 2003; Elitzur & Ho 2009) or low accretion rates (Nicastro 2000; Nicastro et al. 2003; Czerny et al. 2004). In both cases, the presence of the BLR is not an inescapable feature of all Seyfert galaxies, as postulated by the unification model, but it is tightly linked to a physical parameter of the AGN, either the luminosity or the accretion rate.

One interesting model is the one proposed by Nicastro (2000). He proposed that

### 1.3. Geometry of the inner structure: is the Unification Model still valid?

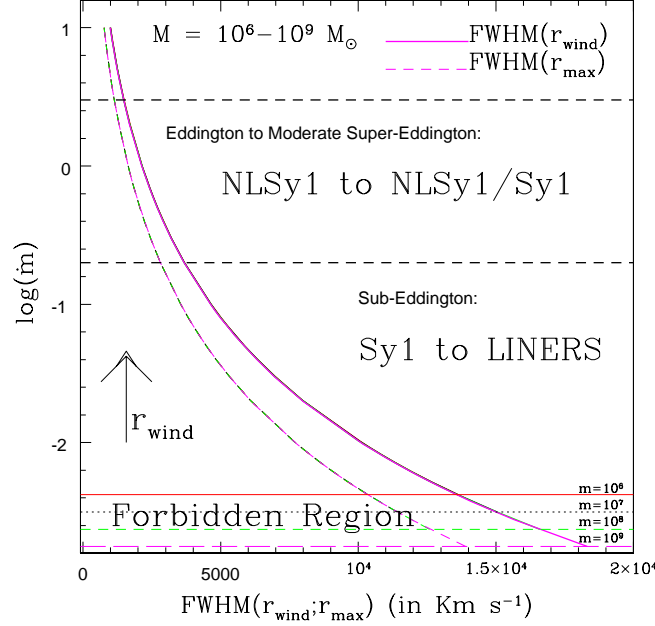


**Figure 1.4:** The relationship between the accretion rate (in the range  $\dot{m}_{\text{min}}(m) - 10$ ) and the expected  $\text{FWHM}(r_{\text{wind}})$  (solid, thick curves) and  $\text{FWHM}(r_{\text{max}})$  (dashed, thin curves), for  $m = 10^6, 10^7, 10^8, 10^9$  is shown. At the bottom of the plot the four horizontal lines indicate these values of  $\dot{m}_{\text{min}}(m)$ , from (Nicastro 2000).

a vertical disc wind, originating at a critical distance in the accretion disc, could be the origin of the Broad Emission Lines and that their widths are the Keplerian velocities of the accretion disc at the radius where this wind arises. The disc wind forms for external accretion rates higher than a minimum value below which a standard Shakura-Sunyaev disc is stable and extends down to the last stable orbit. The transition radius  $r_{\text{tran}}$ , derived by setting equal the radiation pressure at  $r < r_{\text{tran}}$  and the gas pressure at  $r > r_{\text{tran}}$ , in a standard SS-disc, can be expressed as a function of the accretion rate:

$$r_{\text{tran}} f^{-16/21} \simeq 15.2 (\alpha m)^{2/21} \left( \frac{1}{\eta} \dot{m} \right)^{16/21}, \quad (1.9)$$

where  $m = M/M_{\odot}$  of the accreting source,  $f = f(r) = (1 - r^{-0.5})$  are the boundary conditions at the marginally stable orbit,  $\dot{m} = \dot{M}/\dot{M}_{\text{Edd}}$ . They assumed constant values for radiative efficiency  $\eta = 0.06$  and viscosity  $\alpha = 0.1$ . Equation 1.9 allows

us to define the minimum external accretion rate needed for a thermally unstable radiation pressure dominated region to exist. At lower accretion rates a SS-disc is stable down to the last stable orbit: all the available energy is dissipated in the disc and no radiation pressure supported and driven wind is generated. The transition radius is a function of the accretion rate, and becomes smaller than the innermost stable orbit for accretion rates (and therefore luminosities) lower than a threshold that depends weakly on the BH mass. Weak AGN should, therefore, lack the BLR (Fig. 1.4).

### 1.4 The continuum emission

AGN shine over  $\sim 10$  decades of the electromagnetic spectrum, from the radio to the gamma rays and in most of this wide energy range they are the brightest objects in the sky. In the following sections we will describe the Spectral Energy Distribution (SED, shown in Fig. 1.5) of Seyfert galaxies, in the different energy bands of the electromagnetic spectrum. It should be noted that the following description applies well to all radio quiet AGN, once accounted for the characteristic properties of each subclass. Moreover, the same consideration holds true for radio loud objects (at least those not dominated by jet emission), even if, in this case, the differences are clearly better defined in some electromagnetic bands, such as the radio emission, naturally larger in this class, and the  $\gamma$  ray spectrum, typically observed only in blazars.

#### 1.4.1 Optical/UV

The dominant feature in the UV/optical spectra of AGN is the big blue bump, as we can clearly see in Fig. 1.5 and 1.6, which can be attributed to thermal emission from a plasma at a temperature in the range  $10^{5\pm1}$  K. The peak energy is around the Lyman edge ( $\lambda = 1216\text{\AA}$ ), and the spectrum can be well approximated by a power law both at lower and higher frequencies. The emission from an optically thick and geometrically thin accretion disc for a SMBH should peak in the UV (its temperatures are expected to be of the order of  $\sim 10^5$  K.). The big blue bump is therefore most likely ascribed to thermal emission from the accretion disc. However, this association is not evident, since the exact shape of the optical/UV continuum is often strongly contaminated by starlight from the host galaxy, absorption by intervening materials and reddening by dust. Moreover, the superposition of the broad emission lines in this energy range makes this analysis very complex. In particular, a set of blended Balmer and Fe II emission lines together with the Balmer continuum make up the 'small blue bump', which alters

## 1.4. The continuum emission

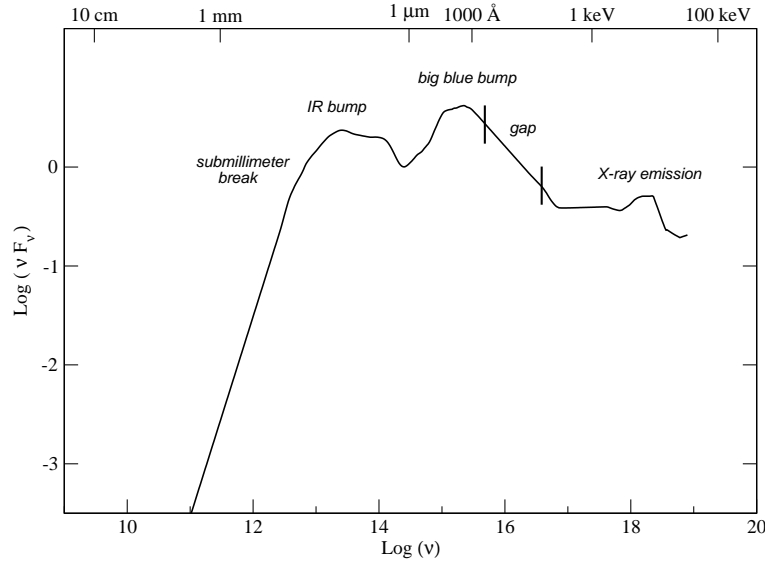


**Figure 1.5:** A typical Spectral Energy Distribution (SED) for a radio quiet AGN is shown. The y axis is arbitrarily normalized, data were taken from (Elvis et al. 1994), together with an extrapolation in the 'gap' (see text for details).

the shape of the underlying continuum in the range between  $\approx 2000 \text{ \AA}$  and  $4000 \text{ \AA}$  (see figure 1.6). It should also be remarked that in the extreme ultraviolet our own Galaxy is opaque and no data are available in that 'gap' (see figure 1.5).

### 1.4.2 Infrared

The integrated IR emission ( $2\text{--}200 \text{ }\mu\text{m}$ ) accounts, on average, for the  $\sim 30\%$  of the bolometric luminosity and it is believed to be mainly due to reprocessing of the primary radiation from dust. The presence of the IR bump, with a minimum around  $1\text{ }\mu\text{m}$  (see Fig. 1.5), is ubiquitous in AGN (Sanders et al. 1989; Haas et al. 2005) and it leads to the conclusion that the emission must be thermal, since the required temperatures are in the right range ( $\approx 2000\text{K}$ ) for hot dust in the nuclear regions (at higher temperatures dust grains would sublime). The submillimeter break at the end of the far-IR band (see Fig. 1.5) can be easily reconciled with the rapid loss of efficiency of dust grains at long wavelengths. This would explain the sharp cutoff observed just short ward of  $1 \text{ mm}$ . A sublimation radius can be defined as the minimum distance from the AGN at which grains of a given composition can exist. Indeed, in the clumpy torus model proposed by Nenkova et al. (2008) the inner radius of the torus is defined by the dust sublimation temperature

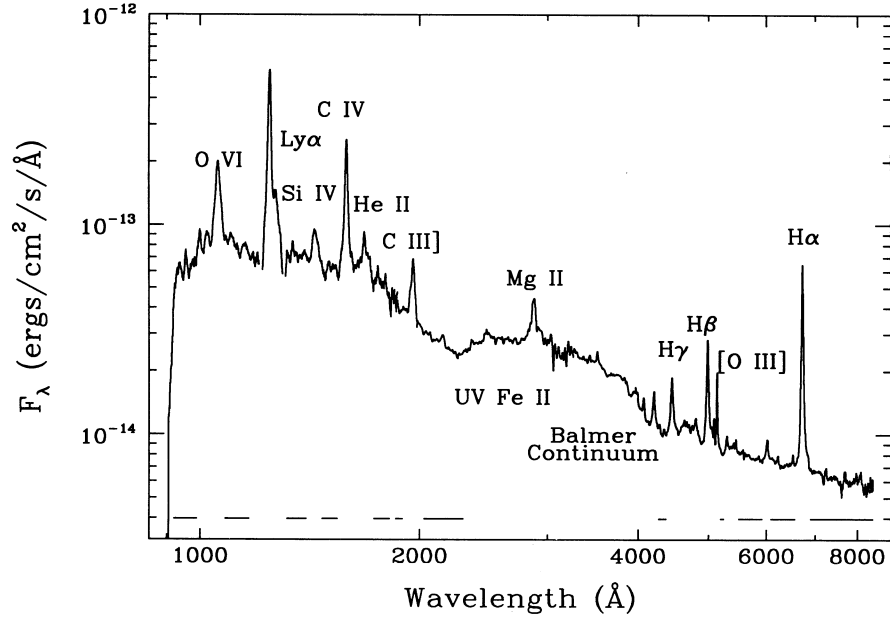


**Figure 1.6:** Merged UV/optical spectrum of the Seyfert 1 galaxy Mrk 335. Major emission features are labelled and the small blue bump can be seen between 2000Å and 4000 Å (from Zheng et al. 1995)

$T_{\text{sub}}$  as follows:

$$R_d \approx 0.4 \left( \frac{L}{10^{45} \text{ erg s}^{-1}} \right)^{0.5} \left( \frac{1500 \text{ K}}{T_{\text{sub}}} \right)^{2.6} \text{ pc} \quad (1.10)$$

where  $L$  is the intrinsic AGN luminosity and  $T_{\text{sub}}$  is typically in the range 1000-1500 K. In more luminous AGN,  $R_d$  increases, and hence the opening angle of the torus must also increase. This leads to a luminosity dependence on the observed Sy1-Sy2 ratio: this is often referred to as the receding torus (Lawrence 1991; Simpson 2005).

The reprocessing dust model is also supported by infrared variability. A optical/UV variation should be followed by an IR variation, but with a significant time delay due to the larger scale where the dust is distributed. In the particular case of Fairall 9 this is exactly what was observed: a delay was measured of about 400 days (Clavel et al. 1989). This means that the minimum distance of dust is just below a parsec or so, in extremely good agreement with the expected sublimation radius for an object of such luminosity. The emerging scenario is a nucleus where the UV/optical continuum fully depletes the dust up to the sublimation radius. Beyond this radius, the same radiation heats the dust to a wide range of temperatures (depending on the distance from the central source), producing the observed IR

## 1.4. The continuum emission

---

bump around 10-30  $\mu\text{m}$ . It should be noted, however, that a significant contribution of starlight to the dust heating has been proposed, especially in the far IR band (Prieto et al. 2001).

### 1.4.3 Radio

The radio emission, in Seyfert galaxies, contributes very little to the bolometric luminosity; the luminosity can be 5-6 orders of magnitude lower than the UV/optical continuum. The emitting region is usually very compact in radio quiet AGN, the radio spectra are very flat and become steeper at shorter wavelengths (see Lal & Ho 2010, and references therein). This is a typical characteristic of non-thermal emission and hence synchrotron radiation is generally invoked as the mechanism responsible for the radio continuum. The flatness of the radio spectrum can be ascribed to a complex source structure and the presence of low-frequency cutoffs found in some objects can be explained in terms of synchrotron self absorption, even if the frequency dependence is not as steep as it should be.

The search for intrinsic differences between the radio properties of Seyfert 1s and Seyfert 2s is still essentially inconclusive. In particular it is not clear why the powering mechanism of radio loud AGN (ultra relativistic electrons in jets) is so weaker in radio quiet sources.

### 1.4.4 X-rays

The X-ray properties of AGN have been intensively studied in the last 25 years, since the first X-ray missions in the mid-1970's. In the following we will discuss the main physical mechanisms in this energy range and the observational features that can be investigated, focusing our attention on both obscured and unobscured objects.

#### The primary emission

The primary X-ray spectrum of Seyfert galaxies is a simple power law with spectral index 1.8-2.0 and a high-energy cutoff around 100-200 keV (Perola et al. 2002). In AGN, a radiatively-efficient accretion disc cannot account directly for the hard X-ray emission, since it mainly radiates in the UV/soft X. After the seminal work by Shakura & Sunyaev (1973) the most promising physical mechanism to produce such components is Comptonization of UV seeds photons produced by the disc in a surrounding hot 'corona' (Liang & Price 1977; Liang 1979), possibly due to magnetic fields from the body of the disc itself (Haardt & Maraschi 1991; Zdziarski et al. 1994). The 'two-phase' model assumes a sandwich geometry



where the hot corona (dominated by electron-positron pairs in thermal equilibrium at a temperature  $T_e$ ) completely embeds the accretion disc, in this scenario the high-energy cutoff naturally arises as a function of  $T_e$ . The optical depth  $\tau$  of the corona is defined by the compactness parameter  $l_c$  which depends on the height scale of the corona, the accretion disc radius and the overall luminosity of the object. The inverse Compton scattering of the UV seed photons emitted by the underlying disc on the hot electrons produces a X-ray power law spectrum, which photon index is a function only of  $T_e$  and  $\tau$ .

However, this simple model fails to reproduce the observed X-ray spectra, since it is required that most of the gravitational energy must be dissipated in the corona rather than in the disc, implying a X-ray luminosity comparable to the one emitted in the UV band. It has been shown that, on the contrary, UV luminosity are much larger (Walter & Fink 1993). More complex geometries have been therefore proposed. For instance, Haardt et al. (1994) proposed and developed a 'patchy corona' model, where hot electrons partially cover the disc and are not distributed uniformly around it. The emission from the regions of the disc under the active clouds is then effectively dominated by the radiation produced by the corona, but the rest of the disc simply radiates as if the corona were not present.

### The reprocessed emission

The interaction between the disc and the corona is a fundamental ingredient of the two-phase model. A substantial fraction of the X-ray photons (actually half of them in the plane parallel limit, if the corona emission is isotropic) is emitted in the direction of the accretion disc again. A large number of these photons are absorbed by the disc and then re-emitted as black body radiation, contributing once again as the seed photons to be Comptonized by the corona. Another fraction of the X-ray radiation interacting with the disc is Compton scattered and adds to the primary spectrum emitted by the corona. This gives rise to a characteristic reprocessed spectrum, very dependent from the ionization state of the disc. If it is highly ionized, Compton scattering becomes the main interaction mechanism, leading to a power law spectrum indistinguishable from the primary nuclear continuum. On the contrary, if matter is mostly neutral, photoelectric-absorption prevails at lower energies (Guilbert & Rees 1988; Lightman & White 1988). This last process is responsible for an emission spectrum where fluorescent narrow  $K\alpha$  lines from the most abundant metals are detected. The strongest emission line is produced by iron, at 6.4 keV if the matter is mostly neutral, and up to 6.68 and 6.97 keV from more ionized material. This line comes together with a sharp ionization edge at 7.1 keV, which accounts for the absorbed photons above the photoionization threshold for neutral iron (this energy clearly shifts to higher values for ionized iron). Photoelectric absorption is an energy-dependent

## 1.4. The continuum emission

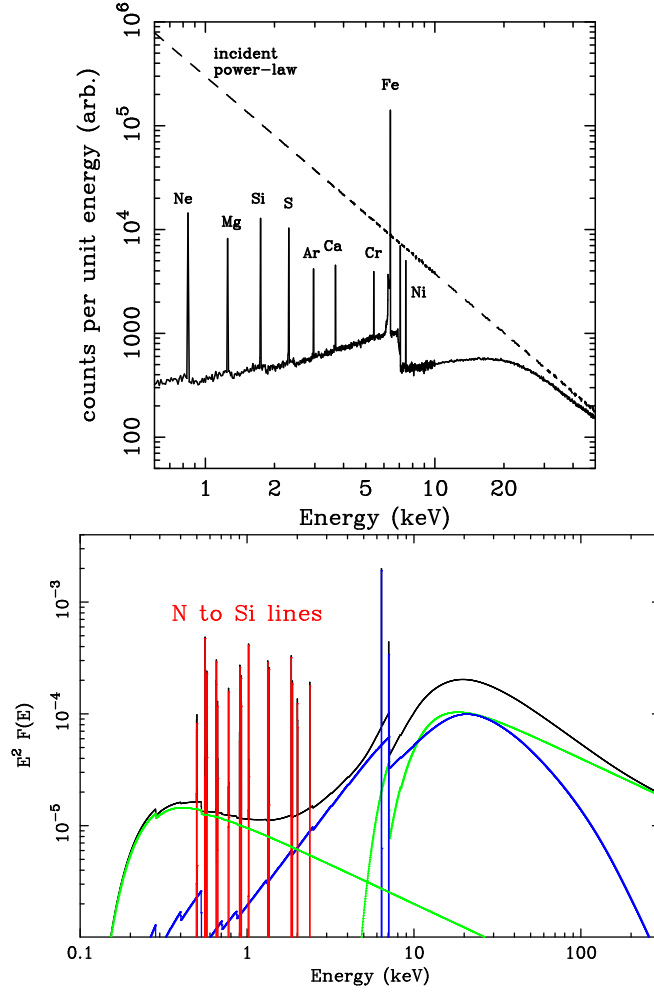


**Figure 1.7:** *Top panel:* Reflection of a power law X-ray spectrum from an optically thick neutral material. The incident continuum is shown as a dashed line, while the straight line is the reprocessed spectrum, including the  $K\alpha$  lines from the indicated elements, from (Reynolds 1999). *Bottom panel:* The broadband spectrum of a Seyfert 2 galaxy. The primary continuum (green) is heavily absorbed by a column density  $N_H > 10^{24} \text{ cm}^{-2}$ , identified as the putative torus, partially blocking the line of sight. This material is responsible for the nearly neutral X-ray reflection (blue) from the visible side of the torus. Since the primary continuum flux is much lower with respect to unobscured objects several emission lines due to photoionized gas are detected (red), from Fabian & Miniutti (2005).

process, so that incident soft X-rays are mostly absorbed, while hard photons tend to be Compton scattered back out of the disc, producing a sort of hump peaking at

$\sim 30$  keV (George & Fabian 1991; Matt et al. 1991). The typical X-ray reflection spectrum from a neutral and uniform density semi-infinite slab of gas is shown in Fig. 1.7 (top panel), where several emission lines are present below 10 keV and the Compton hump can be seen above 20 keV.

### The soft excess

A soft, quasi-blackbody excess is often observed in the energy range below 1 keV in most spectra of Seyfert 1s. For a very complete review on this subject we refer the reader to Fabian & Ross (2010). So far, we described the scenario where the irradiation is weak and the gas dense, so it remains neutral, which is unlikely in the innermost regions of an AGN. It is expected that the irradiation from the corona is intense enough to ionize at least the surface of the accretion flow. There might also be sufficient radiation intrinsic to the accretion flow (e.g. thermal black body emission) which also ionizes the matter. Ross & Fabian (1993) calculated X-ray reflection spectra taking into account different parameters of the accretion disc, such as ionization state and temperature. In Fig. 1.8 we show ionized reflection models calculated for different accretion rates (15%, 20%, 25% and 30% of the Eddington limit), for a  $10^8 M_{\odot}$  black hole. Several models have been proposed in the last few years but the origins of such spectral features in the soft X-rays of AGN are still under debate. A blurred ionized reflection has been proposed by (Crummey et al. 2006): the soft X-ray lines in the reflection spectrum at standard solar abundances might overlap each other so that they relativistically blur into a mildly-structured soft hump. In this scenario the soft X-rays should be linked with the hard ( $>10$  keV) X-rays and reflection components; i.e., a broad iron line and a bump at  $\sim 30$  keV, are expected. Other authors proposed that the soft excess could result from warm Comptonization in an optically thick plasma (Petrucci et al. 2012; Done et al. 2012). In this case, a correlation between the UV and soft X-ray emission is expected. Finally, the effect of partial covering ionized absorption can also account for part of the observed soft excess without requiring material to be moving at extreme velocities (e.g. Miller et al. 2008).

## 1.5 Signatures of the circumnuclear environment

Most of the emission from AGN is somewhat, or at least in part, obscured. In the local universe optically obscured type 2 AGN outnumber unobscured type 1 AGN by a factor  $\sim 4$ , as shown by Maiolino & Rieke (1995). Moreover, heavy absorption in the X-rays is very common, since about half of the optically selected Seyfert 2s in the local Universe are Compton-thick (Maiolino et al. 1998).

### 1.5. Signatures of the circumnuclear environment

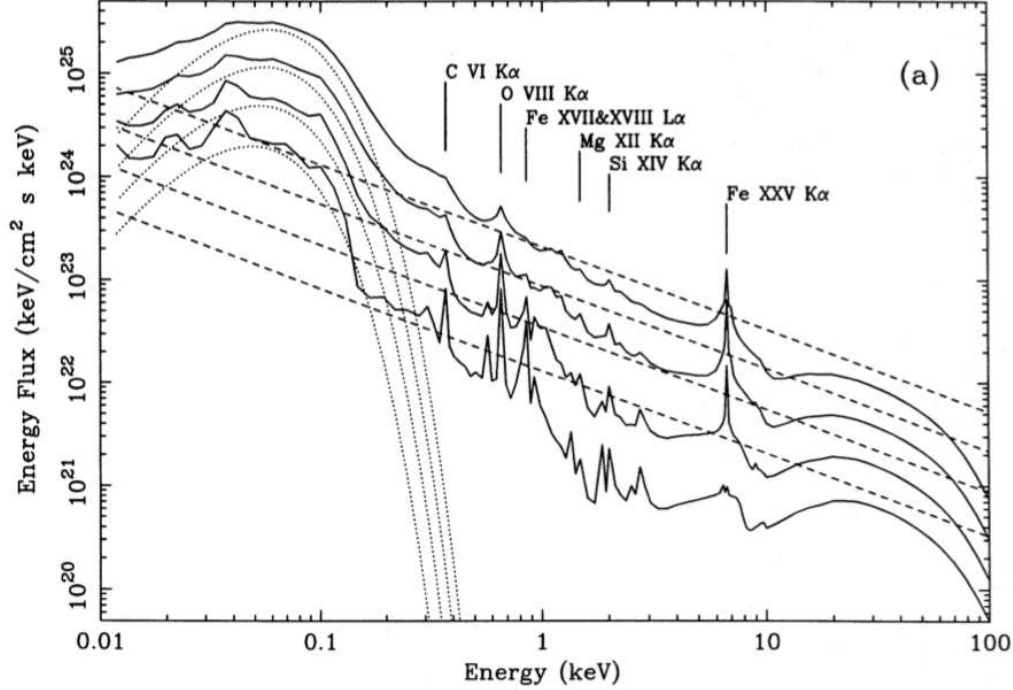


**Figure 1.8:** : Ionized reflection models calculated for different accretion rates (15%, 20%, 25% and 30% of the Eddington limit), for a  $10^8 M_\odot$  black hole. Solid curves show the spectrum emerging from the surface layer for each model. Dashed and dotted curves show the illuminating hard spectrum (a power-law of photon index 1.8) and the soft spectrum entering the surface layer from the disc below, respectively. From Ross & Fabian (1993).

The geometry of the different absorbers distributed around the central engine is therefore crucial for the understanding of the mechanisms that fuel AGN. In the following we will describe the different emission features from the reprocessing of the nuclear radiation from the circumnuclear absorbing material.

In the previous sections we showed how reflection in X-rays is due to photoelectric absorption (dominant below  $\sim 4$  keV) and Compton scattering (dominant from  $\sim 7$  keV up to  $\sim 30$  keV). The X-ray properties of obscured AGN strongly depend on the amount of absorbing column density: column densities above  $\sigma_T^{-1} = 1.5 \times 10^{24} \text{ cm}^{-2}$  (i.e. when the optical depth for Compton scattering equals unity) completely block the X-ray primary emission up to 10 keV or more and the source is classified as 'Compton-thick'. Column densities below this value (but still in excess of the Galactic one) produce a photoelectric cutoff at energies between 1 and 10 keV and in this case the object is classified as 'Compton-thin'. Otherwise, the source

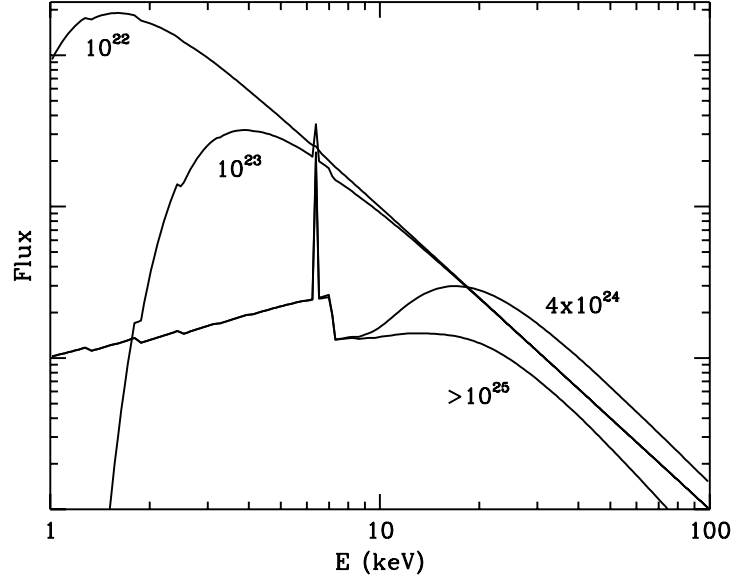


**Figure 1.9:** The X-ray spectrum of an obscured Seyfert Galaxy, for different column densities of the absorber, assumed to form a geometrically thick torus (from Matt et al. 2003).

is completely unabsorbed and the spectrum unaltered. In Fig. 1.9 the emerging X-ray spectra for different absorbing column densities can be seen.

### 1.5.1 The reflection component

In Sect. 1.3 we described how, after the discovery of polarized broad lines in the optical spectra of NGC 1068 (Antonucci & Miller 1985; Miller & Antonucci 1983), a torus was proposed as the most natural configuration for the circumnuclear absorber. If such torus is Compton-thick, it could be indirectly observed even if it does not intercept the line of sight. In fact, part of the nuclear radiation could hit the inner walls of the material and then be scattered towards the observer. The reprocessed spectrum should have the same shape as the Compton reflection component produced by the accretion disc. In Fig. 1.10 several reflection spectra are

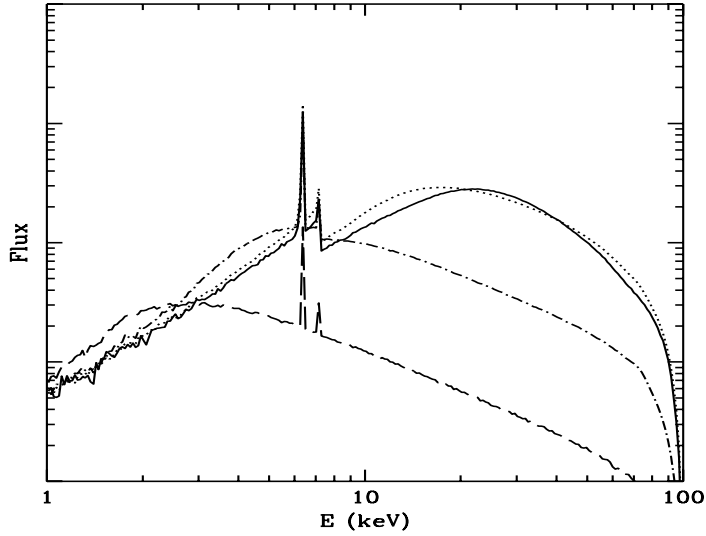


**Figure 1.10:** The reflection spectrum from the torus for different column densities:  $2 \times 10^{22} \text{ cm}^{-2}$  (dashed line),  $2 \times 10^{23} \text{ cm}^{-2}$  (dotted-dashed line),  $2 \times 10^{24} \text{ cm}^{-2}$  (dotted line),  $2 \times 10^{25} \text{ cm}^{-2}$  (solid line). The torus is assumed to be face-on, illuminated by a power law with photon index 2 and exponential cutoff at 100 keV (from Matt et al. 2003).

calculated as a function of the column density of the torus, from  $2 \times 10^{22} \text{ cm}^{-2}$  up to  $2 \times 10^{25} \text{ cm}^{-2}$ . However, as we will see in the next sections, both Compton-thin and Compton-thick absorbers can co-exist in the same source as already observed by several authors, e.g in NGC 1365 (Risaliti et al. 2005), NGC 6300 (Guainazzi 2002), UGC 4203 (Guainazzi et al. 2002) and NGC 5506 (Bianchi et al. 2003). Matt (2000) proposed a model where the torus is assumed always to be Compton-thick, while Compton-thin absorption comes from large scale (hundred of parsecs) dust lanes, like the one observed with the HST by Malkan et al. (1998).

### 1.5.2 The Iron $K\alpha$

The optically thick material surrounding the central nucleus is also responsible for emission lines due to fluorescence. If an X-ray photon has an energy higher than the binding energy of the K-shell electrons of an ion, one of them can be expelled via photoelectric absorption. The vacancy is then filled by an electron from a

different outer shell, with the release of a new photon, whose energy is equal to the difference between the two shells, or giving the same amount of energy to another electron (the so called ‘Auger effect’). If the electron came from the L-shell, the emitted photon is called  $K\alpha$  and the transition is that with the highest probability to occur; if the original shell was the M, the transition is called  $K\beta$ . Both transitions are doublets, because of spin-orbit coupling effects. The total probability that the de-excitation happens via the emission of a photon, whatever the transition, is called ‘fluorescent yield’, rising function of the atomic number  $Z$  (Bambynek et al. 1972). Iron is by far the most abundant among the heavy elements (e.g. Anders & Grevesse 1989a), because it represents the final stage in thermonuclear fusion. Therefore,  $K\alpha$  iron lines are very prominent and crucial in a great variety of astrophysical sources.

The relevant energies for neutral iron are 6.391 and 6.404 keV for the  $K\alpha_1$  and  $K\alpha_2$  emission lines, respectively (Bearden 1967). The separation of these energies is smaller than the best energy resolution available in present X-ray satellites, it is then customary to adopt the value of 6.400 keV, as the mean weighted on the probability ratio 1:2 between the two transitions. Analogously, the weighted mean for the  $K\beta$  doublet is 7.058 keV (Bearden 1967).

### The Equivalent Width

The Equivalent Width (EW) of an emission line is defined as:

$$EW \equiv \int \frac{F_L(E) - F_C(E)}{F_C(E)} dE \quad (1.11)$$

where  $F_L(E)$  is the observed flux of the line, while  $F_C(E)$  is the corresponding continuum level at the same wavelength. It strongly depends on the underlying continuum and therefore, for a given incident spectrum, it depends only on the physical properties of the material that produces the line. In several type 1 AGN the Iron  $K\alpha$  line is believed to be produced in the accretion disc. In the following we will briefly outline the main key parameters such as the geometry of the disc and the ionization structure of the emitting gas.

Let us assume a geometry with an accretion disc illuminated semi-isotropically from above: it is clear that when the material is seen edge-on the EW of the line is fainter than if it were face-on. The equation (from Ghisellini et al. 1994) that describes the dependance from the angle  $\mu = \cos i$  between the normal to the reflecting surface and the line of sight can be written as :

$$EW(\mu) = \frac{EW_{\mu=1}}{\ln 2} \log \left( 1 + \frac{1}{\mu} \right) \quad (1.12)$$

This is due to the different projected areas in the two cases and to the fact that, in the latter, the emitted photon would have lower probabilities to be absorbed

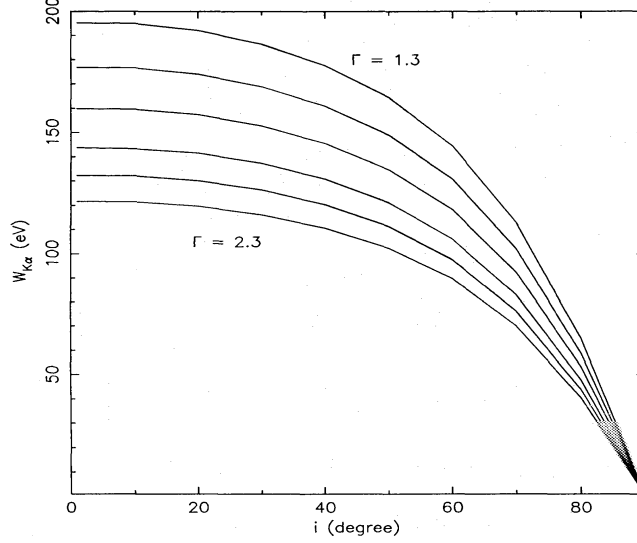


**Figure 1.11:** The EW of the iron line as a function of the inclination angle of the accretion disc, for incident power law photon index of (from the top) 1.3, 1.5, 1.7, 1.9, 2.1 and 2.3. The assumed geometry corresponds to  $R=1$  (see George & Fabian 1991, for details).

and/or scattered again. If both the line and the Compton reflection component are produced by the same material, the EW of the iron line should correlate almost linearly with the amount of reflection, which is typically expressed in terms of the solid angle  $R = \frac{\Omega}{2\pi}$  subtended by the reflector. In Fig. 1.11 the reader may find that, for a face-on disc with  $R=1$ , typical values for the iron line EW are about 150 eV, decreasing for larger angles and higher photon indexes. The ionization structure of a material can be described by the ionization parameter, which expresses the balance between the photoionization and the recombination rate:

$$\xi = \frac{4\pi F}{n} \quad (1.13)$$

where  $F$  is the incident flux and  $n$  the hydrogen number density. Matt et al. (1993, 1996) have performed detailed calculations on the reprocessed spectrum as a function of the ionization parameter of the reflecting material. For  $\xi < 100 \text{ erg cm s}^{-1}$ , we are in the 'cold' reflection regime, with an Iron line at 6.4 keV. When  $100 < \xi < 500 \text{ erg cm s}^{-1}$ , the available iron ions are FeXVII-FeXXIII. In this range the L-shell vacancy allows the resonant absorption of the  $K\alpha$  photons and the following de-excitation. The process of absorption and re-emission (the so called 'resonant scattering') will eventually end in a loss of the photon through



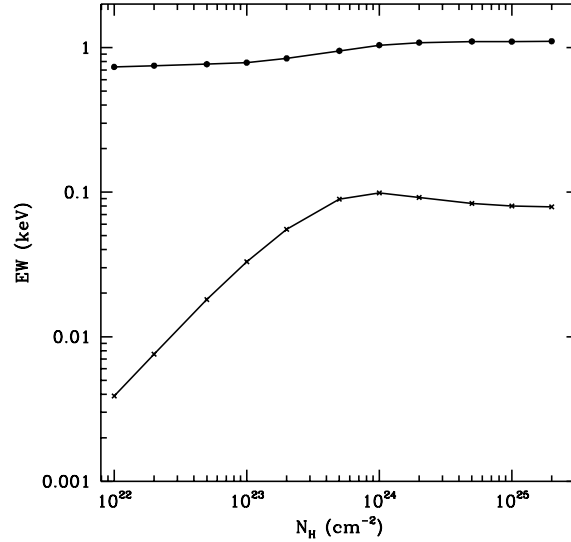


**Figure 1.12:** The EW of the iron line against the reflection continuum only (upper data) and the total continuum (lower data) as a function of the column density of a face-on torus (from Matt et al. 2003).

the Auger effect, except for a very tiny fraction of the initial line flux. Therefore, the resulting EW is very weak. For  $500 < \xi < 5000 \text{ erg cm s}^{-1}$ , iron is mainly FeXXV-FeXXVI: resonant scattering is still effective, but line photons are no longer lost, because the lack of L-shell electrons prevents the Auger effect to occur: strong lines at 6.68 and 6.97 keV are produced. In the end, when the value of the ionization parameter is even larger, iron ions are completely stripped and no line is expected.

All the above discussion is still valid if the iron line is produced by the torus instead of the disc, the main differences being in the relativistic effects which will be treated in section 1.6 for the standard accretion disc.

In heavily obscured sources ( $N_H > 10^{24} \text{ cm}^{-2}$ ), where the primary continuum is completely absorbed well above the iron line energy, the EW of the Iron  $K\alpha$  line usually ranges between  $\sim 1\text{-}3 \text{ keV}$ . In less obscured sources, it depends on the fraction of the intrinsic continuum emission absorbed at the line energy, for  $N_H < 10^{24} \text{ cm}^{-2}$ . It is useful to note that iron lines with EWs of about 100 eV are not necessarily produced by a Compton-thick material, as shown in figure 1.12, where values for Compton-thin matter are shown. The same figure display the expected

EWs as calculated against the reflected continuum only, with values easily over-exceeding 1 keV.

A significant fraction of photons produced by the fluorescent emission of an iron  $K\alpha$  line can be Compton scattered once or more before escaping from the material where they are produced. This phenomenon has been widely studied in the past and it can be observed as a series of 'Compton Shoulders' on the red side of the line core (see Matt et al. 1991; George & Fabian 1991; Leahy & Creighton 1993; Sunyaev & Churazov 1996). We refer the reader to Matt (2002), where the author extensively described the case of a single scattering, the first order Compton Shoulder, which is by far the strongest.

## 1.6 The profile of the Iron Line

The iron line profile is intrinsically narrow, apart from the natural thermal broadening (much lower than the resolution of X-ray instruments) and the Compton Shoulder described above. However, if it is produced in the accretion disc (as expected: see section 1.4.4), a number of effects contribute to forge a peculiar profile (see Fabian et al. 2000, for a review). Firstly, the line is broadened because of the rotation velocity of the accretion disc. Each radius produces a double-horned line profile, with the blue peak due to the region approaching the observer, the red one to that receding (first panel in figure 1.13). The effect is clearly higher for the inner radii of the disc, whose rotational velocities are larger. Since these velocities reach easily relativistic values, the blue peaks are beamed and thus enhanced with respect to the red ones. Moreover, the transverse Doppler effect also becomes important, shifting the overall profile to lower energies (second panel in figure 1.13). A comparable effect is due to gravitational redshift, as shown in the third panel of figure 1.13. The resulting profile is a good diagnostic tool both for the accretion disc and the central black hole's properties. First of all, it is very sensitive to the inclination angle of the disc with respect to the line of sight. When the disc is face-on, only transverse Doppler and gravitational redshift effect are clearly present, because there is no region of the disc which is actually moving in the direction of the line of sight. As the inclination angle rises, so do the velocity component along the line of sight of the approaching and receding regions of the disc, thus increasing the separation between the two peaks in the overall profile (see figure 1.14).

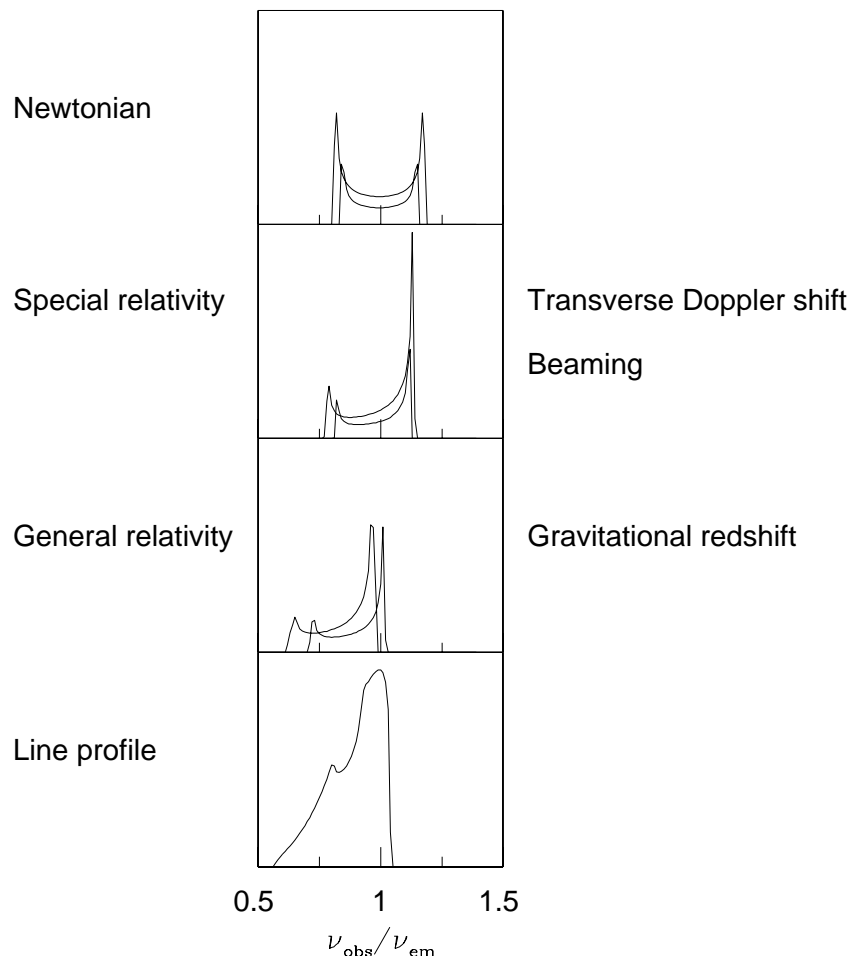


**Figure 1.13:** All the individual effects that contribute to forge the characteristic double-horned relativistic line (from Fabian et al. 2000)

## 1.7 Ionized absorption

Very little is known about the flow patterns of gas in the innermost regions of AGN. Probing the gas kinematics (velocities) and dynamics (accelerations) around black holes is a fundamental to understand the geometry of the circumnuclear regions and the energy generation mechanism. Warm absorbers are an important diagnostic of the physical conditions within the central regions of active galaxies. For more detailed reviews on this topic we refer the reader to Komossa (2000), Blustin et al. (2005) and Cappi (2006). The study of the ionized material provides a wealth of information about the nature of the warm absorber itself, its relation to other components of the active nucleus, and the intrinsic AGN X-ray spectral

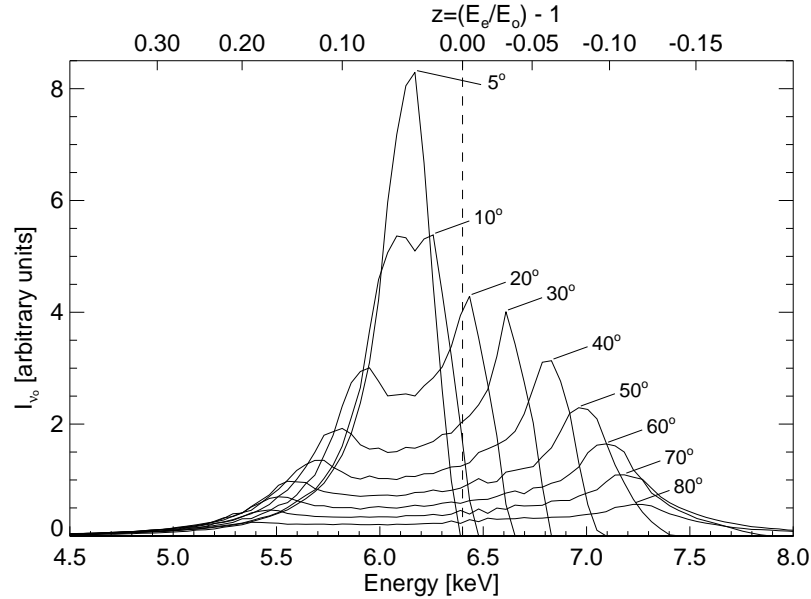


**Figure 1.14:** Iron line profiles as a function of the inclination angle of the accretion disc. The BH is assumed rapidly rotating ( $a=0.998$ ) and the adopted line emissivity index is  $\beta = 0.5$ , with the disc extending from the last stable orbit ( $1.23 r_g$ ) to  $50 r_g$  (from Reynolds & Nowak 2003).

shape. Concerning the nature and location of the warm absorber, several different models have been suggested: (i) a relation of the WA to the BLR (a high-density component of the inner BLR, a BLR confining medium, winds from bloated stars, or a matter bounded BLR component; see Reynolds et al. 1995), (ii) an accretion disc wind (e.g. Konigl & Kartje 1994), (iii) a relation to the torus (e.g. Reynolds et al. 1997), or (iv) a relation to the NLR (see, e.g., the two-component WA model of Otani et al. 1996). The reason for the large variety of models discussed is that not all physical properties of the warm absorber (its density  $n$ , column density  $N_w$ , covering factor  $\eta = \omega/4\pi$ , distance  $r$  from the nucleus, elemental abundances  $Z$ , its velocity field, and the shape of the illuminating continuum) can be directly determined from X-ray spectral fits, but only certain combinations of these parameters.

About half of the X-ray spectra of local bright Seyfert galaxies show evidence of a warm absorber with column densities in the range  $10^{22} - 10^{24} \text{ cm}^{-2}$  (e.g. Reynolds 1997). High-resolution grating observations performed with XMM-Newton and Chandra (Appendix A.1 and A.2) have shown that the warm absorber has a typical temperature of  $\sim 10^6 \text{ K}$  and, in some cases, outflowing velocities of a few times  $10^3 \text{ km s}^{-1}$  (Krongold et al. 2003). The presence of narrow blue-shifted absorp-

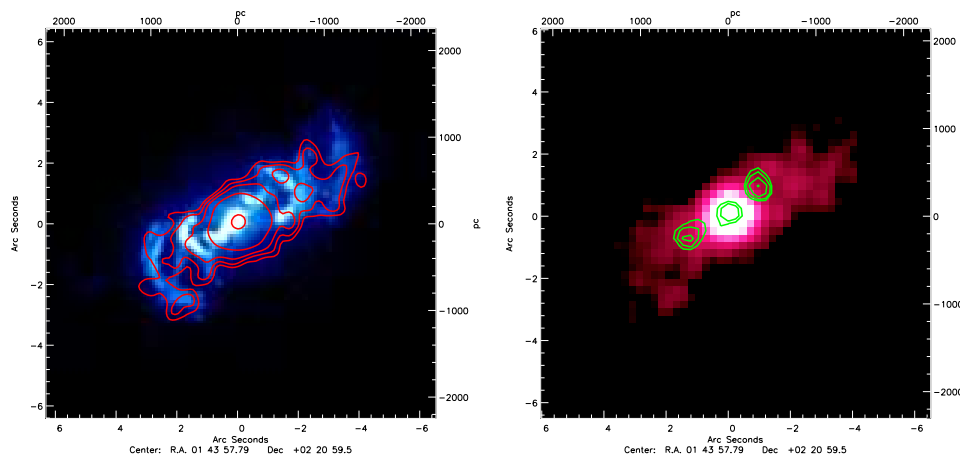


**Figure 1.15:** Left: Chandra soft X-ray (0.2-2 keV) contours superimposed on the HST O III image. The contours refer to 0.001, 0.1, 0.2, 0.4 and 0.95 levels with respect to the brightest pixel. Right: VLA radio (6 cm) contours superimposed on the Chandra soft X-ray (0.2-2 keV) image. From Bianchi et al. (2010b).

tion lines at rest-frame energies higher than 7 keV in the spectra of a number of radio-quiet AGN are commonly identified with FeXXV and/or FeXXVI K-shell resonant absorption from a highly ionized zone of circumnuclear gas ( $\log \xi \simeq 3-6$  erg s<sup>-1</sup> cm). The blue-shifted velocities of the lines are also often quite large, reaching mildly relativistic values, up to  $\sim 0.2 - 0.4c$  and in some cases showing short term variability (Cappi et al. 2009). Very recently, X-ray evidence for ultra-fast outflows (UFOs), with blue-shifted velocities  $v \geq 10^4$  km s<sup>-1</sup> ( $\simeq 0.033c$ ), has been recently reported in a number of local AGN (Tombesi et al. 2010, 2011). The detection of these UFOs is consistent with the observation of fast outflows in different classes of AGNs also in other wavebands, from the relativistic jets in radio-loud AGNs to the broad-absorption lines (BAL) in the UV and X-ray spectra of distant quasars (e.g Chartas et al. 2003).

## 1.8 Soft X-ray emission in obscured sources

X-ray spectra of many obscured AGN exhibit strong emission lines in the soft X-ray band (0.5-3 keV), the so called 'soft excess', due to the ubiquitous presence of warm gas surrounding the central nucleus. Emission from circumnuclear regions is much easier to observe in Seyfert 2s (and in particular in Compton-thick ones), where the nuclear radiation is obscured, than in unobscured Seyfert 1s, in

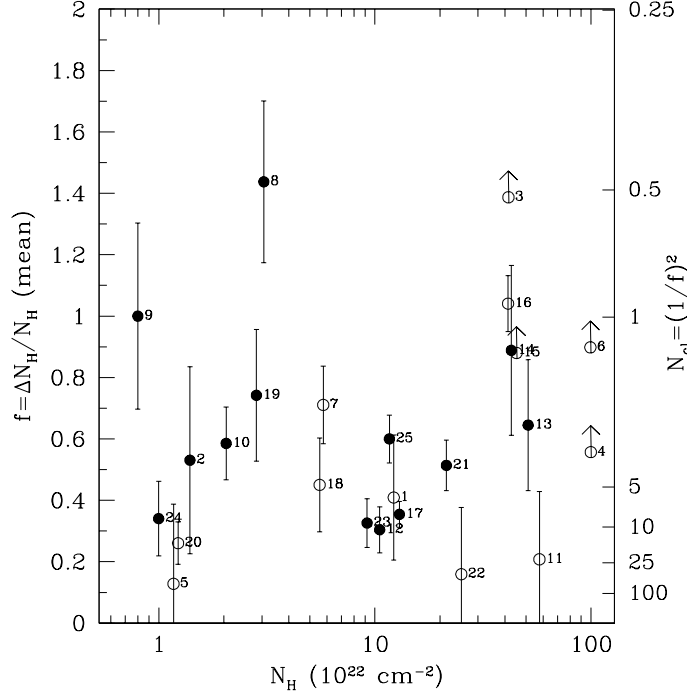


**Figure 1.16:** The ratio between the variation of  $N_H$  and the mean  $N_H$  for all the Seyfert 2 galaxies with multiple hard X-ray observations is shown. Open circles have been used for sources with only 2 or 3 observations in the hard X rays, filled circles for sources with four or more observations. From Risaliti et al. (2002)

which these components are heavily diluted by the photons from the nucleus. The line emitting region is likely to be photoionized from the nuclear primary continuum and coincident with the NLR (Bianchi et al. 2006; Bianchi & Guainazzi 2007). In Fig. 1.15, left panel, the Chandra soft X-ray (0.2-2 keV) contours are superimposed on the HST O III image and the soft X-ray emission perfectly resembles the optical one. In Seyfert 2, on the other hand, where the direct view to the continuum source is blocked by the putative molecular torus, the properties of the absorbing medium can be studied by detailed investigation of light that is reprocessed and scattered into our line of sight (see Fig. 1.7, bottom panel). The soft X-ray spectrum of Compton-thick Seyfert 2s had to await the high resolution spectrometers aboard XMM-Newton and Chandra to reveal its real nature, at least in the three brightest sources, where such an experiment was possible: NGC 1068 (Kinkhabwala et al. 2002; Brinkman et al. 2002; Ogle et al. 2003), Circinus (Sambruna et al. 2001) and Mrk 3 (Sako et al. 2000; Bianchi et al. 2005; Pounds & Page 2005).

## **1.9 Column density variability**

As described in previous sections, the circumnuclear environment of AGN is definitely much more complex than the one pictured by the Unified model. Some years ago Bianchi et al. (2009) proposed an alternative scenario to explain the column density variations by introducing different absorbers in addition to the classical torus. Indeed, a powerful tool to investigate structure, composition and distance from the central nucleus of the several absorbers is the study of column density variability through time-resolved X-ray spectroscopy.

X-ray absorption variability is a common feature among AGN. Risaliti et al. (2002) showed that local obscured AGN with multiple hard X-ray observations present column density ( $N_{\text{H}}$ ) variations on time scales from months to a few years almost ubiquitously (Fig. 1.16). However, the comparison between different observations, typically performed at distances of months-years, only provides upper limits to the intrinsic time scales of  $N_{\text{H}}$  changes. Since their seminal results many observational campaigns on much shorter time scales (from hours up to weeks) have been staged, leading to a great improvement of these estimates. In particular such studies have been successfully performed for a handful of sources: NGC 1365 (Risaliti et al. 2005, 2007, 2009), NGC 4388 (Elvis et al. 2004), NGC 4151 (Puccetti et al. 2007), NGC 7582 (Bianchi et al. 2009), Mrk 766 (Risaliti et al. 2011). We refer the reader to Bianchi et al. (2012) and Risaliti (2011) for more detailed reviews.

## Chapter 2

# The link between the Hidden Broad Line Region and the accretion rate

In the past few years, exceptions to orientation-based unification models have been found, suggesting the possibility that not all Seyfert 2 galaxies host a Seyfert 1 nucleus. However, recent works casted doubts on these conclusions (e.g. Bian & Gu 2007). In these works large, but inhomogeneous, samples were used to identify a physical parameter responsible for the existence or absence of HBLR in AGN, but no clear indication for the existence of such a parameter was found. This is likely to be due to the use of the [OIII] luminosities as a proxy of the nuclear activity of the AGN, and the difficulty in correcting this for extinction in obscured objects. It has been shown by several authors, by comparing AGN luminosities derived from [OIII] and [OIV] emission line luminosities, that the observed [OIII] luminosities often suffer significant attenuation in typical Seyfert 2 galaxies (e.g. Haas et al. 2005; Meléndez et al. 2008; Diamond-Stanic et al. 2009; Goulding & Alexander 2009; Baum et al. 2010; Kraemer et al. 2011) and that the efforts to use standard extinction correction for [OIII] are not always reliable (e.g. Goulding & Alexander 2009; LaMassa et al. 2010).

[OIV] emission line luminosities might therefore be more reliable than [OIII] luminosities, as tracers of the intrinsic nuclear emission. However, they are still an indirect proxy of the nuclear continuum emission. In the following, instead, we will use the observed X-ray (2-10 keV) continuum emission as a direct probe of the AGN activity. We selected a sample of type 2 AGN with good quality spectropolarimetric and X-ray observations, for which we can give a good estimate of the mass of the central supermassive black hole. Our work is based on a previous study discussed in Nicastro et al. (2003), but here we use a wider sample and more robust estimates of the BH masses. By doing so, we find evidence suggesting that accretion rate is the main parameter that sets the existence of HBLRs in Seyfert 2 galaxies.



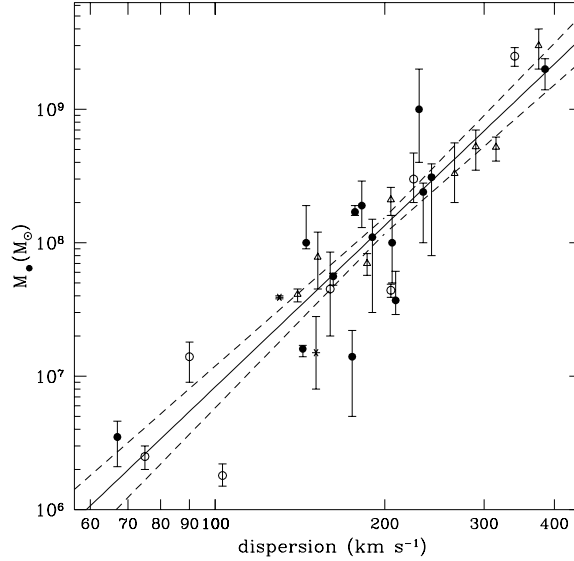


**Figure 2.1:**  $M_{\text{BH}}-\sigma_{\star}$  relation for galaxies with dynamical measurements, from Tremaine et al. (2002).

## 2.1 The Sample

Our starting sample is mostly based on the spectropolarimetric surveys performed by Tran (1995, 2001, 2003) on the Seyfert 2 galaxies included in the CfA (Huchra & Burg 1992) and 12  $\mu\text{m}$  (Rush et al. 1993) samples. Additionally, we included objects from other, high-quality, spectropolarimetric studies (Tran et al. 1992; Young et al. 1996; Moran et al. 2000; Lumsden & Alexander 2001). From this sample, consisting of 90 candidates, we selected only sources with available black hole mass (Section 2.1.1) and bolometric luminosity (Section 2.2) estimates, so that their accretion rate in units of the Eddington value,  $L_{\text{bol}}/L_{\text{Edd}}$  (hereafter  $\lambda_{\text{Edd}}$ ), can be evaluated.

### 2.1.1 The BH mass sub-selection

It is only since a couple of decades that measures of black holes' masses in AGN have become possible. The presence of an active nucleus makes it very difficult to disentangle the stellar absorption features from the nuclear spectrum, preventing the application of the classical method used in non active galaxies. For a complete review we refer to Peterson (2007).

Reverberation mapping is the main technique used to measure the size of the broad

**Table 2.1:** The sample used in this work. X-ray and bolometric luminosities are already corrected for a factor 70 for all Compton Thick sources. Columns: (a) Name of the object; (b) Instrument (AS: *Chandra* ACIS-S; PN: *XMM-Newton* EPIC pn; XIS: *Suzaku* XIS0+3) and OBSID; (c)  $\checkmark$  if Compton-thin, X if Compton-thick; (d) Stellar velocity dispersions; (e) Mass of the central BH in solar mass units; (f) Absorbing column density in  $10^{22} \text{ cm}^{-2}$  units (g) Absorption corrected 2-10 keV luminosity; (h) Bolometric luminosity; (i) Accretion rate in Eddington units; (l) Extinction-corrected O [III] ( $\lambda$  5007 ) luminosity; (m) O [IV] ( $\lambda$ 25.89  $\mu\text{m}$  ) luminosity (n) Reference for stellar velocity dispersions, HBLR (in order); series References: (1) Garcia-Rissmann et al. (2005), (2) Nelson & Whittle (1995), (3) Terlevich et al. (1990), (4) Oliva et al. (1999), (5) Barth et al. (2002), (6) Shaw et al. (1993), (7) McElroy (1995), (8) Tran (2003), (9 )Tran (1995), (10) Moran et al. (2000), (11) Young et al. (1996), (12) Lumsden & Alexander (2001), (13) Other surveys

Hidden Broad Line Region Seyfert 2s											
Object name (a)	Obs. ID (b)	C-Thin (c)	$\sigma_*$ (km s $^{-1}$ ) (d)	$\log(M_{bh}/M_\odot)$ (e)	$N_H$ (f)	$\log(L_{2-10 \text{ keV}})$ (g)	$\log(L_{Bol})$ (h)	$\log(\lambda_{eddi})$ (i)	$\log(L_{[OIII]})$ (l)	$\log(L_{[OIV]})$ (m)	References (n)
CIRCINUS	PN- 0111240101	X	$75 \pm 5$	6.42	$430^{+40}_{-30}$	42.62	43.76	-0.75	40.92	40.58	1, 13
IC 3639	XIS-702011010	X	$99 \pm 5$	6.90	$>150$	42.64	43.80	-1.20	41.89	40.66	1,8
IC 5063	XIS-704010010	$\checkmark$	$160 \pm 25$	7.74	$25^{+3}_{-2}$	42.83	44.03	-1.81	41.56	41.40	2,8
IRAS01475-0740	PN-0200431101	X	$108 \pm 17$	7.05	$> 200$	43.52	44.90	-0.25	41.76	40.74	1,8
MCG -2-8-39	PN-0301150201	$\checkmark$	$126 \pm 11$	7.32	$44^{+23}_{-24}$	42.57	43.70	-1.72	41.16	41.07	1,8
Mrk 3	XIS-100040010	X	$249 \pm 4$	8.51	$140^{+8}_{-12}$	44.44	46.10	-0.51	43.27	41.97	1, 10
Mrk 348	PN-0067540201	$\checkmark$	$117 \pm 18$	7.19	$15^{+2}_{-1}$	43.41	44.77	-0.52	41.96	40.95	2,8
Mrk 1210	PN-0002940701	$\checkmark$	$82 \pm 16$	6.57	$22^{+5}_{-6}$	43.02	44.24	-0.43	42.37	-	1,9
NGC 513	PN-0301150401	$\checkmark$	$150 \pm 25$	7.63	$7^{+2}_{-2}$	42.72	43.93	-1.80	41.14	40.74	2,8
NGC 591	PN-0200431001	X	$107 \pm 18$	7.04	$> 160$	43.02	44.27	-0.87	41.97	-	2,10
NGC 788	XIS-703032010	$\checkmark$	$140 \pm 20$	7.51	$85^{+7}_{-6}$	43.15	44.43	-1.18	40.73	40.97	2,10
NGC 1068	PN-0111200201	X	$147 \pm 3$	7.59	$> 1000$	43.02	44.27	-1.42	42.38	41.81	1,8
NGC 2273	XIS-702003010	X	$136 \pm 22$	7.46	$120^{+110}_{-46}$	42.73	43.90	-1.65	41.13	40.07	2, 10
NGC 3081	XIS-70301301	$\checkmark$	$113 \pm 4$	7.13	$89^{+13}_{-15}$	42.50	43.61	-1.62	41.43	41.09	1,10
NGC 4388	XIS-800017010	$\checkmark$	119	7.22	$31^{+2}_{-2}$	42.90	44.12	-1.20	41.85	41.58	3,8
NGC 4507	XIS-702048010	$\checkmark$	$152 \pm 4$	7.65	$87^{+7}_{-8}$	43.11	44.39	-1.36	42.19	41.02	1,10
NGC 5252	PN-0152940101	$\checkmark$	$190 \pm 27$	8.04	$2.2^{+0.1}_{-0.1}$	43.04	44.30	-1.84	42.05	-	2,11
NGC 5506	PN-0554170101	$\checkmark$	180	7.95	$3.0^{+0.1}_{-0.1}$	43.05	44.30	-1.75	41.45	41.28	4,8
NGC 7212	PN-0200430201	X	$140 \pm 9$	7.51	$> 150$	43.77	45.22	-0.38	42.73	-	1,13
NGC 7674	PN-0200660101	X	$144 \pm 32$	7.56	$> 100$	43.96	45.47	-0.18	42.57	41.97	2,8
NGC 7682	PN-0301150501	X	$123 \pm 17$	7.28	$> 100$	43.02	44.27	-1.11	41.76	41.01	2,8
Non Hidden Broad Line Region Seyfert 2s											
Object name (a)	Obs. ID (b)	C-Thin (c)	$\sigma_*$ (km s $^{-1}$ ) (d)	$\log(M_{bh}/M_\odot)$ (e)	$N_H$ (f)	$\log(L_{2-10 \text{ keV}})$ (g)	$\log(L_{Bol})$ (h)	$\log(\lambda_{eddi})$ (i)	$\log(L_{[OIII]})$ (l)	$\log(L_{[OIV]})$ (m)	References (n)
M51	PN-0303420101	X	$82 \pm 11$	6.57	$> 400$	41.54	42.51	-2.17	40.03	39.01	2,8
Mrk 573	AS-7745	X	$148 \pm 3$	7.60	$> 100$	43.10	44.37	-1.33	42.39	41.71	1,8
Mrk 1066	PN-0201770201	X	$119 \pm 19$	7.22	$> 100$	42.92	44.15	-1.17	42.27	-	2,10
NGC 1320	PN-0405240201	X	$124 \pm 14$	7.29	$> 100$	42.69	43.86	-1.54	41.08	40.67	2,8
NGC 1358	PN-0301650201	X	$185 \pm 20$	7.99	$130^{+850}_{-60}$	43.05	44.31	-1.79	41.36	40.56	2,10
NGC 1386	XIS-702002010	X	$133 \pm 3$	7.42	$> 100$	41.62	42.59	-2.92	41.09	40.25	1,8
NGC 1667	XIS-701006010	X	173	7.88	$> 100$	42.56	43.70	-2.28	42.03	40.51	3,8
NGC 3079	XIS-803039020	X	$150 \pm 10$	7.63	$> 100$	42.02	43.05	-2.68	40.48	39.53	6,8
NGC 3281	XIS-703033010	$\checkmark$	$176 \pm 3$	7.91	$79^{+10}_{-7}$	42.65	43.81	-2.20	41.30	41.58	1,10
NGC 3982	PN-0204651201	X	$81 \pm 13$	6.55	$> 100$	41.15	42.06	-2.59	40.33	39.10	5,8
NGC 5135	XIS-702005010	X	$124 \pm 6$	7.29	$> 100$	43.10	44.37	-1.02	42.21	41.48	1,8
NGC 5283	AS-4846	$\checkmark$	$148 \pm 14$	7.60	$12^{+3}_{-3}$	41.54	42.49	-3.21	40.88	-	2,8
NGC 5347	XIS-703011010	X	$103 \pm 14$	6.97	$> 100$	42.39	43.49	-1.58	41.22	40.01	3,8
NGC 5728	XIS-701079010	X	209	8.21	$> 150$	43.29	44.61	-1.69	42.83	41.36	7,11
NGC 7582	PN-0112310201	$\checkmark$	$113 \pm 3$	7.13	$57^{+10}_{-10}$	41.90	42.91	-2.32	41.63	41.11	1,8
NGC 7130	XIS-703012010	X	$147 \pm 5$	7.59	$> 100$	43.10	44.37	-1.32	42.55	40.94	1,12
NGC 7172	PN-0202860101	$\checkmark$	$160 \pm 9$	7.74	$8.4^{+0.1}_{-0.1}$	42.73	43.90	-1.93	40.84	40.82	1,8
UGC 6100	PN-0301151101	X	$156 \pm 25$	7.69	$> 100$	42.84	44.05	-1.75	42.18	-	2,8

lines emitting region once we are able to observe changes in the primary continuum. Since the accretion disc is responsible for producing a time-variable high-energy continuum that ionizes and heats the surrounding gas we can derive the size of the BLR by analyzing its response to the changes in the illuminating flux from the nucleus. If we assume a virial-like relationship between the size of the line-emitting region and the lines' Doppler velocity  $\Delta V$ , we have  $r \propto \Delta V^{-2}$ . If gravity is the main driver of the geometry and kinematics of the BLR the mass of the accreting source can be written as  $M_{BH} = \frac{f \Delta V^2 r}{G}$ , where  $f$  is a scaling factor of order unity. With this analysis it has been shown that the continuum variations appear to be in phase, with any lags between bands not exceeding a couple of days, from the shortest measured wavelength (1350 Å) to the longest (5100 Å). The highest ionization emission lines respond most rapidly to continuum variations and the lower ionization lines respond less rapidly: the BLR thus shows radial ionization stratification. Of course, the reverberation mapping technique can be performed only in objects that show broad emission lines in their optical/UV spectra, i.e. type 1 AGN.

On the other hand, it is crucial to study the nuclear potential to provide black hole masses for Seyfert 2 galaxies. One of the most direct probes to measure the near-nuclear gravitational field are dispersion velocities of stars ( $\sigma_*$ ) in the host galaxy. They do allow a clean investigation of the relation between properties of nuclear activity and the depth of the nuclear potential. Many efforts have been spent in the past to infer the correct relation between the black hole mass and the stellar velocity dispersion of the host galaxy ( $M_{BH}$ - $\sigma_*$  relation, Ferrarese & Merritt 2000; Merritt & Ferrarese 2001). In this work, BH masses are homogeneously derived for the entire sample, by using uniquely the  $M_{BH}$ - $\sigma_*$  relation (Tremaine et al. 2002, shown in Fig. 2.1):

$$M_{BH} = 1.35 \times 10^8 \left( \frac{\sigma_*}{200 \text{ km s}^{-1}} \right)^{4.02} M_{\odot}. \quad (2.1)$$

Stellar velocity dispersions were mainly taken from Nelson & Whittle (1995) and Garcia-Rissmann et al. (2005). They based their estimates on direct measurements of CaII (8498 Å, 8542 Å and 8662 Å) and MgI  $3p \rightarrow 4s$  (5167 Å, 5172 Å and 5183 Å, hereinafter Mg  $b$ ) triplet absorption lines, imprinted by the interstellar medium. For sources with more than one measurement, we used that with smaller error bars. Uncertainties on the BH mass estimates based on the  $M_{BH}$ - $\sigma_*$  relation come from the statistical errors on the  $\sigma_*$  measurements (listed in Table 1) as well as from the spread in the  $M_{BH}$ - $\sigma_*$  relation itself, estimated to be 0.44 dex (Gültekin et al. 2009). This spread is generally much larger than the statistical error on  $\sigma_*$ . We therefore assumed an uncertainty of 0.44 dex for all our BH mass estimates. Stellar velocity dispersions and their associated uncertainties, as well as BH masses, are listed in Table 2.1 (columns (d) and (e), respectively).

## 2.2. Data Analysis

---

The  $\sigma_*$  selection reduced the original spectropolarimetric sample to 46 sources with direct  $\sigma_*$  measurements.

### 2.1.2 The X-ray Sub-Selection and the Final Sample

To estimate the bolometric luminosity of the sources of our sample, we use the 2-10 keV luminosity, which is a direct tracer of the primary emission, and apply a bolometric correction. We searched the *XMM-Newton*, *Chandra*, *Suzaku* (Appendix A.3) and *Swift* (Appendix A.4) archives for observations of the sources of our sample of 46 objects with accurate BH-mass estimate. When multiple observations of a single target were available, we selected that with the highest S/N ratio in the 2-10 keV band. For all sources of our final sample, a minimum of 150 counts in the 2-10 keV band was required, to derive estimates of the column density and, therefore, intrinsic X-ray luminosity. Such column density estimates, together with other diagnostic tools such as the EW of the Iron line (Sect. 1.5.2) and the X-ray to the [OIII] fluxes, allow us to discriminate between Compton Thin and Compton Thick sources. In Fig. 2.2, 2.3 and 2.4 we show, for the sake of clarity, three different examples of spectra used in our work, with 90000, 2000 and 500 counts in the 0.5-10 keV energy band, respectively. The criteria mentioned above reduced the final sample to a total of 39 sources: 21 with polarized hidden Broad Emission Lines (HBLRs) and 18 sources without (non-HBLRs). These are listed in Table 2.1, together with the selected X-ray observations.

## 2.2 Data Analysis

### 2.2.1 X-ray Data Reduction and Analysis

*Suzaku* X-ray Imaging Spectrometer (XIS) data were processed with the latest calibration files available at the time of the analysis (2011-02-10 release), by using FTOOLS 6.11 and SUZAKU software Version 2.3, and adopting standard filtering procedures. Response matrices and ancillary response files were generated using XISRMFGEN and XISSIMARFGEN. The 0.5-10 keV spectra extracted from the front-illuminated XIS0 and XIS3 have been co-added via the ftool AD-DASCASPEC.

We used only *XMM-Newton* observations performed with the EPIC-Pn camera (Strüder et al. 2001) operated in large window and medium filter modes. Source data 'cleaning' (exclusion of flaring particle background intervals) and spectra extraction, were performed with SAS 10.0.0 (Gabriel et al. 2004) via an iterative process which leads to a maximization of the Signal-to-Noise Ratio (SNR),

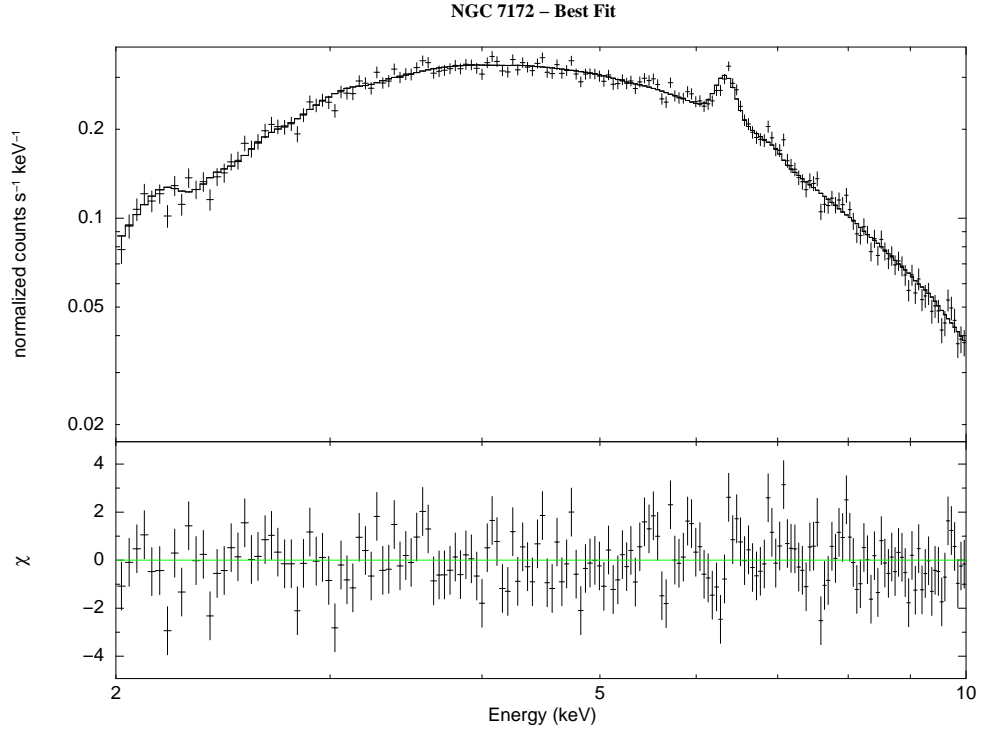


**Figure 2.2:** The high S/N EPIC Pn spectrum of the Compton Thin object NGC 7172.

similarly to that described in Piconcelli et al. (2004). For each source, background spectra were extracted from source-free circular regions of the source field.

Finally, *Chandra* data were reduced with the Chandra Interactive Analysis of Observations (CIAO; Fruscione et al. 2006) 4.3 and the Chandra Calibration Data Base (CALDB) 4.4.1 software, by adopting standard procedures.

All the spectra with a high S/N ratio were binned in order to over-sample the instrumental resolution by at least a factor of 3 and to have no less than 30 counts in each background-subtracted spectral channel. This allows the applicability of the  $\chi^2$  statistics. The adopted cosmological parameters are  $H_0 = 70 \text{ km s}^{-1} \text{ Mpc}^{-1}$ ,  $\Omega_\Lambda = 0.73$  and  $\Omega_m = 0.27$ . Errors are quoted at a confidence level of 90% for one interesting parameter ( $\Delta\chi^2 = 2.7$ ), if not otherwise stated. The spectral analysis was performed with the package XSPEC 12.7.0 (Arnaud 1996).

For all sources of our sample, we fit their 2-10 keV spectra with a general baseline model, consisting of a power law continuum attenuated by the line of sight column of Galactic absorption plus intrinsic absorption at the source redshift, plus three additional emission components: (a) a photoionized plasma emitter, to model the soft excess often detected in Seyfert 2s at  $E \lesssim 2 \text{ keV}$ , (b) a cold

## 2.2. Data Analysis

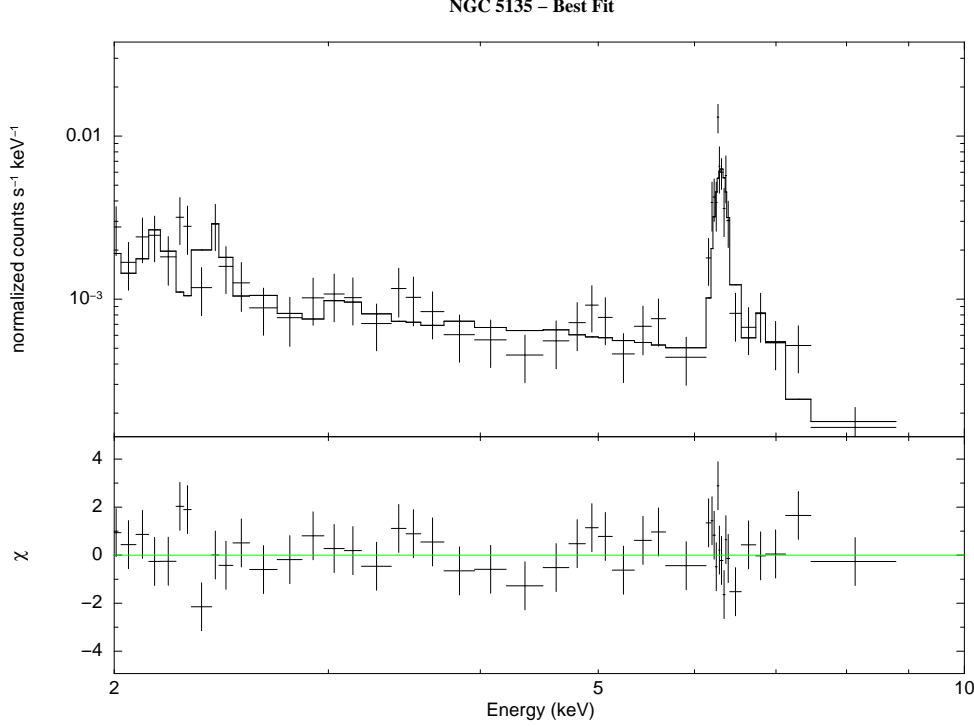


**Figure 2.3:** The coadded Suzaku XIS0+3 spectrum of the Compton Thick source NGC 5135.

Compton Reflector, scattering the primary nuclear photons off the inner walls of cold circumnuclear material into the line of sight, and (c) positive gaussian profiles, to model fluorescence emission lines of high-Z elements such as Fe at 6.4 keV, as required by the data. The model can be parameterized as:

$$F(E) = e^{-\sigma(E)N_H^G} [Ph_C + e^{-\sigma(E)N_H} B E^{-\Gamma} + R(\Gamma) + \sum_i G_i(E)] \quad (2.2)$$

where  $\sigma(E)$  is the photoelectric cross-section (abundances as in Anders & Grevesse 1989b),  $N_H^G$  is the line-of-sight Galactic column density (Dickey & Lockman 1990);  $Ph_C$  is the photoionized plasma emission (see Bianchi et al. 2010a, for details on the adopted CLOUDY model);  $N_H$  is the neutral absorbing column density at the redshift of the source;  $B$  is the normalization of the primary powerlaw with slope  $\Gamma$ ;  $R(\Gamma)$  is the Compton-reflection component (modelled in XSPEC with PEXRAV (Magdziarz & Zdziarski 1995)); and  $G_i(E)$  are the required Gaussian profiles.

Our adopted models do not aim at obtaining the ‘best fit’ for each source, but only a reliable estimate of the observed 2-10 keV luminosity (Table 2.1, column

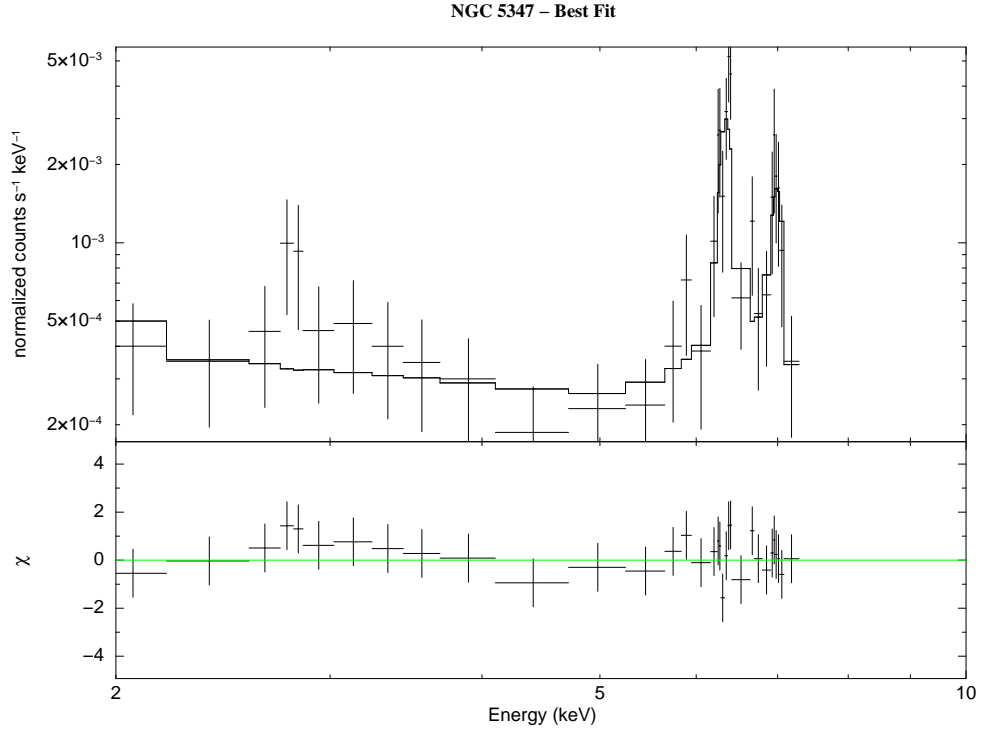


**Figure 2.4:** The coadded Suzaku XIS0+3 spectrum of the Compton-Thick source NGC 5347.

(g)).

### 2.2.2 Nuclear 2-10 keV Luminosity for Compton-Thick Sources

Compton-Thick sources are defined as sources for which the intrinsic column of absorbing gas,  $N_H$ , is greater than  $\approx 10^{24} \text{ cm}^{-2}$ , so preventing us from directly observing the primary powerlaw below 10 keV. The 2-10 keV spectra of Compton-thick sources are therefore generally adequately modeled by a pure-reflection component (i.e. reflection-dominated Seyfert 2s), which can only provide a measurement of the reflected, and not the nuclear, luminosity.

Several tracers can be used to estimate the bolometric luminosity of Compton-thick objects, e.g. [OIII] (Lamastra et al. 2009) and [OIV] (Rigby et al. 2009). For homogeneity with the Compton-thin sources of our sample, here we use the observed X-ray luminosity, by applying the following procedure. We compare the extinction-corrected [OIII] luminosities of the sources of our sample (Table 2.1, column (1)), taken from Wu et al. (2011) and Bian & Gu (2007), with their observed 2-10 keV reflection-dominated luminosities. Both works correct the ob-

## 2.2. Data Analysis

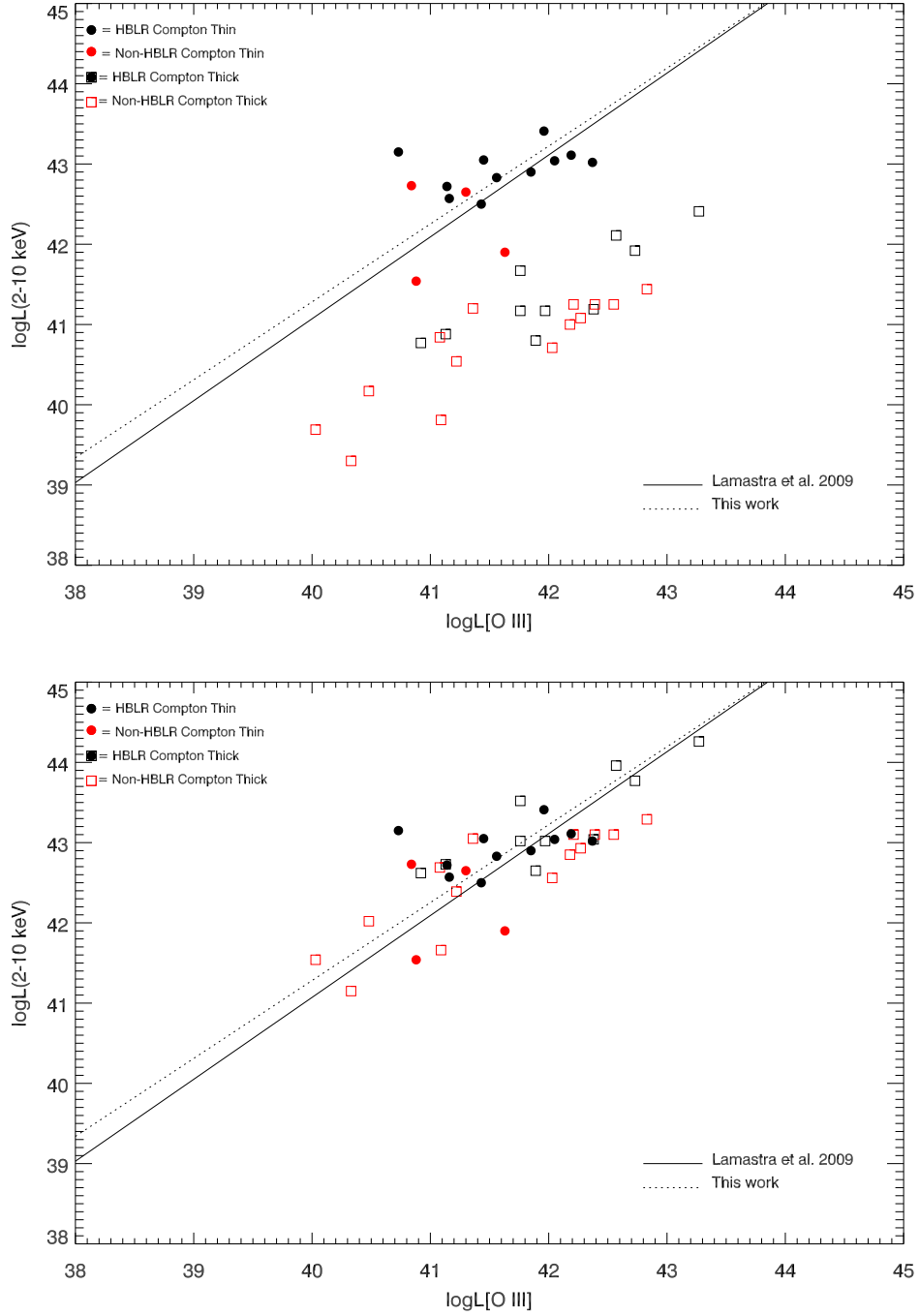


**Figure 2.5:** 2-10 keV luminosities derived from our X-ray analysis are plotted against [OIII] luminosities. A correction factor of 70 is used in the bottom panel.



served  $F_{[OIII]}$  for extinction, by applying the relation in Bassani et al. (1999) :

$$F_{[OIII]}^{cor} = F_{[OIII]}^{obs} \left[ \frac{(H\alpha/H\beta)_{obs}}{(H\alpha/H\beta)_0} \right]^{2.94}, \quad (2.3)$$

where an intrinsic Balmer decrement  $(H\alpha/H\beta)_0=3$  is adopted. The results are shown in Fig. 2.5, top panel. All the Compton-Thick sources have a  $L_x/L_{[OIII]}$  ratio smaller than the best fitting relation found by Lamastra et al. (2009) for a large sample of Compton-thin Seyfert 2s (solid line in Fig. 2.5: compare with the dotted line in the same figure, which best-fits the sub-sample of Compton-thin sources of our sample). For the Compton-thick sources of our sample, we find a mean value of  $\langle \log(L_x/L_{[OIII]}) \rangle = -0.76 \pm 0.09$ . For the Compton-thin sources of their sample, instead, Lamastra et al. (2009) found a mean  $\langle \log(L_x/L_{[OIII]}) \rangle = 1.09$ . The ratio between these two means can be used as an estimate of the correction factor needed to infer the nuclear 2-10 keV luminosity of Compton-thick sources, from their observed 2-10 keV luminosity:  $10^{1.09-(-0.76)} \simeq 70$ . The bottom panel of Fig. 2.5 shows the  $\log L_x - \log L_{[OIII]}$  plane for all the sources of our sample, after applying a correction factor of 70 to the observed 2-10 keV luminosity of all Compton-thick sources. Now all the sources of our sample lie on the Lamastra et al. (2009) relation for Compton-thin sources. We decided to adopt this correction for all Compton-thick sources, also for those where  $E > 10$  keV data were available (*Suzaku* PIN) and so a direct estimate of the nuclear continuum above 10 keV could in principle be attempted. This is because Compton scattering at high column densities may significantly suppress the observed intrinsic luminosity even at  $E > 10$  keV, and the modellization of these effects are highly dependent on the (unknown) geometry of the absorber (e.g. Matt et al. 1999). In the cases where objects presented observations in both Compton-thin and Compton-thick states in the past few years we chose the former, to infer with a higher precision the unabsorbed luminosity of the source. In one case (IRAS01475-0740), the 2-10 keV source spectrum is ambiguous: following the detailed analysis presented in Brightman & Nandra (2008) we classify this object as Compton-thick.

### 2.2.3 Bolometric Luminosities and Eddington Ratios

For each source of our sample, we used their intrinsic 2-10 keV luminosity (observed, for Compton-Thin sources, or inferred, for Compton-Thick sources, see previous section) to derive their bolometric luminosity, and thus Eddington ratio (Table 2.1, columns (h) and (i)), by adopting the luminosity-dependent relation presented in Marconi et al. (2004). We tested the importance of this assumption in our calculations, by trying different bolometric corrections (e.g. Elvis et al. 1994; Vasudevan & Fabian 2009), and comparing the results. The most significant differences between these methods were found at the extremes of the lumi-

## 2.2. Data Analysis

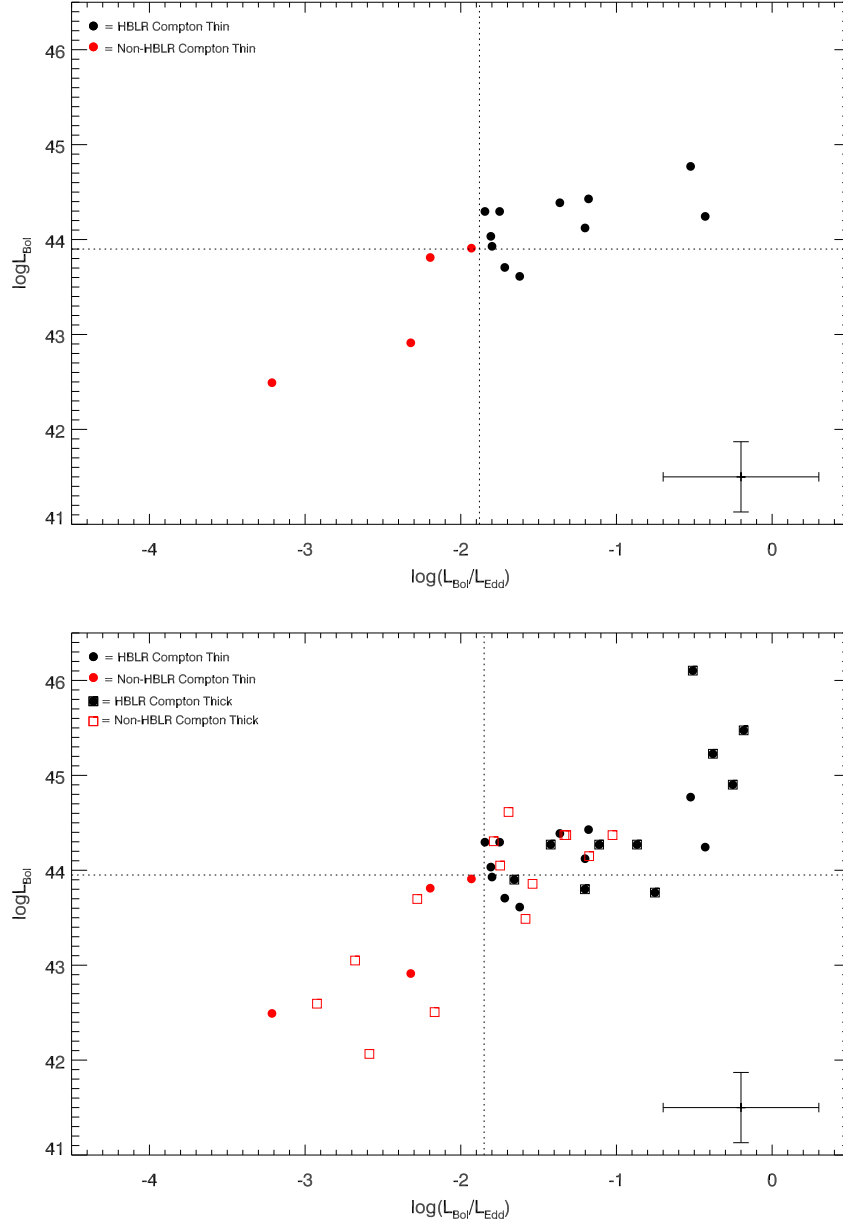


**Figure 2.6:** The bolometric luminosity inferred from the 2-10 keV luminosity against the Eddington ratio for all the Compton-thin sources of our sample is plot in the top panel while in the bottom plot Compton-thick sources are introduced, using a correction factor of 70. The dotted lines represent the maximal separation values between the cumulative distribution of the two samples with respect to  $L_{\text{Bol}}$  and  $\lambda_{\text{edd}}$ .

luminosity (accretion) range spanned by the sources of our sample. Therefore, the exact choice of the bolometric correction does not significantly affect our results. The major contribution to the bolometric luminosity error determination comes from the uncertainty on the bolometric correction itself, which is generally significantly larger than the uncertainty on the X-ray luminosity. The bolometric correction proposed by Marconi et al. (2004) is based on the correlation between the UV luminosity at 2500 Å and the 2-10 keV X-ray luminosity, whose spread is estimated as 0.37 dex in Young et al. (see eq. 3 of 2010). Therefore, we assume this uncertainty on our derived bolometric luminosities. For the Eddington ratios, we propagated the uncertainties on the BH mass and bolometric luminosity. This leads to an uncertainty of 0.5 dex in the Eddington ratios.

## 2.3 Results

We first considered only the Compton-thin sources of our sample. In the top panel of Fig. 2.6, we plot the bolometric luminosity against the Eddington ratio for all the Compton-thin sources of our sample. HBLR and non-HBLR sources are clearly separated both in luminosity and in accretion rate. To evaluate the statistical significance of this separation (both in luminosity and accretion rate), we performed a two-sample Kolmogorov-Smirnov test on our data. These tests give probabilities of 0.5% (luminosity) and 0.1% (Eddington ratio) that the two classes are taken from the same parent population. These correspond to 2-sided Gaussian-equivalent significances of  $2.8\sigma$  and  $3.3\sigma$ , respectively. The threshold Eddington ratio and luminosity that minimize the probability of chance separation, are  $\log \lambda_{edd} = -1.9$  and  $\log L_{bol} = 43.90$ , respectively.

We then repeated our analysis by including also Compton-thick sources (for which inferred intrinsic 2-10 keV luminosity estimates are uncertain: see Sect. 2.1.2). The inclusion of Compton-thick sources makes the HBLR versus non-HBLR separation less sharp (Fig. 2.6, bottom panel), and less significant, with probabilities of chance separation of 1.0% and 1.8%, for Eddington ratio and bolometric luminosity, respectively (Table 2.2), corresponding to statistical significances of only  $2.4\sigma$  and  $2.6\sigma$ . However, we note that no HBLR source falls below the Eddington ratio threshold.

### 2.3.1 Comparison with other Works and Methodologies

Other authors investigated larger (but, in most cases inhomogeneous) samples to search for physical parameters responsible for the existence or absence of HBLRs in AGN, and found often no clear indication for the existence of such a parameter (e.g. Bian & Gu 2007). However, we think that this is due to the non-homogenous

### 2.3. Results

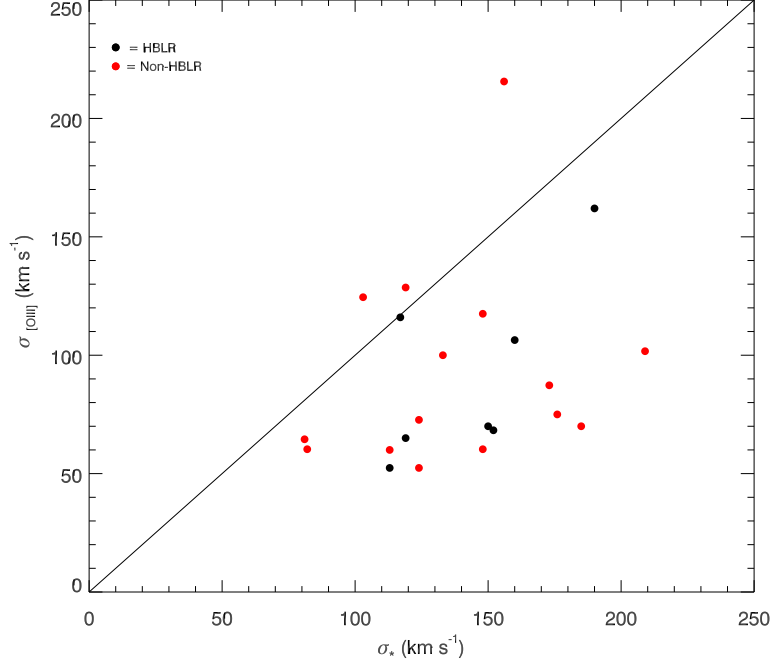


**Figure 2.7:** Stellar velocity dispersions obtained from the CaII and Mg b absorption lines against those derived through the FWHM of the [OIII] emission line (on the Y axis). The two estimates are very different and not correlated. Only the BH masses estimated with the first method will be used in this work.

nature of the assembled samples, or to the ill-suited methodologies used to derive bolometric luminosities and/or BH masses, or to a combination of both issues. BH masses can be derived through a variety of different means (e.g. FWHM[OIII],  $\sigma_*$ ). Using all of these possible means, obviously allows for large samples to be assembled. However, building samples with black-hole mass determinations derived with different methods introduces significant sources of uncertainties, which may wash out possible correlations among important physical parameters, like the source accretion rate or luminosity. For example, stellar velocity dispersion can in principle be inferred through the relation  $\sigma_* = (\text{FWHM}_{[\text{OIII}]} / 2.35) \times 1/1.34$  (Greene & Ho 2005), by making use of [OIII] FWHM measurements, which are available for a large number of sources in the literature. We tested the goodness of this estimator against the sources of our sample, for which direct stellar velocity dispersions are available. For all sources of our sample, we searched the literature for [OIII] FWHM measurements, and applied the Greene & Ho (2005) relation

## Chapter 2. The link between the HBLR and the accretion rate

**Table 2.2:** Results from the two-sample K-S test. For Compton Thick sources a correction factor of 70 is used for the calculation of the 2-10 keV luminosity and hence for the bolometric luminosity. (1) Description of the sample; (2) number of objects in the sample; (3) percentage probability that the two samples derive from the same parent population in  $L_{Bol}$ ; (4) percentage probability that the two samples derive from the same parent population in  $L_{2-10 \text{ keV}}$ ,  $L_{[OIII]}$ , or  $L_{[OIV]}$ ; (5) percentage probability that the two samples derive from the same parent population in  $\lambda_{edd}$ ; (6),(7),(8) maximal separation value between the cumulative distributions of the two samples.

Sample (1)	N (2)	$P(L_{Bol})$ (3)	$P(L_{2-10 \text{ keV}})$ (4)	$P(\lambda_{edd})$ (5)	$L_{Bol}^{max}$ (6)	$L_{2-10 \text{ keV}}^{max}$ (7)	$\lambda_{edd}^{max}$ (8)
Non-HBLR Compton Thin	4						
HBLR Compton Thin	11	0.5%	4.4%	0.1%	43.90	42.73	-1.9
Non-HBLR Compton Thick and Thin	18						
HBLR Compton Thick and Thin	21	1.8%	6.9%	1.0%	43.90	42.56	-1.8
[OIII]		$P(L_{[OIII]})$			$L_{[OIII]}^{max}$		
Non-HBLR Compton Thin	4						
HBLR Compton Thin	11	38.5%	38.5%	8.7%	43.51	41.36	-2.5
Non-HBLR Compton Thick and Thin	18						
HBLR Compton Thick and Thin	21	23.2%	23.2%	25.7%	43.54	41.39	-2.1
[OIV]		$P(L_{[OIV]})$			$L_{[OIV]}^{max}$		
Non-HBLR Compton Thin	3						
HBLR Compton Thin	9	-	-	-	-	-	-
Non-HBLR Compton Thick and Thin	15						
HBLR Compton Thick and Thin	17	10.4%	10.4%	1.1%	43.82	40.57	-1.4

to derive the stellar velocity dispersions. We then compared these estimates with the measurements of  $\sigma_*$ . Fig. 2.7 shows the result of this comparison: clearly the two values differ significantly and do not appear to be linearly correlated with one another. We, therefore, use only BH estimates based on direct measures of the  $\sigma_*$ , in order to avoid further uncertainties due to the indirect derivation of this parameter.

Another important source of potential error, is the proxy used to derive the nuclear bolometric luminosity of an obscured AGN. In our work, we use 2-10 keV luminosities, which are a direct probe of the intrinsic nuclear activity. However, such luminosities are available only for a limited number of Seyfert 2s. On the contrary [OIII] luminosities only echoes the intrinsic nuclear activity, but are

## 2.4. Discussion on the origin of the BLR

---

available for a much larger number of obscured AGN. To check the goodness of the [OIII] luminosity estimator, we compared our results with those obtained, for the sources of our sample, by using the the [OIII] luminosities and the bolometric luminosities derived from them, through the bolometric correction  $C_{[OIII]}$  described in Lamastra et al. (2009). The results are shown in Table 2.2 and Fig 2.8 (top panel): HBLR and non-HBLR sources are now mixed in both bolometric luminosities and Eddington ratios, with no significant separation between the two classes. The presence or absence of a clear separation, either in accretion rates or bolometric luminosities, between Compton-thin HBLRs and non-HBLRs, when these quantities are inferred from 2-10 keV (probabilities of chance separation of 0.1% and 0.5%, for  $\lambda_{Edd}$  and  $L_{Bol}$ , respectively) or [OIII] (probabilities of chance separation of 8.7% and 38.5%) observed luminosities, confirms (e.g. Lamastra et al. 2009; Trouille & Barger 2010, and references therein) that the [OIII] luminosity is not a direct proxy for the bolometric luminosity of an AGN.

A large number of sources in our sample (32 out of 39) also have [OIV] measurements (Pereira-Santaella et al. 2010; Weaver et al. 2010). For a few sources we inferred [OIV] luminosities following the method presented in Goulding & Alexander (2009). Using the relation in Goulding et al. (2010), both bolometric luminosities and accretion rates can be inferred from the [OIV] luminosities. The results are shown in the bottom panel of Fig. 2.8 and Table 2.2. The two classes show a more significant separation in accretion rate than in bolometric luminosity (probability of chance separation of 1.1% and 10.4%, respectively<sup>1</sup>). Both HBLR and non-HBLR Compton thick sources are included in the sample and the separation between the two different populations in accretion rate resembles the one inferred from our X-ray analysis, suggesting that the efforts to use standard extinction correction for [OIII] are not always reliable (e.g. Goulding & Alexander 2009; LaMassa et al. 2010).

## 2.4 Discussion on the origin of the BLR

Since the seminal results by Miller & Antonucci (1983) on the archetypical Seyfert 2 galaxy, NGC1068, many efforts have been spent to understand whether the Unification Model is valid for all Seyfert galaxies, in contrast of the presence/absence of the BLR being linked to intrinsic properties of different classes of sources. Intrinsic differences were strongly advocated by Tran (2001) and Tran (2003), who found that HBLR Seyfert 2s are normally associated with typical obscured Seyfert 1 nuclei, while non-HBLR Seyfert 2 galaxies host, on average, significantly weaker nuclei, likely incapable of generating classical BLRs.

---

<sup>1</sup>A K-S test for the subsample of only Compton-thin sources cannot be performed, since the minimum number of data values for a statistical significance is 4 (Stephens 1970, pag. 120-121)

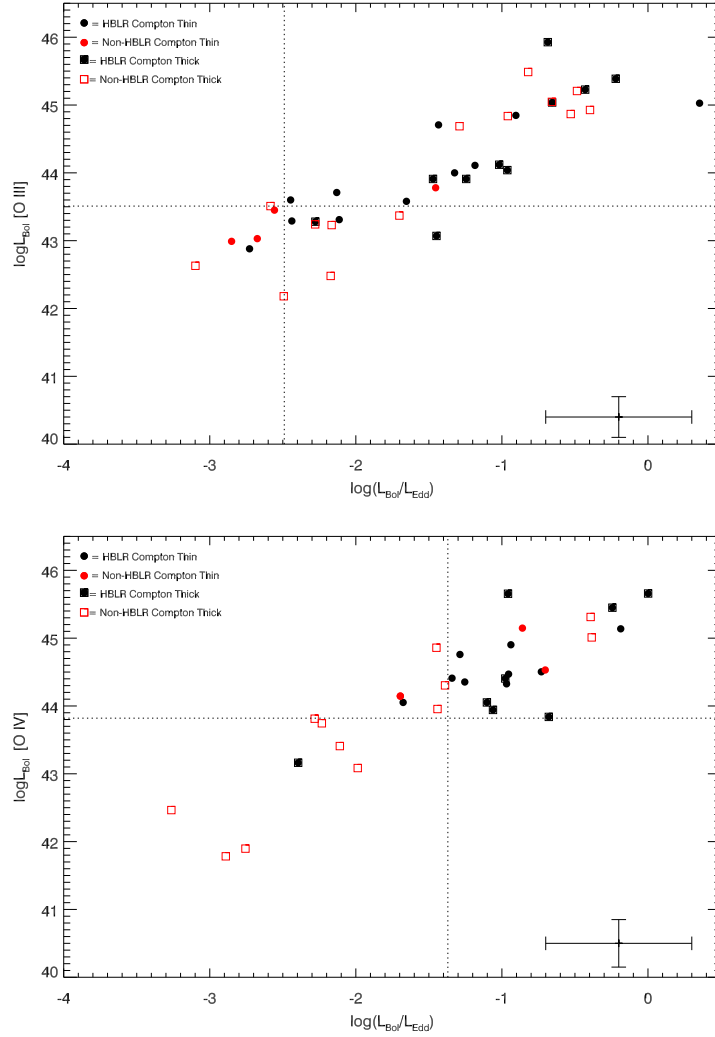


**Figure 2.8:** In the top panel bolometric luminosities derived from the [OIII] and Eddington ratios for all the 39 Compton-thin and Compton-thick sources of our sample are shown. In the bottom panel bolometric luminosities derived from [OIV] and Eddington ratios for 32 sources are shown. We used a dispersion value of  $\sigma = 0.3$  dex for uncertainties in the estimates of the [OIII] bolometric luminosities, based on a recent study presented in Risaliti et al. (2011) where the flux of the [OIII] line is used as a reliable indicator of the bolometric emission of quasars. For [OIV] bolometric luminosities we used a dispersion value of  $\sigma = 0.35$  dex (Goulding et al. 2010). The dotted lines represent the maximal separation values between the cumulative distribution of the two samples with respect to  $L_{\text{Bol}}$  and  $\lambda_{\text{edd}}$ .

## 2.4. Discussion on the origin of the BLR

---

This evidence supports theoretical models that link the presence or absence of BLRs in Seyferts to intrinsic nuclear properties. In a model proposed by Nicastro (2000), the presence of broad emission lines is intrinsically connected with disk instabilities occurring in proximity of a transition radius at which the accretion disk changes from gas-pressure dominated to radiation-pressure dominated. The transition radius is a function of the accretion rate, and becomes smaller than the innermost stable orbit for accretion rates (and therefore luminosities) lower than a threshold that depends weakly on the BH mass. Weak AGN should, therefore, lack the BLR.

In this work we try to test this model in the least possible biased observational way, by collecting the 'cleanest' possible sample of Seyfert 2 galaxies with the best spectropolarimetric data available at the moment, and robust estimates of their BH masses performed homogeneously on the basis of the observed stellar velocity dispersion. When only Compton-thin sources are considered, the estimate on their accretion rate is done directly on the observed nuclear X-ray emission, and the modest absorption is likely not able to affect severely the detection of the hidden BLR, if present. We find that the separation between HBLR and non-HBLR Compton-thin sources is highly significant both in accretion rate and luminosity. In particular, no HBLR is found below the threshold Eddington rate  $\log \lambda_{edd} = -1.9$ , and no non-HBLR above the same limit. Even when Compton-thick sources are included, no HBLR is still found at accretion rates lower than the above threshold. This threshold accretion rate is in good agreement with the value presented in a recent work (Trump et al. 2011).

This result supports the theoretical expectations of the model proposed by Nicastro (2000), albeit with a slightly higher value of the threshold accretion rate ( $\log \lambda_{edd} \sim -2.5$  in Nicastro (2000)). We stress here that the model proposed by Nicastro (2000) applies only to radiatively efficient AGN, accreting through a Shakura-Sunyaev disk (SS-disk hereinafter, Shakura & Sunyaev 1973). Broad Emission lines are known to exist in some objects (mostly LINERs or transition objects, e.g. Elitzur & Ho 2009) accreting at rates as low as  $\log \lambda_{edd} \sim -6$  (e.g. M 81, Ho 2008). These objects are probably highly radiatively inefficient, and therefore most likely do not host a classic SS-disk.

If BLRs do not exist in weakly accreting AGN, one would expect the existence of unabsorbed, genuine Seyfert 2 galaxies. Such objects do indeed exist, and the best examples (where the lack of optical broad lines and of X-ray obscuration are unambiguously assessed in simultaneous high S/N observations) have Eddington rates lower than the threshold estimated in this work: NGC 3147 ( $\log \lambda_{edd} \simeq -4$ : Bianchi et al. 2008), Q2131427 ( $\log \lambda_{edd} \simeq -2.6$ : Panessa et al. 2009), NGC 3660 ( $\log \lambda_{edd} \simeq -2$ : Brightman & Nandra 2008; Bianchi et al. 2012).

It is interesting to note that among all the 156 X-ray unobscured ( $N_H < 2 \times 10^{22} \text{ cm}^{-2}$ ) AGN observed with XMM-Newton (CAIXA: Bianchi et al. 2009), only 6



have an Eddington rate lower than the threshold found in this work<sup>2</sup>. Four of these 6 sources were previously classified as unabsorbed Seyfert 2s (Panessa & Bassani 2002; Panessa et al. 2009; Brightman & Nandra 2008) but see also Shi et al. (e.g. 2010, and references therein), who recently claimed the presence of very broad and weak broad emission lines in two of these objects). The remaining two objects are PG 1011-040 and NGC 7213, and both show the presence of BLR in their optical spectra. Both objects are peculiar. PG 1011-040 is only slightly below the accretion rate threshold of  $\log \lambda_{edd} \simeq -1.9$  that we find here and, most importantly, is severely under-luminous in X-rays with respect to its multiwavelength luminosity, so that the accretion rate derived from its 2-10 keV luminosity by simply applying the Marconi et al. (2004) correction, is likely severely underestimated (Gallagher et al. 2001; Vasudevan & Fabian 2007). NGC 7213 is the only bright Seyfert 1 galaxy known to unambiguously lack reprocessing features from Compton-thick distant material (Bianchi et al. 2003, 2004; Lobban et al. 2010).

The inclusion of Compton-thick sources in our sample makes the HBLR versus non-HBLR separation, in terms of either Eddington ratios or bolometric luminosities, less significant. Several non-HBLR Compton-thick sources lie now in the HBLR  $L_{Bol} - \lambda_{Edd}$  plane, i.e. at accretion rate higher than the threshold we find for Compton-thin sources. This mixing could be, at least partially, due to the difficulties in assessing the intrinsic 2-10 keV luminosity of Compton-thick sources, because of the unknown geometry of the absorbers and reflectors<sup>3</sup>

However, such uncertainties should in principle determine equally over- and under-estimates of the luminosities. Instead, while no Compton-thick HBLR is still found below the Eddington rate threshold, a significant fraction (64%) of Compton-thick non-HBLR has accretion rates higher than this limit. Moreover, uncertainties in the exact geometry of absorbers and reflectors, could only be responsible for modest (factor of 2-3) over-estimates of the intrinsic bolometric luminosity and so of the Eddington accretion rate. This could perhaps explain the presence of few non-HBLR closely above the Eddington ratio threshold, but can hardly explain order-of-magnitude over-estimates of the bolometric luminosity, as inferred from the 2-10 keV spectra.

If the scenario proposed by Nicastro (2000) is correct, non-HBLR Compton-thick sources with Eddington accretion rate estimates much above the threshold, are likely to be peculiar objects, where BLR line emission cannot be seen, not even in polarized light. These source should possess a BLR, but something prevents us from observing it. Different, alternative scenarios, to the intrinsic lack of a BLR,

---

<sup>2</sup>An updated catalogue was used for this search.

<sup>3</sup>The same uncertainties are probably also responsible for the lack of HBLR and non-HBLR separation when indirect estimators of the nuclear bolometric luminosity (e.g. [OIII]) are used.

## 2.4. Discussion on the origin of the BLR

---

have already been proposed in the past (Lumsden & Alexander 2001; Gu & Huang 2002; Martocchia & Matt 2002; Tran 2003; Moran 2007). This could be either because of the lack of an unobscured population of hot electrons scattering the line emission along our line of sight, or because the orientation of these sources is such that our line of sight intercept larger portions of absorbing gas, and this covers both the nuclear source and at least part of the line-reprocessing electron region (e.g. Shu et al. 2007; Wu et al. 2011, and references therein).

In conclusion, the main results of the analysis discussed in this work can be summarized as follows:

- we presented evidence suggesting that the accretion rate is the main ingredient which drives the presence of HBLRs in Seyfert 2 galaxies. By selecting a sample of 39 type 2 AGN with good quality spectropolarimetric and X-ray data, and for which we derived homogeneous estimates of the mass of the central supermassive BH, we found a clear separation between Compton-thin HBLR and non-HBLR sources, both in luminosity ( $\log L_{\text{bol}} = 43.90$ ) and in accretion rate ( $\log \lambda_{\text{edd}} = -1.9$ ). A statistically similar separation is found when bolometric luminosities are derived from infrared [OIV] emission lines.

Our results agree with the ones discussed in Nicastro et al. (2003) but have higher statistical significance (due to the larger sample we use here, compared to Nicastro et al. (2003)), and it is certainly more robust due to the more accurate estimates of the BH masses that we derive here;

- the inclusion of Compton-thick sources washes out the separation between HBLR and non-HBLR, but still no HBLR source falls below the Eddington ratio threshold. We propose that the presence of a significant fraction (64%) of Compton-thick non-HBLRs at accretion rates higher than the threshold found for Compton-thin sources is not due to the lack of BLRs, but to heavy line-of-sight absorption preventing us from observing not only the direct line emission, but also their polarized light scattered by an, at least partly, obscured population of warm electrons.



## Chapter 3

# The circumnuclear geometry of Sy2 galaxies

In this chapter we will present our results from the study of X-ray variability in two Seyfert 2 galaxies, namely NGC 4945 and NGC 4507. As already discussed in Section 1.9 X-rays provide a unique opportunity to investigate the innermost regions of AGN. Column density variations is one of the most powerful methods to infer the distribution of absorbing matter surrounding the nucleus.

The first part of this chapter is focused on a Seyfert 2 galaxy, NGC4945, where we searched for spectral variation in the high energy spectra of the source. We performed a timing, spectral and imaging analysis of the X-ray inner structure in this source, which revealed its geometrical and physical structure with unprecedented detail. NGC 4945 hosts one of the brightest AGN in the sky above 10 keV, but it is only visible through its reflected/scattered emission below 10 keV, due to absorption by a column density of  $\sim 4 \times 10^{24} \text{ cm}^{-2}$ . A new Suzaku campaign of 5 observations spanning 6 months, together with past XMM-Newton and Chandra observations, show a remarkable constancy (within  $< 10\%$ ) of the reflected component. Instead, Swift-BAT reveals strong intrinsic variability on time scales longer than one year. We show that the reflector is at a distance  $> 30\text{-}50 \text{ pc}$ , well within the imaging capabilities of Chandra at the distance of NGC 4945 (1 arcsecond  $\sim 18 \text{ pc}$ ). Accordingly, the Chandra imaging reveals a resolved, flattened, 150 pc-long clumpy structure, whose spectrum is fully due to cold reflection of the primary AGN emission. The clumpiness may explain the small covering factor of the cold reflector derived from the spectral and variability properties. This study provides evidence for absorption variability at a parsec-scale distance and proves the fundamental importance of a broadband X-ray study of AGN.

The second part of the chapter is based on a spectral analysis of an XMM-Newton and Chandra campaign of the obscured AGN in the Seyfert 2 galaxy NGC 4507, consisting of six observations spanning a period of six months in 2010. Using the

EPIC and the ACIS-S CCD cameras, we can detect strong absorption variability on time scales between 1.5 and 4 months in the circumnuclear environment of the nucleus through a very detailed spectral analysis. The variation of the absorbing column density is the first one ever observed on these time scales and it suggests that the obscuring material consists of gas clouds at parsec-scale distance. The lack of significant variability on shorter time scales suggests that this event is not due to absorption by broad line region clouds, which was instead found in other studies of similar sources, such as NGC 1365 (Risaliti et al. 2005, 2007, 2009), NGC 4388 (Elvis et al. 2004), NGC 4151 (Puccetti et al. 2007), NGC 7582 (Bianchi et al. 2009), Mrk 766 (Risaliti et al. 2011). This shows that a single, universal structure of the absorber (either BLR clouds, or the parsec-scale torus) is not enough to reproduce the observed complexity of the X-ray absorption features of this AGN.

### 3.1 The Compton-thick Sy2 NGC 4945

NGC 4945 is an almost edge-on (inclination angle  $\sim 80^\circ$ ) spiral galaxy hosting one of the nearest AGN ( $D \sim 3.7$  Mpc,  $1'' = 18$  pc, Mauersberger et al. 1996). NGC 4945 has been widely studied in the past, both in the soft and in the hard X-rays. It is the brightest Seyfert 2 and the second brightest radio-quiet AGN after NGC 4151 in the 100 keV sky (Done et al. 1996), with a strongly absorbed ( $N_H \sim 4 \times 10^{24} \text{ cm}^{-2}$ , Itoh et al. 2008) intrinsic nuclear continuum, known to be extremely variable (Guainazzi et al. 2000, Madejski et al. 2000). Such a high column density completely blocks the primary nuclear emission below 8-10 keV while the emission at higher energy is still visible, though heavily affected by Compton scattering and photoelectric absorption. A detailed analysis of the high energy variability (Madejski et al. 2000, Done et al. 2003, hereafter D03) already provided important (and, so far, almost unique) constraints on the geometry of the reflector: the variability above 10 keV implies that most of the observed emission is due to the primary emission, and not to Compton scattering from other directions (which would dilute the intrinsic variability, producing an almost constant observed emission). This, in turn, means that the reflector covers a solid angle  $< 10$  deg as seen from the source (assuming a toroidal structure). This is also in agreement with the unusually low ratio between the observed, reflected emission below 10 keV, and the intrinsic flux in the same band as estimated from the emission above 10 keV (smaller than 0.1%). Finally, a *Chandra* observation revealed a spatially resolved component, on a  $\sim 100$  pc scale, whose spectrum is typical of Compton reflection from a neutral medium (D03).

Here we present the analysis of new and archival *Suzaku*, *XMM-Newton* and *Chandra* observations, focusing specifically on the determination, with unprece-

mented detail, of the dimensions and the geometrical structure of the circumnuclear absorber/reflector in NGC 4945. A complete study, discussing both the *Chandra* imaging data, and our new *Suzaku* observations, will be presented in a separate work (Marinucci et al. 2012, in prep.). The work presented here expands the results summarized above, through two completely new studies:

- the comparison between the intrinsic variability *above* 10 keV (from *Swift*/BAT observations), and the reflection variability *below* 10 keV (from a set of 8 *XMM-Newton* and *Suzaku* observations over a period of  $\sim 10$  years);
- a detailed analysis of the spatial extension of the reflector, taking advantage of the full set of available *Chandra* observations, as discussed in the next Sections.

#### 3.1.1 Observations and data reduction

**Chandra.** NGC 4945 was observed by *Chandra* on 2000, January 27-28 for a total exposure time of 49 ks, with the ACIS camera. It was observed again four years later twice, for a total exposure time of 180 ks taking advantage of the HETG instrument. Data were reduced with the CIAO 4.3 package (Fruscione et al. 2006) and using the Chandra Calibration Data Base (CALDB) version 4.4.6, adopting standard procedures. The imaging analysis was performed on a file including the two merged HETG-zeroth order images reprojected on the ACIS-S image, applying the SER and smoothing procedures widely discussed in the literature (Tsunemi et al. 2001, Li et al. 2004, Wang et al. 2011). We therefore used a pixel size of 0.246 arcsec in Fig. 3.1 and 0.123 arcsec in Fig. 3.2. After cleaning for background flaring we get a total of 34 ks and 173 ks for the 2000 and the 2004 HETG-zeroth order merged observations, respectively. Spectra were extracted on both data sets from three different regions: a circle with 25'' radius (matching the *XMM-Newton* extraction region, see below); a  $12'' \times 6''$  box, and a central circle with 1.5 arcsec radius. We grouped all extracted spectra to have at least 20 total counts per new bin.

**Suzaku.** The six *Suzaku* observations analyzed in this work were performed with the X-ray Imaging Spectrometer (XIS). The first one has been performed in 2006, has a duration of  $\sim 100$  ks, and has been presented by Itoh et al. (2008). The remaining five observations, with a duration of 40 ks each, have been performed between July 2010 and January 2011, as part of a monitoring campaign of this source. The event files were processed and calibrated adopting standard procedures, discussed in several previous papers (e.g. Maiolino et al. 2010). The source extraction radius is 1.85' for all 6 observations. Background spectra have been extracted from source-free regions with 3' radii. The 0.5-10 keV spectra extracted from the front-illuminated XIS0 and XIS3 have been co-added.

**XMM-Newton.** We used 2 *XMM-Newton* observations performed with the EPIC-PN camera operated in large window and medium filter modes. Source data

'cleaning' (exclusion of flaring particle background intervals) were performed with SAS 10.0.0 (Gabriel et al. 2004) via an iterative process which leads to a maximization of the Signal-to-Noise Ratio (SNR), similarly to that described in Piconcelli et al. 2004. Source spectra were extracted from a 25'' radius circle; background spectra were extracted from source-free circular regions of the source field.

**Swift.** The *Swift*/BAT 15-195 keV light curve has been obtained from the on-line catalog<sup>1</sup> which at the time of our analysis included data collected over 65 months.

### 3.1.2 The reflector geometry from time and spectral variability

NGC 4945 offers a *unique* possibility to perform a comparison between the variability of the intrinsic and the reflected X-ray emission, because it is the only known AGN with both (a) Compton thickness  $\tau_C > 1$ , and (b) a strong intrinsic variability above 10 keV. For *all* the other known bright AGN, such a detailed direct comparison between the variability of the two components is impossible because one of the two above mentioned conditions is not satisfied:

- (a) if the AGN is not Compton-thick, the Compton reflection component is diluted by the dominant direct component. The separation of the two components is never precise, and typical uncertainties in the flux of the reflected component are of the order of 20-30% even for long observations of the brightest AGN.

- (b) if the AGN is Compton-thick, the intrinsic emission is either not visible (due to  $N_H > 10^{25} \text{ cm}^{-2}$ , as in NGC 1068), or, anyway, not variable, probably because of the dilution due to multiple Compton scatterings (such as in the Circinus galaxy). NGC 4945 shows one of the brightest reflection dominated spectra below 10 keV, with flux measurement uncertainties of the order of  $\sim 1\%$ , and a high-quality light curve of its intrinsic emission above 10 keV, provided by *Swift*/BAT. The highest quality spectra below 10 keV have been obtained in the eight *XMM-Newton* and *Suzaku* observations presented in the previous Section. The 3-10 keV spectra of these observations have been fitted with a model consisting of a reflection continuum (PEXRAV, Madgazar & Zdziarski 1995), three emission lines for neutral, He-like and H-like iron, and an additional power law, requested by the fit, and associated to the diffuse emission (see below). From the analysis of the HETG grating spectra we rule out the presence of emission features associated to the Iron  $K\beta$  line, as already shown in Shu et al. (2011). The analysis has been performed with the XSPEC 12.7 code (Arnaud et al. 1996). All quoted errors are at the 90% confidence level for one interesting parameter. This model successfully reproduces all the individual spectra, with best fit parameters typical of reflection-dominated sources. The details of the spectral model have been discussed in Itoh

---

<sup>1</sup><http://swift.gsfc.nasa.gov/docs/swift/results/bs58mon/>



### 3.1. The Compton-thick Sy2 NGC 4945

---

et al. 2008, Schurch et al. 2002 and D03. What is interesting in this context is instead the possible variability of the reflected component. In this respect, the following results are relevant:

1. The analysis of the *Chandra* spectrum of the resolved  $12'' \times 6''$  box, shows that the central emission is well fitted by a pure reflection continuum, with no need for an additional power law, so confirming that this component is needed only to reproduce the circumnuclear emission. Similarly, the *XMM-Newton* spectrum, extracted from the central  $25''$ , requires only a minor contribution from the additional power law (about 1/10 of that in the *Suzaku* spectra).
2. If we fit the eight spectra with constant reflection component and emission lines, leaving the additional power law as the only variable component, we obtain an equally good fit, with no significant residuals in any individual spectrum. This implies that formally, *all* the observed variability may be due to galactic sources in the field of view.
3. The whole luminosity within the central 1.85 arcmin region is only  $\sim 2 \times 10^{39}$  erg s $^{-1}$ . It is therefore not surprising if significant variability due to single sources is observed. In Fig. 3.1, top panel, the two extraction regions for the *Suzaku* and *XMM-Newton* observations are shown, respectively. The contribution from the unresolved discrete sources to the total flux in the 2-10 keV energy band is much lower in the two *XMM-Newton* spectra ( $\frac{F_{\text{pow}}}{F_{\text{pexrav}}} \simeq 0.6$ ), due to the smaller extraction radii, rather than in the *Suzaku* coadded XIS0+3 spectra ( $\frac{F_{\text{pow}}}{F_{\text{pexrav}}} \simeq 2$ ).

Based on the above considerations, we conclude that the best way to estimate the reflection variability is to fit the 8 spectra with the model described above, with only three free parameters: the slope and the normalization of the additional power law, and the flux  $F$  of the reflection (continuum plus lines) component, normalized to the value of the first interval, for ease of comparison. The results are reported in Table 3.1, and show no significant variability in any observation. If we assume a constant value of the relative flux  $F$ , we obtain  $\langle F \rangle = 0.98 \pm 0.02$  (column 5), and a marginally better fit (the  $\chi^2$  increases by 3, with 7 more degrees of freedom). The dispersion around the central value is significantly smaller than the uncertainties on the individual values. This is due to the partial degeneracy among the spectral parameters. Based on these results, we estimate an upper limit to the



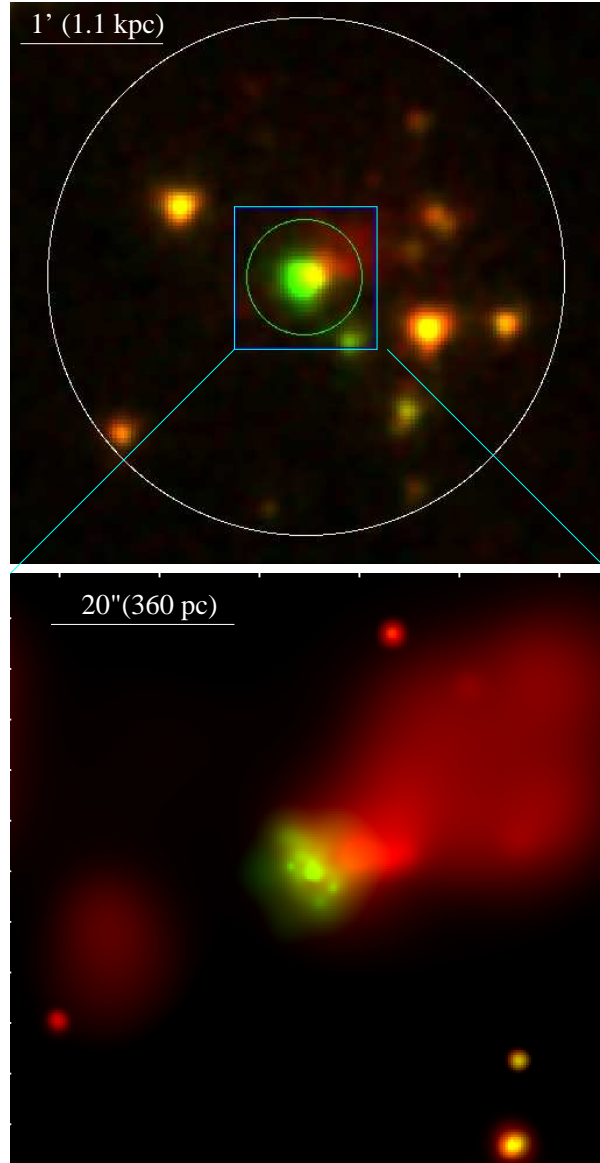


**Figure 3.1:** Upper panel: two-color (red: 0.3-2 keV; green: 2-10 keV) *XMM-Newton* image of the central 4' of NGC 4945. The bigger and smaller circles show the *Suzaku* and *XMM-Newton* spectrum extraction regions, respectively. Lower panel: same for the central arcmin, as imaged by *Chandra*.

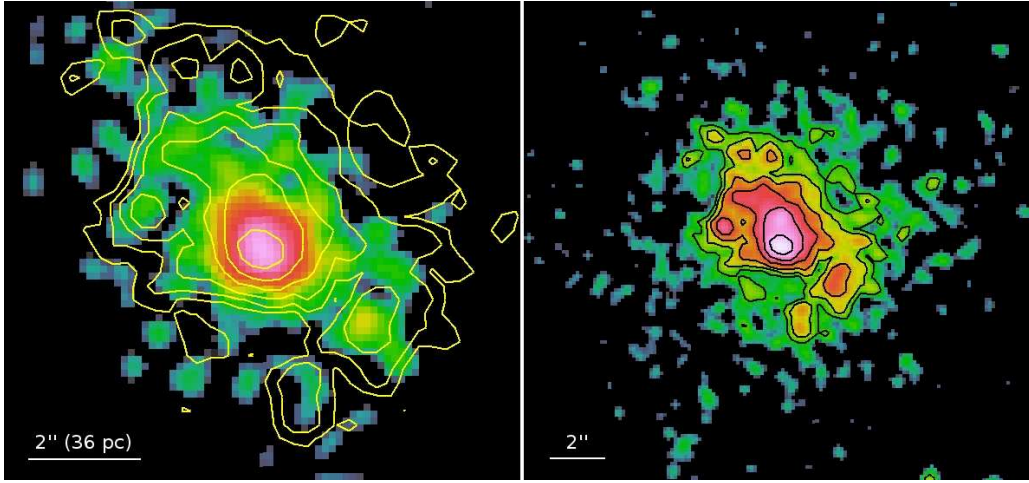


**Figure 3.2:** Image of the central region in the line emission band (6.2-6.7 keV, left) and in the hard X-ray band (right). The black (right panel) and yellow (left panel) lines represent the contours of the reflected continuum emission. It is interesting to point out that the Iron  $K\alpha$  emitting regions (left panel) well match the reflection continuum contours, leading to the conclusion that the cold reflection and the iron emission lines originate exactly from the same circumnuclear material.

observed reflection variability of  $\sim 4\%$ , corresponding to twice the dispersion, or, equivalently, to the ratio between the maximum and minimum value of  $F$  within the measured dispersion.

This result can be compared with the variability observed at higher energies. The average 15-150 keV flux of NGC 4945 is of the order of 5-10 mCrab<sup>2</sup>, therefore the *Swift*/BAT monitoring provides reliable, high S/N light curves with reasonably short time bins. In Fig. 3.3 we show the 65-month light curve, in bins of one and five months. In order to obtain a semi-quantitative estimate of the reflector distance, we modeled the circumnuclear gas as a cylinder with the axis on the plane of the sky, with radius  $R$  and height  $H$ , such that  $H/R < 0.1$ , as implied by the analysis of D03. We then used the observed BAT light curve as an input, and determined the maximum observable flux variation of the reflected component as a function of the distance  $R$ , by adding the contribution of each element of the reflector. Qualitatively, we expect that the more distant the reflector, the lower variability is observed in the reflected light curve, because the intrinsic variability is smoothed out by the different lengths of the light paths corresponding to each reflecting element. Quantitatively, the result is shown in Fig. 3.3b. In order to ob-

---

<sup>2</sup>One Crab is defined as the intensity of the Crab Nebula in the corresponding X-ray energy band.

serve a variation not larger than 4% (reminding that  $\langle F \rangle = 0.96-1.00$ ), the reflector must be at a distance larger than 35 pc. This result is obviously approximate, due to the assumptions on the geometry, and to the limited sampling of the reflection fluxes, which may have caught the source in the same reflected states by chance. However, we believe it provides a solid order of magnitude estimate of the distance of the reflector. We conclude noting that, considering that the *Chandra* resolution is  $\sim 0.25$  arcsec, ( $\sim 5$  pc at the distance of NGC 4945), the X-ray reflector should be easily resolved by *Chandra*, consistent with the conclusions of D03.

#### 3.1.3 The reflector geometry from direct imaging

In Fig. 3.1 the  $1' \times 1'$  central region of NGC 4945 is shown. After running the script CHANDRA\_REPRO on the three *Chandra* event files we merged them all with the MERGE\_ALL script and filtered them in energy between 0.3-2 keV (in red) and 2-10 keV (in green). A soft X-ray emitter can be seen in the top right region of the image, as already discussed in Schurch et al. 2002, where they called it the 'plume', reproduced by a single temperature thermal model ( $kT \sim 0.6$  keV), interpreted as a mass-loaded superwind emanated from the central nuclear starburst. With the inclusion of the two 2004 observations in the image, we notice a further soft lobe in the bottom-left direction indicating a second, possible emitter partially absorbed by a dust-lane crossing the nucleus, aligned with the clumpy structure shown in Fig. 3.2. For this analysis we refer to a future work (Marinucci et al., in prep.).

The nuclear 2-10 keV emission is embedded in a  $12'' \times 6''$  box, corresponding to a  $180 \text{ pc} \times 90 \text{ pc}$  region, which is consistent with the starburst ring traced by molecular gas (Moorwood et al. 1996, Marconi et al. 2000, Curran et al. 2001).

We performed a spectral analysis of three zones, corresponding to the *XMM-Newton* extraction region, a  $12'' \times 6''$  box, including most of the hard emission (Fig. 3.1), and a central circular region with radius  $1.5''$ . The spectra, shown in Fig. 3.4, are fitted with the same reflection model as described above, with a contribution of the additional power law decreasing from the larger to the small region. In particular: (a) the best fit model of the spectrum from the  $25''$  circle is fully consistent (in each individual parameter) with that of the *XMM-Newton* observations; (b) the spectrum from the  $12'' \times 6''$  box is again fitted with the same model, but with a relative flux of the reflection component  $F = 0.86 \pm 0.07$ , indicating that most of the reflection comes from this region, with only a remaining  $\sim 10\%$  from outer regions; (c) the model from the central annulus is fitted with a pure reflection component, with no need for the additional power law. The relative flux is  $F = 0.58 \pm 0.06$ . This shows that the reflection emission is moderately concentrated in the projected central  $\sim 30$  pc, but with a significant contribution from

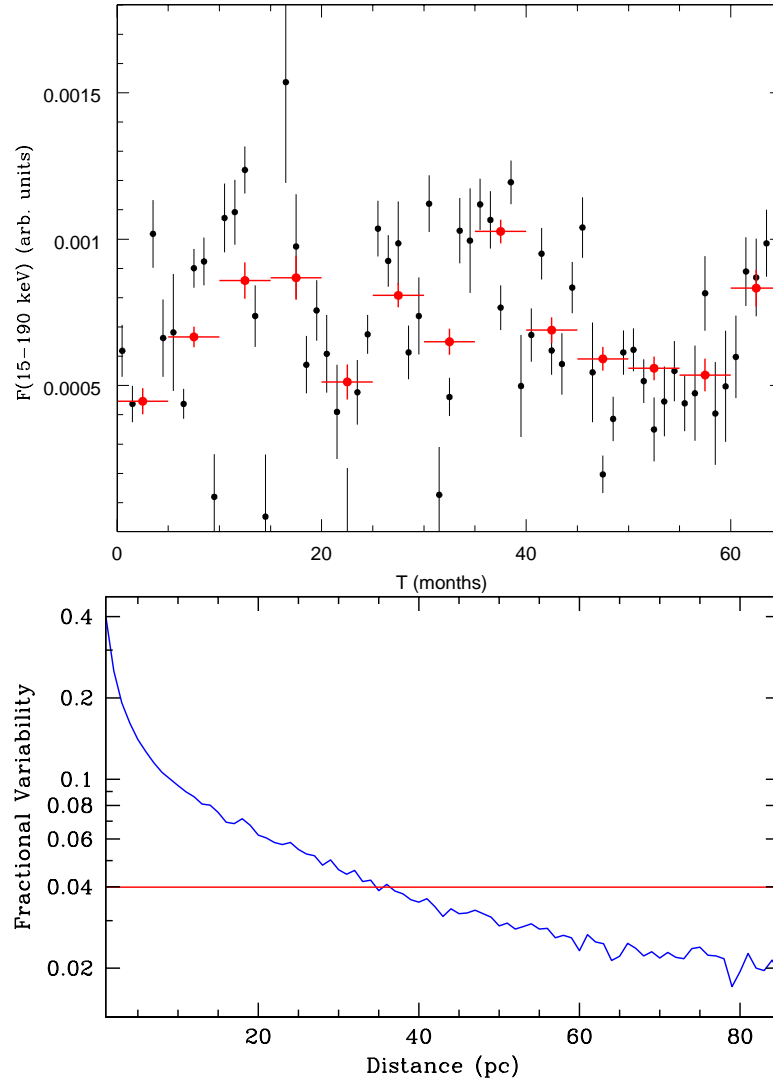


**Figure 3.3:** Upper panel: *Swift*/*BAT* light curve of the 15-195 keV emission of NGC 4945, grouped in time bins of 1 month (black) and five months (red). Lower panel: expected maximum variability as a response of a cylindrical reflector to the *BAT* light curve, as a function of the distance form the central source. The value corresponding to the upper limit to the observed reflection variability is  $\sim 35$  pc.

### Chapter 3. The circumnuclear geometry of Sy2 galaxies

Param.	Value	OBS	Date	F <sup>e</sup>
$\Gamma$	$1.6 \pm 0.1$	Suzaku 1	01/06	$1.00 \pm 0.06$
E(1) <sup>a</sup>	$6.39 \pm 0.01$	Suzaku 2	07/10	$1.00 \pm 0.08$
EW(1) <sup>b</sup>	$1020 \pm 100$	Suzaku 3	07/10	$0.99 \pm 0.08$
E(2) <sup>a</sup>	$6.66 \pm 0.01$	Suzaku 4	07/10	$0.97 \pm 0.08$
EW(2) <sup>b</sup>	$130 \pm 20$	Suzaku 5	08/10	$0.98 \pm 0.08$
E(3) <sup>a</sup>	$7.02 \pm 0.01$	Suzaku 6	01/11	$0.94 \pm 0.08$
EW(3) <sup>b</sup>	$140^{+20}_{-10}$	XMM 1	01/00	$0.97 \pm 0.05$
N <sup>c</sup>	$3.7 \pm 0.7$	XMM 2	01/04	$0.98 \pm 0.06$
F <sub>2-10</sub> <sup>d</sup>	$1.3 \times 10^{-12}$	Chandra 25''	05/04	$1.08 \pm 0.11$
L <sub>2-10</sub> <sup>d</sup>	$2.2 \times 10^{39}$	Chandra BOX	05/04	$0.86 \pm 0.07$
$\chi^2/\text{d.o.f.}$	1308/1205	Chandra 1.5''	05/04	$0.58 \pm 0.06$

**Table 3.1:** Best fit values for the reflection component. <sup>a</sup>: emission line energies, in keV; <sup>b</sup>: line equivalent widths, in eV; <sup>c</sup>: normalization in units of  $10^{-3} \text{ ph cm}^{-2} \text{ s}^{-1} \text{ keV}^{-1}$ ; <sup>d</sup>: 2-10 keV flux and luminosity of the reflection spectrum, in c.g.s. units. <sup>e</sup>: relative flux.

the outer regions. In our simple cylindrical scheme, if a small (a few degrees) inclination angle is assumed, this concentration in the central unresolved region is expected due to the projection effect, and is not related to a small physical distance from the X-ray source. A direct, complementary way to demonstrate that the hard X-ray emission is dominated by the reflected, diffuse component is by comparing the image in the full hard X-ray spectral interval (2-10 keV), with the exclusion of the 6.2-6.7 energy range, with the “iron line image” obtained filtering only the 6.2-6.7 keV spectral interval (Fig. 3.2), which is clearly dominated by the iron emission line (Fig. 3.4). We then overimposed the contours of the hard X-rays on the Iron  $K\alpha$  emitter. The striking match between these two images demonstrates that the cold reflection and the iron emission lines originate exactly from the same circumnuclear material and we are actually able to take a screenshot of the inner reflecting structure of NGC 4945.

Finally, we notice that the emission in Fig. 3.2 originates from a non homogeneous structure, with visible clumps and empty regions with sizes of the order of tens of parsecs. The differences in counts among these sub-regions are highly significant (same area regions of  $10 \times 10$  pixels contain from  $< 10$  to  $> 100$  counts). A smaller-scale clumpiness of these structures, not resolved by *Chandra*, may explain the low covering factor ( $< 10\%$ ) of the reflector, as estimated from the high intrinsic variability above 10 keV, and from the low ratio between the reflected and intrinsic components (Madejski et al. 2000).

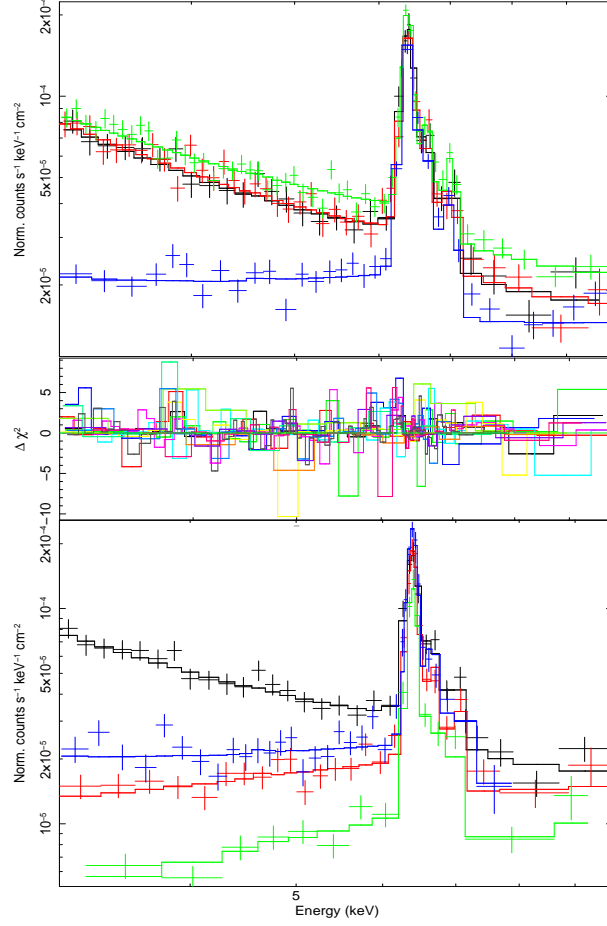


**Figure 3.4:** Spectra (rescaled to a common effective area), model and  $\Delta\chi^2$  from the observations. The  $\Delta\chi^2$  values are shown for all the spectra in the central panel, while only some of the spectra are shown, for clarity. Upper panel: first *Suzaku* observation in 2010 (black); *Suzaku* in 2011 (red), *Suzaku* in 2006 (green); *XMM-Newton* in 2004 (blue). Lower panel: the first 2010 *Suzaku* observation is shown again (black) for ease of comparison; the remaining spectra are from the *Chandra* 2004 data, extracted from a 25'' radius (blue) a 12x6'' box (red) and a 1.5'' radius circle (green). It is worth noting that the spectra between 6 and 7 keV, dominated by the iron line emission, are almost identical in all observations, except for the last one from *Chandra*, and that the total continuum decreases with the area of the extraction region. Both these features are evidence that the variability is due to the diffuse galactic component, while the reflection remains constant, as quantitatively demonstrated by the spectral fits (Table 1).

### 3.1.4 The structure of the innermost regions

The time, spectral and imaging analysis of the X-ray emission of NGC 4945 based on *XMM-Newton*, *Suzaku*, *Swift/BAT* and *Chandra* data, characterizes the AGN circumnuclear reflector with unprecedented detail.

- 1) The comparison between the strong intrinsic variability measured by *Swift/BAT* and the constant reflection spectra from *XMM-Newton* and *Suzaku* observations over more than ten years implies a distance of the reflector  $D > 35$  pc.
- 2) The *Chandra* image, obtained combining two observations performed in 2000 and 2004, reveals an extended hard emission on projected scales of  $\sim 200 \times 100$  pc. The spectrum of this emission is entirely reproduced by a cold reflection model. The central 30 pc account for about 50% of the whole emission.
- 3) We show the first X-ray image of the inner reflector of an AGN. The large scale structure of the emission region is clumpy and asymmetric, and the central region is resolved by *Chandra*. A smaller-scale, unresolved clumpiness may explain the low covering factor of the reflector inferred by the high variability of the intrinsic emission at  $E > 10$  keV, and by the low ratio between reflected and intrinsic spectrum (Madejski et al. 2000, D03).

## 3.2 The Compton-thin Sy2 NGC 4507

NGC 4507 is a nearby ( $z=0.0118$ ) barred spiral galaxy and one of the X-ray brightest Compton-thin Seyfert 2s, despite the heavy obscuration ( $N_H \sim 4 - 9 \times 10^{23} \text{cm}^{-2}$ ). It was first observed in the X-rays by Einstein ( $L_X = 2.8 \times 10^{41} \text{erg s}^{-1}$ , Kriss et al. 1980) and then in 1990 with Ginga (Awaki et al. 1991), showing a strongly absorbed ( $N_H \sim 5 \times 10^{23} \text{cm}^{-2}$ ) power law continuum and a prominent iron  $K\alpha$  line. In 1994 ASCA also revealed a strong X-ray excess and an intense emission line (identified as Ne IX) at  $\sim 0.9$  keV (Comastri et al. 1998). Risaliti (2002) reported then three BeppoSAX observations of the source, confirming the obscuring column densities observed in the previous two observations. In 2001 NGC 4507 has been observed for the first time with the most sensitive X-ray satellites, *XMM-Newton* and *Chandra/ACIS-S* HETG (Matt et al. 2004) confirming once again the clear Compton-thin state of the spectrum, with a  $\Gamma = 1.8_{-0.2}^{+0.1}$  power law absorbed by an  $N_H = 4.4_{-0.6}^{+0.5} \times 10^{23} \text{cm}^{-2}$ . In 2007 a  $\sim 3$  days observation with *Suzaku* has been performed and it revealed a much larger absorbing column density ( $N_H \sim 9 \times 10^{23} \text{cm}^{-2}$ ) with respect to the earlier observations, but no changes *within* the 3 days of monitoring (Braitto et al. 2012, hereafter B12). Summarizing, NGC 4507 showed strong variations in time scales of years (from 1990 until 2007) but none in shorter time scales (3 days observation with *Suzaku*). This excluded a possible sub-parsec scale absorbing structure, but leaves the actual size and dis-



tance of the absorber largely unconstrained. In this work we report the study of five XMM-Newton observations spanning a period of 6 weeks, between June and August 2010, and a Chandra observation performed 4 months later, in December 2010. This observational campaign has been designed to fill the time gap between days and years in the previous observations, so constraining the location of the absorber.

#### 3.2.1 Observations and data reduction

The 5 XMM-Newton observations analyzed in this work were performed on 2010 June 24 (obsid 0653870201), July 3 (obsid 0653870301), July 13 (obsid 0653870401), July 23 (obsid 0653870501), August 3 (obsid 0653870601) with the EPIC CCD cameras, the PN (Strüder et al. 2001) and the two MOS (Turner et al. 2001), operated in large window and medium filter mode, respectively. The extraction radii and the optimal time cuts for flaring particle background were computed with SAS 11 (Gabriel et al. 2004) via an iterative process which leads to a maximization of the Signal-to-Noise Ratio (SNR), similarly to that described in Piconcelli et al. (2004). After this process, the net exposure times for the 5 different observations were 16 ks, 13 ks, 13 ks, 13 ks and 17 ks for the PN, respectively. The resulting optimal extraction radii are 40 arcsec for the first three observations, 30 arcsec for the fourth one, 26 arcsec for the last one. The background spectra were extracted from source-free circular regions with a radius of about 50 arcsec for all the 5 observations. We also re-extracted the data from a previous XMM-Newton observation (obsid 0006220201), with a net exposure of about 36 ks, adopting an extraction radius of 40 arcsec for the source and 42 arcsec for the background. The analysis of the last set of data is discussed in Matt et al. (2004).

Chandra observed the source on December 2, 2010 for 44 ks, with the Advanced CCD Imaging Spectrometer (ACIS: Garmire et al. 2003). Data were reduced with the Chandra Interactive Analysis of Observations (CIAO: Fruscione et al. 2006) 4.4 and the Chandra Calibration Data Base (CALDB) 4.4.6 database, adopting standard procedures, using a 2 arcsec and 10 arcsec extraction radii for the source and background, respectively.

Spectra were binned in order to over-sample the instrumental resolution by at least a factor of 3 and to have no less than 30 counts in each background-subtracted spectral channel. This allows the applicability of the  $\chi^2$  statistics.

#### 3.2.2 Data analysis

The adopted cosmological parameters are  $H_0 = 70 \text{ km s}^{-1} \text{ Mpc}^{-1}$ ,  $\Omega_\Lambda = 0.73$  and  $\Omega_m = 0.27$ , i.e. the default ones in XSPEC 12.7.0 (Arnaud 1996). Errors



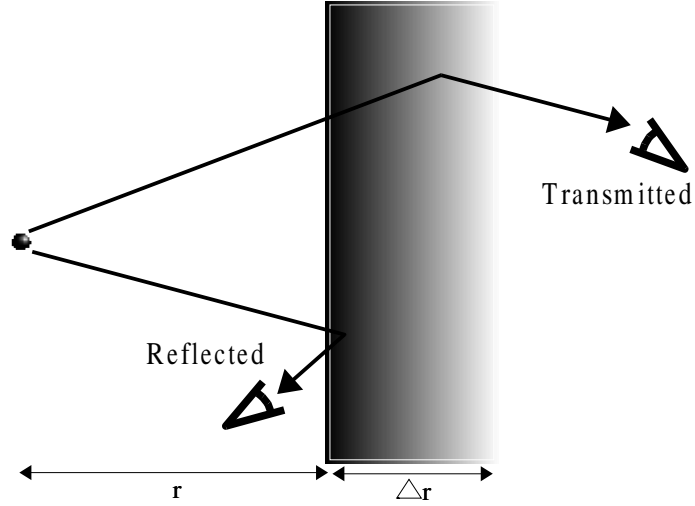


**Figure 3.5:** The adopted geometry for the photoionized reflector.

correspond to the 90% confidence level for one interesting parameter ( $\Delta\chi^2 = 2.7$ ), if not otherwise stated.

### EPIC PN+MOS spectral analysis

The soft 0.5-3.0 keV spectrum presents a strong 'soft excess', which appears dominated by emission lines from an highly ionized gas, as observed in most X-ray obscured AGN (Turner et al. 1997; Guainazzi & Bianchi 2007). Emission lines from H-like and He-like C, N, O, and Ne, as well as from the Fe L-shell, have been detected and reported in previous observations (Matt et al. 2004). Throughout this work we reproduced the soft emission in terms of a self-consistent model using the public photoionization code CLOUDY<sup>3</sup> (v94.00: Ferland 2000). It is an extension of the same model used in Bianchi et al. (2010a). The main ingredient is the ionization parameter  $U$  (Osterbrock & Ferland 2006), defined as:

$$U = \frac{\int_{\nu_R}^{\infty} \frac{L_{\nu}}{h\nu} d\nu}{4\pi r^2 c n_e} \quad (3.1)$$

where  $c$  is the speed of light,  $r$  the distance of the gas from the illuminating source,  $n_e$  its density and  $\nu_R$  the frequency corresponding to 1 Rydberg. The incident continuum has been modeled as in Korista et al. (1997), a constant electron density  $n_e = 10^5 \text{ cm}^{-3}$  has been used and elemental abundances can be found as in Table 9

<sup>3</sup><http://www.pa.uky.edu/~gary/cloudy/>

of CLOUDY documentation<sup>4</sup>. The resulting grid parameters are  $\log U = [-2.00 : 4.00]$ , step 0.25, and  $\log N_H = [19.0 : 23.5]$ , step 0.1. Only the reflected spectrum, arising from the illuminated face of the cloud, has been taken into account in our model. We also produced tables with different densities ( $n_e = 10^3 - 10^4 \text{ cm}^{-3}$ ): all the fits presented in this thesis resulted to be insensitive to this parameter, as expected since we are always treating density regimes where line ratios of He-like triplets are insensitive to density (Porquet & Dubau 2000). The adopted geometry for the photo ionized reflector can be found in Fig. 3.5.

Following Matt et al. (2004) the baseline model we used to fit the 0.5-10 keV spectra can be roughly expressed by the following general formula:

$$F(E) = e^{-\sigma(E)N_H^G} [Ph_C + C + e^{-\sigma(E)N_H} B E^{-\Gamma} + R(\Gamma) + \sum_i G_i(E)] \quad (3.2)$$

where  $\sigma(E)$  is the photoelectric cross-section (abundances as in Anders & Grevesse 1989b),  $N_H^G$  is the Galactic absorbing column density along the line of sight to the source (Dickey & Lockman 1990);  $Ph_C$  is the emission from a photoionised gas reproduced with self-consistent CLOUDY models as described in Bianchi et al. (2010a) and Marinucci et al. (2011) while  $C$  is the emission from a collisionally-ionised diffuse gas (APEC model, Smith et al. 2001);  $N_H$  is the neutral absorbing column density at the redshift of the source;  $B$  is the normalization of the primary powerlaw with slope  $\Gamma$ ;  $R(\Gamma)$  is the Compton scattering from the inner layer of the circumnuclear torus, modelled in XSPEC with PEXRAV (Magdziarz & Zdziarski 1995);  $G_i(E)$  are Gaussian profiles, corresponding to required emission lines of high-Z elements such as the Fe  $K\alpha$  at 6.4 keV, Fe  $K\beta$  at 7.058 keV, Fe XXVI at 6.966 keV and the forbidden line of the Fe XXV  $K\alpha$  triplet at 6.69 keV (see table 3.2).

A further Gaussian emission line has been used to reproduce the Compton Shoulder (CS) redwards of the Iron line core, as expected on theoretical grounds, with energy fixed at 6.3 keV and  $\sigma=40$  eV (Matt 2002).

The reflected, Compton scattered emission has been modeled using the PEXRAV model with  $\Gamma=1.8$  and normalization fixed to the values measured with the broadband Suzaku observation (B12). The previous model has been used to fit, in first place, the 5 separate EPIC PN+MOS observations. The 5 spectral fits from our campaign in Summer 2010 (labeled as Obs. 1-5 in Table 3.2) have good  $\chi^2/\text{d.o.f.}$  and do not present any strong evidence of variations in either the absorbing column density or  $\Gamma$ .

Two different photoionised phases and a collisional one are needed to model the 0.5-3.0 keV spectra of NGC 4507. Table 3.2 clearly shows that the soft X-ray emitting gas has not varied during the monitoring. This suggests that the

---

<sup>4</sup>Hazy 1 version 08, p. 67: [http://viewvc.nublado.org/index.cgi/tags/release/c08.00/docs/hazy1\\_08.eps?revision=2342&root=cloudy](http://viewvc.nublado.org/index.cgi/tags/release/c08.00/docs/hazy1_08.eps?revision=2342&root=cloudy)

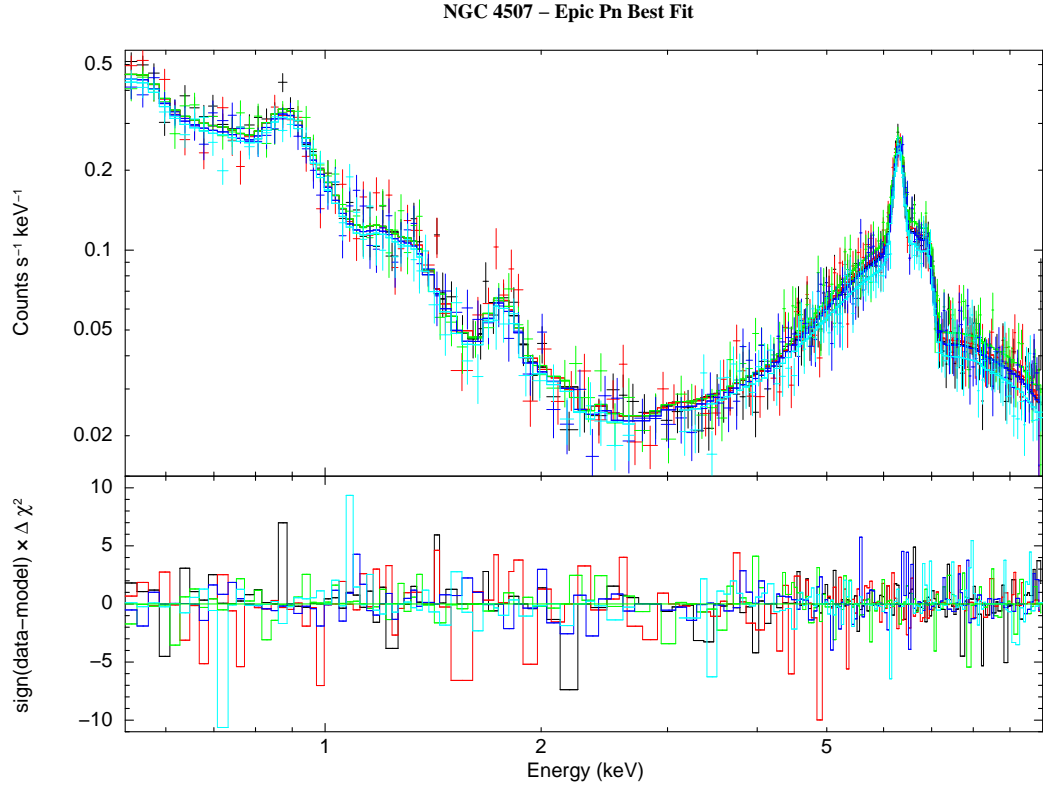


**Figure 3.6:** XMM-Newton EPIC PN 0.5-10 keV best fit and ratio for the 5 observations of the campaign described in this work.

absorbing material, responsible for the column density variation between June and December 2010, might be much closer to the X-ray source than the circumnuclear matter responsible for the soft emission. As already discussed in Bianchi et al. (2006) and Bianchi & Guainazzi (2007) this gas is likely coincident with the NLR. Further studies on the photoionisation mechanisms and extended emission in NGC 4507 will be discussed in detail in the future (Wang et al., in preparation).

We then analyzed the 10 spectra (5 EPIC PN and 5 MOS1+2, labeled as Set 1 in Table 1) simultaneously, using the model described above and linking all the parameters, except for the flux normalizations. The baseline model reproduces the 5 sets of data and some residuals are present around 1.8 keV. Indeed, the addition of a line at  $1.77 \pm 0.03$  keV is required ( $\Delta\chi^2 = 44$ , with a significance greater than 99.99%, according to  $F$ -test<sup>5</sup>.); it can be identified as Si  $K\alpha$ , with a corresponding

<sup>5</sup>The  $F$ -test is not a reliable test for the significance of emission lines unless their normalizations are allowed to be negative (Protassov et al. 2002)

flux of  $2.0 \pm 0.4 \times 10^{-6}$  ph cm $^{-2}$  s $^{-1}$ . The primary power law ( $\Gamma = 1.8_{-0.2}^{+0.2}$ ) is absorbed by a column density of  $9.0 \pm 0.5 \times 10^{23}$  cm $^{-2}$ . The photon index is in agreement with previous studies on this source, on the contrary a clear variation in the  $N_H$  can be noticed with respect to the old 2004 XMM-Newton observation, but it is fully compatible with the Suzaku observation in 2007 (Fig. 3.11). The addition of a CS redwards of the Iron K $\alpha$  line core is required by the fit ( $\Delta\chi^2 = 20$  with a significance greater than 99.99%) and its flux, being  $24 \pm 7\%$  of the flux of the narrow core of the Fe K $\alpha$ , is consistent with expectations. Both Iron K $\alpha$  and CS fluxes are in agreement with the ones found in the previous XMM observation (Matt et al. 2004). The equivalent widths of the high energy emission lines are in full agreement with the ones we find when we analyze the 5 sets of data separately. We only find upper limits on fluxes ( $< 0.5 \times 10^{-6}$  ph cm $^{-2}$  s $^{-1}$ ) and EWs ( $< 50$  eV) of the Fe XXVI emission lines at 6.966 keV.

As a last cross-check, we let the 5 different absorbing column density parameters free to vary in our fit, to check whether a possible variation may have been occurred in the 1.5 months monitoring. The best fit values of the 5 different  $N_H$  do not show any significant variation with respect to the best fit value for the whole data set ( $9.0 \pm 0.5 \times 10^{23}$  cm $^{-2}$ ) with a non significant improvement of the fit ( $\Delta\chi^2 = 5$  with four more parameters and a significance lower than 8%). This result brings further evidence to the argument that absorption variability on short time scales (hours-days) can be ruled out in our analysis of NGC 4507. If the intervening absorbing material had varied on such short time scales we would not have measured a constant column density in a 1.5 months monitoring. The measured values would have been completely scattered over the range of values observed in the past ( $4 - 9 \times 10^{23}$  cm $^{-2}$ ).

#### **Chandra ACIS spectral analysis**

The baseline model is the same we used to fit the XMM-Newton data. The overall fit is very good ( $\chi^2 = 327/329$ ) and the addition of a further emission line at  $1.81 \pm 0.02$  keV is required ( $\Delta\chi^2 = 14$  with a significance greater than 99.99%), with a flux of  $4_{-2}^{+1} \times 10^{-6}$  ph cm $^{-2}$  s $^{-1}$ , marginally consistent with the emission from Si K $\alpha$  already found in XMM-Newton best fits. The soft X-ray spectrum is produced by two photoionised phases, while the contribution by a collisional gas is not required by the fit. Equivalent widths, fluxes and energy centroids of the emission lines found in the 5 - 7.5 keV energy range are fully consistent with the results reported above. Best fit values are shown in Table 3.2 and the column is labeled as Obs. 6.

The reflected primary continuum has been fitted as described before (see Sect. 3.2.2): the best fit value of the absorbing column density is  $6.5 \pm 0.7 \times 10^{23}$  cm $^{-2}$ , leading to a  $2.5 \times 10^{23}$  cm $^{-2}$  variation at a  $3\sigma$  confidence level in a time scale

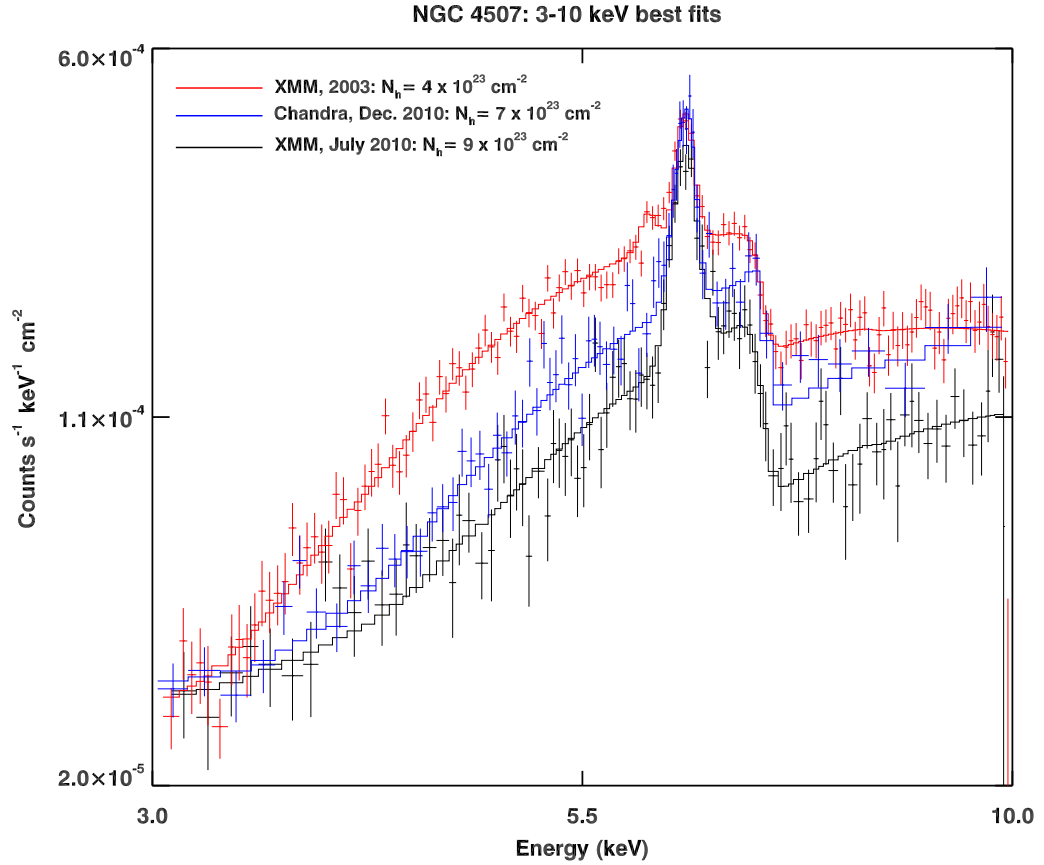


**Figure 3.7:** 3-10 keV best fits. The impact of the variation in the absorbing column density on the three spectra can be clearly seen.

ranging between 1.5 (time interval between the first and the fifth XMM-Newton observation) and 4 months (time interval between the last XMM-Newton observation and the one with Chandra). In Fig. 3.7 we show the influence of the change in  $N_H$  on the spectral shape between 3 and 10 keV. Considering the partial degeneracy between the column density and the spectral slope, the significance of the variation is even stronger, as illustrated by the  $\Gamma$ - $N_H$  contour plots shown in Fig. 3.8.

### 3.2.3 Discussion on the column density variability

In the past few years a great number of sources have been monitored and spectral changes from Compton-thin ( $N_H$  of units in  $10^{23} \text{ cm}^{-2}$ ) to reflection dominated ( $N_H > 10^{24} \text{ cm}^{-2}$ ) on time scales from a couple of days to  $\sim 10$  hours have been de-

### 3.2. The Compton-thin Sy2 NGC 4507

Parameter	Obs. 1	Obs. 2	Obs. 3	Obs. 4	Obs. 5	Obs. 6	Set 1
K (PN-MOS)	$0.99^{+0.02}_{-0.02}$	$1.06^{+0.03}_{-0.03}$	$1.02^{+0.03}_{-0.03}$	$1.02^{+0.03}_{-0.03}$	$0.93^{+0.03}_{-0.03}$	-	-
$N_H$ ( $10^{23} \text{ cm}^{-2}$ )	$8.7^{+0.7}_{-0.8}$	$9.7^{+0.9}_{-0.9}$	$7.6^{+1.0}_{-1.3}$	$9.4^{+1.1}_{-1.1}$	$8.0^{+0.8}_{-0.6}$	$6.5^{+0.7}_{-0.7}$	$9.0^{+0.5}_{-0.5}$
$\Gamma$	$1.8^{+0.1}_{-0.1}$	$2.0^{+0.3}_{-0.3}$	$1.4^{+0.4}_{-0.3}$	$1.9^{+0.3}_{-0.3}$	$1.6^{+0.3}_{-0.4}$	$1.5^{+0.4}_{-0.4}$	$1.8^{+0.2}_{-0.2}$
F (CS <sub>6.3</sub> keV)	< 1.5	< 1.7	$1.8^{+0.7}_{-0.9}$	$1.4^{+0.7}_{-0.8}$	$0.8^{+0.4}_{-0.4}$	$2.0^{+0.9}_{-1.1}$	$1.0^{+0.2}_{-0.2}$
Fe K $\alpha$ E	$6.40^{+0.01}_{-0.01}$	$6.40^{+0.01}_{-0.01}$	$6.41^{+0.02}_{-0.02}$	$6.41^{+0.01}_{-0.02}$	$6.40^{+0.02}_{-0.02}$	$6.40^{+0.02}_{-0.02}$	$6.401^{+0.003}_{-0.003}$
Flux	$4.4^{+0.3}_{-0.4}$	$3.8^{+0.5}_{-0.5}$	$3.7^{+0.7}_{-0.7}$	$4.3^{+0.6}_{-0.7}$	$4.6^{+0.5}_{-0.5}$	$4.0^{+0.9}_{-1.0}$	$4.2^{+0.3}_{-0.2}$
EW	$315^{+15}_{-35}$	$250^{+40}_{-40}$	$245^{+35}_{-45}$	$285^{+40}_{-45}$	$335^{+40}_{-35}$	$220^{+50}_{-40}$	
Fe K $\beta$ E	7.058	7.058	7.058	7.058	7.058	7.058	7.058
Flux	< 0.6	< 0.5	< 0.6	< 0.5	< 0.8	< 1.1	$0.3^{+0.2}_{-0.2}$
EW	< 50	< 35	< 45	< 40	< 70	< 70	
Fe XXV E	6.700	6.700	6.700	6.700	6.700	6.700	6.700
Flux	$0.6^{+0.3}_{-0.4}$	< 0.3	$0.7^{+0.4}_{-0.4}$	< 0.7	< 0.3	< 0.4	$0.3^{+0.1}_{-0.1}$
EW	$40^{+20}_{-25}$	< 20	$45^{+25}_{-25}$	< 45	< 20	< 20	
kT (keV)	$0.43^{+0.12}_{-0.08}$	$0.53^{+0.30}_{-0.25}$	$0.44^{+0.26}_{-0.15}$	$0.43^{+0.17}_{-0.15}$	$0.42^{+0.12}_{-0.12}$	-	$0.43^{+0.11}_{-0.07}$
$\log U_1$	$1.63^{+0.05}_{-0.05}$	$1.59^{+0.10}_{-0.07}$	$1.75^{+0.05}_{-0.10}$	$1.59^{+0.11}_{-0.07}$	$1.67^{+0.07}_{-0.10}$	$1.85^{+0.20}_{-0.12}$	$1.64^{+0.04}_{-0.04}$
$\log N_{H1}$	$20.5^{+0.2}_{-0.2}$	$20.9^{+0.3}_{-0.2}$	$20.9^{+0.2}_{-0.2}$	$21.1^{+0.4}_{-0.3}$	$20.8^{+0.4}_{-0.3}$	$21.9^{+0.8}_{-0.6}$	$21.0^{+0.1}_{-0.2}$
$\log U_2$	$-0.69^{+0.10}_{-0.25}$	$-0.18^{+0.28}_{-0.23}$	$-0.45^{+0.30}_{-0.25}$	$-0.47^{+0.64}_{-0.82}$	$0.30^{+0.30}_{-0.50}$	$0.90^{+0.10}_{-0.40}$	$-0.15^{+0.21}_{-0.25}$
$\log N_{H2}$	$19.9^{+0.1}_{-0.3}$	$20.4^{+0.5}_{-0.5}$	< 19.8	$19.8^{+0.5}_{-0.5}$	$19.9^{+0.3}_{-0.5}$	$21.52^{+0.10}_{-0.10}$	$19.9^{+0.2}_{-0.3}$
F <sub>0.5–2 keV</sub>	$0.4^{+0.1}_{-0.1}$	$0.4^{+0.1}_{-0.1}$	$0.4^{+0.2}_{-0.2}$	$0.4^{+0.1}_{-0.1}$	$0.4^{+0.2}_{-0.1}$	$0.3^{+0.2}_{-0.2}$	
F <sub>2–10 keV</sub>	$7.7^{+0.3}_{-0.3}$	$8.0^{+0.3}_{-0.3}$	$8.4^{+0.2}_{-0.2}$	$8.0^{+0.3}_{-0.3}$	$7.5^{+0.8}_{-0.6}$	$10.0^{+0.4}_{-0.4}$	
$\chi^2/\text{d.o.f.}$	308/292	347/268	242/272	267/267	280/283	313/327	1576/1459

**Table 3.2:** Best fit values. Energies are in keV, line fluxes in  $10^{-5} \text{ ph cm}^{-2} \text{ s}^{-1}$ , observed fluxes in  $10^{-12} \text{ erg cm}^{-2} \text{ s}^{-1}$  and EWs in eV. Photoionisation parameters  $\log U_1$ ,  $\log U_2$  and column densities  $\log N_{H1}$ ,  $\log N_{H2}$  are the best fit values of the two photoionised phases needed to reproduce the soft emission; kT is the energy of the additional collisional phase (see text for detail).

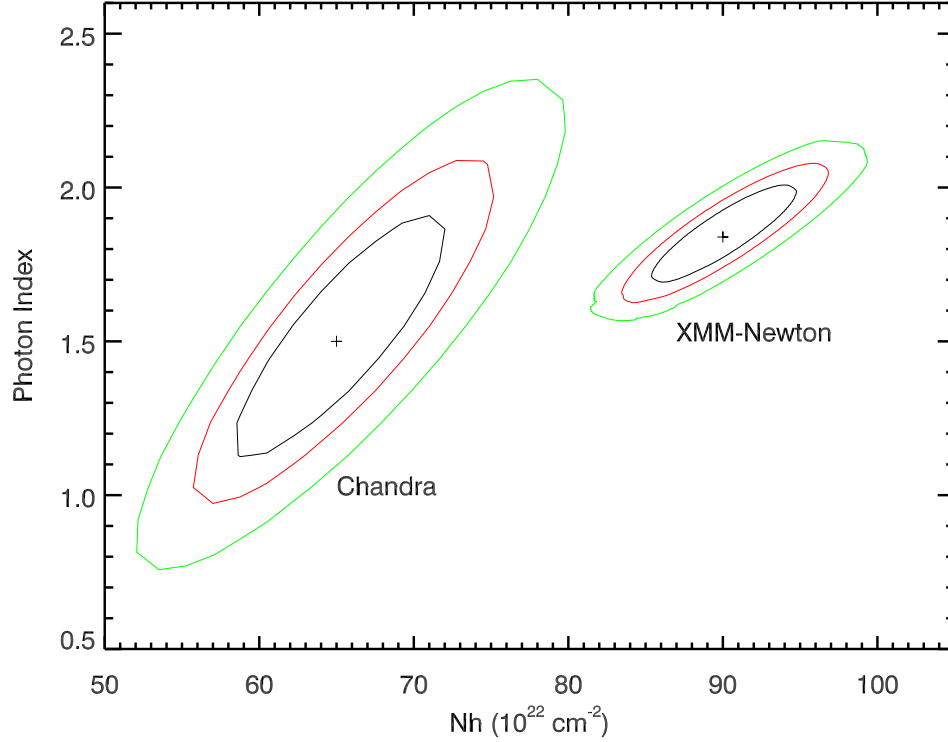


**Figure 3.8:**  $\Gamma$ - $N_H$  contour plots of the 5 combined XMM-Newton observations and the *Chandra* December 2010 observation. Solid black, red and green lines corresponds to  $1\sigma$ ,  $2\sigma$ ,  $3\sigma$  confidence levels, respectively.

tected. Such rapid events imply that the absorption is due to clouds with velocity  $v > 10^3 \text{ km s}^{-1}$ , at distances from the central BH of the order of  $10^4$  gravitational radii (assuming that they are moving with Keplerian velocity around the central black hole). The physical size and density of the clouds are estimated to be of the order of  $10^{13} \text{ cm}$  and  $10^{10} - 10^{11} \text{ cm}^{-3}$ , respectively. All these physical parameters are typical of BLR clouds, strongly suggesting that the X-ray absorber and the clouds responsible for broad emission lines in the optical/UV are one and the same. Maiolino et al. (2010) investigated the case of NGC 1365 and succeeded in drawing a physical scenario that correctly reproduces the observed X-ray variability. During two eclipses they revealed a 'cometary' shape of the obscuring cloud, consisting of a high density head, and an elongated, lower density tail. This structure was discovered by the time evolution of the two key observational parameters of the cloud (Fig. 3.9): its covering factor to the X-ray source (suddenly increas-

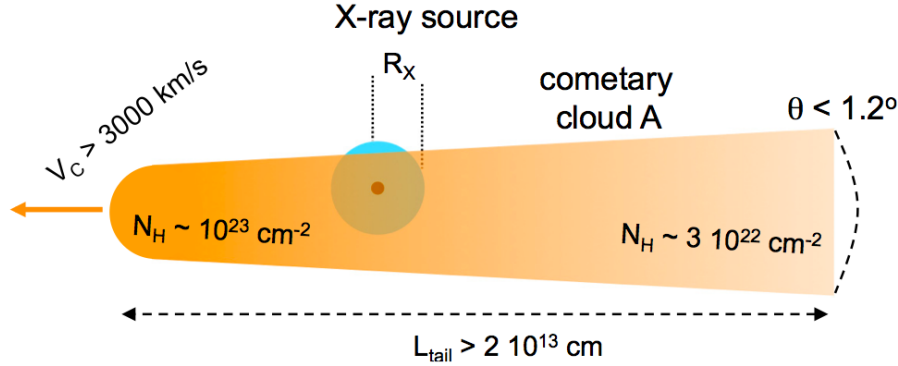


**Figure 3.9:** Structure of the absorbing cloud as obtained from a Suzaku observation of NGC 1365. The cloud size is not in the correct scale: the tail is much longer when compared with the source size, which is of the order of a few  $10^{11}$  cm, from Maiolino et al. (2010).

ing at the beginning of the occultation, then slowly increasing over a relatively long time interval), and its column density (highest at the beginning of the occultation, and then decreasing steadily).

From the X-ray data analysis presented in the previous sections on NGC 4507 a column density variation in a time scale of months is evident. We are going to describe, in the following, the physical implications of this result. Changes in absorbing column density are due to two different physical processes: a variation of the ionizing primary radiation, which causes the variation in the ionization state of the absorber or variations in the amount of absorbing gas along the line of sight. In the case of NGC 4507 the first physical scenario can be clearly ruled out because the difference in the 2-10 keV fluxes between the observations is not significant enough to justify a variation in the primary ionizing radiation. The black hole mass of NGC 4507 is estimated by means of stellar velocity dispersion to be  $4.5 \times 10^7 M_\odot$  (Marinucci et al. 2012). We assume the dimensions of the X-ray emitting source  $D_S$  to be  $10 R_G$ . This is in agreement with continuum variability studies and disk-corona emission models, all suggesting a compact central X-ray source, confined within a few  $R_G$  from the central black hole. In the case of NGC 4507 we are not able to measure the covering factor of each crossing cloud, therefore we will assume a very simple geometry, where the size of the obscuring cloud  $D_C \sim D_S$ . A schematic view of the geometrical structure is shown in Fig. 3.10. The transverse velocity  $v_K$  for one obscuring cloud is then simply given by the linear dimension of the X-ray source,  $D_S$ , divided by the crossing time:



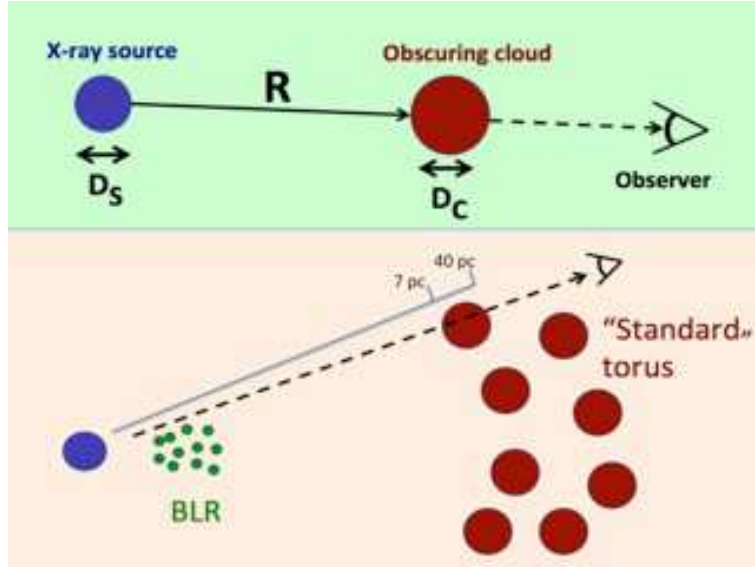


**Figure 3.10:** Schematic view of the circumnuclear absorbing structure in NGC 4507.

$$v_K = \frac{D_C}{T_{cr}} \simeq \frac{10 GM_{bh}}{c^2 T_{cr}} \simeq 70 \text{ km s}^{-1} M_{7.65} T_4^{-1}, \quad (3.3)$$

where we introduced the adimensional parameters  $M_{7.65} = M_{bh}/10^{7.65} M_\odot$  and  $T_4 \simeq 1 \times 10^7 \text{ s} = 4 \text{ months}$ .

If we then consider the absorbing material located at a distance  $R$  from the central X-ray source, moving with Keplerian velocity, we can calculate  $R$  with the simple formula:

$$R = \frac{GM_{bh}}{v_K^2} = \frac{GM_{bh} T_{cr}^2}{10^2 R_G^2} \simeq 40 \text{ pc } M_{7.65} R_{10}^{-2} T_4^2, \quad (3.4)$$

where  $R_{10} = D_S/10 R_G$ . In the case of NGC 4507 the lower limit on the crossing time is 1.5 months, the time interval between the first and last observation of our XMM-Newton campaign, during which the column density is maximal and nearly constant. The upper limit to the uncovering time ( $\sim D_S/v_K$ ) is 4 months, time interval between the fifth XMM-Newton observation (August 2011) and the Chandra one (December 2011).

Using these limits in the relations above we get a lower limit of  $R = 7 \text{ pc } M_{7.65} R_{10}^{-2}$  and an upper limit of  $R = 40 \text{ pc } M_{7.65} R_{10}^{-2}$ . These distances imply that the obscuring material is located well outside the BLR: to be consistent with the BLR

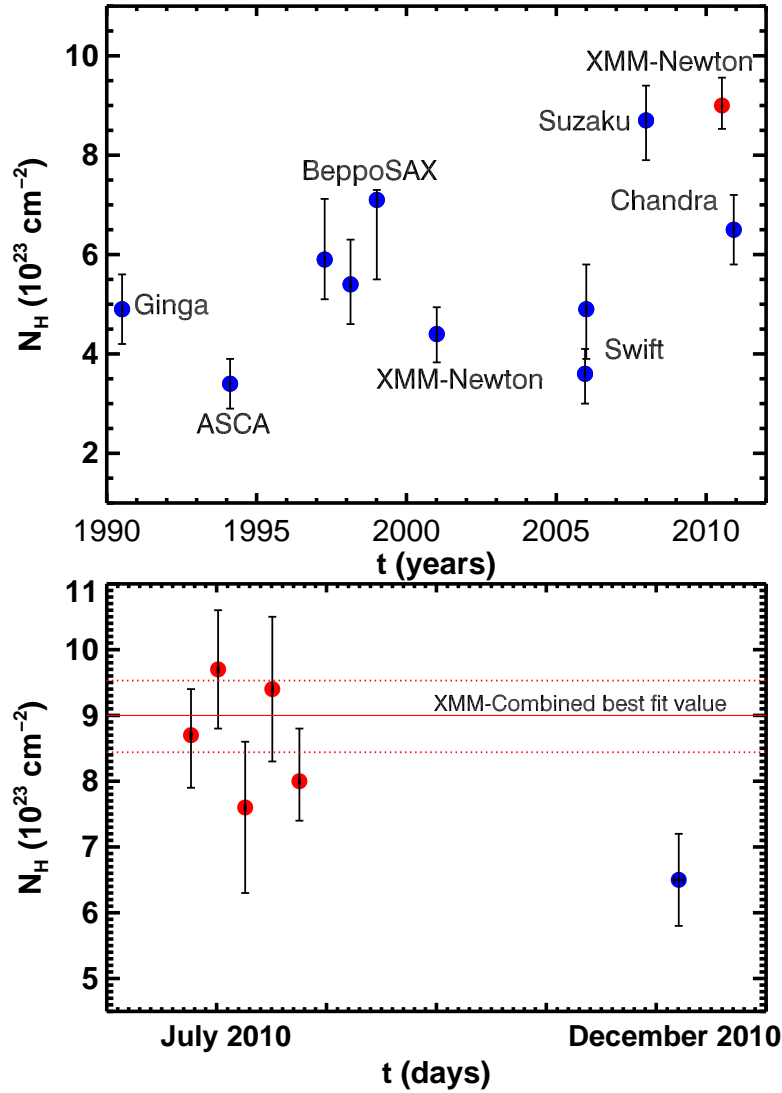


**Figure 3.11:** Column density light curves. (a) From 1990 until now the source has presented several  $N_H$  variations. Values are taken from Risaliti et al. (2002). A clear changing-look on time scales of years has been already discussed in B12, while for the first time a column density variation has been observed on time scales of months. (b) Column density light curve from June 2010 to December 2010. The 5 XMM-Newton observations do not show any evidence of variation in  $N_H$ , while the Chandra value clearly differs from the XMM combined best fit value, which is plotted as a red solid line with errors as red dashed lines.

location the obscuring cloud should have a linear size  $D_C > 20D_S$ . If we assume a typical BLR density  $n_e \sim 10^9 \text{ cm}^{-3}$  (Osterbrock 1989) and a  $N_H = 2.5 \times 10^{23} \text{ cm}^{-2}$  (difference between XMM-Newton and Chandra spectra) we get a linear size for the obscuring cloud  $D_C < 3.5 D_S$ : these two values are clearly inconsistent. The Suzaku observation is the only one that really probes the typical BLR timescales in NGC 4507, but with an average column density of  $\sim 10^{24} \text{ cm}^{-2}$  it is not possible to disentangle any inner component with  $N_H \sim 10^{22} - 10^{23} \text{ cm}^{-2}$ .

We reduced and analyzed two 10ks long Swift-XRT observations on the 24<sup>th</sup> and 30<sup>th</sup> of December 2005 (OBSID 00035465001 and 00035465003 respectively), to check for column density variations on timescales of days. The baseline model we used to reproduce the data is a simple absorbed power law, a gaussian emission line and a further soft power law for spectral features below  $\sim 3 \text{ keV}$ . Data quality does not allow for a clear investigation of the  $\Gamma$ - $N_H$  parameter space, so we adopted a fixed value of  $\Gamma = 1.8$ . Only a marginal column density variation (at  $1\sigma$  confidence level) is found between the two Swift observations but the two measurements of  $N_H$  are consistent at the 90% confidence level (Fig. 3.11). The lack of significant variability on short time scales does not imply that a BLR component does not exist at all, it suggests indeed a much more complex environment of absorbing structures, as already discussed in Nardini & Risaliti (2011) for the dwarf Seyfert galaxy NGC 4395.

The obscuring clouds' velocities we measured (70-170 km/s  $M_{7.65}$ ) are at least one order of magnitude smaller than the typical BLR clouds' velocities. The absorption variability is due to circumnuclear material which is located at distances consistent with the putative torus (Antonucci 1993). Such material cannot be located at much larger scales (i.e. dust lanes) since the NLR is not significantly affected by reddening, as inferred by the observed  $H\alpha/H\beta$  ratio (Kewley et al. 2001).

Since the presence of a Compton-thick material around the nucleus is invariably accompanied by a neutral iron narrow  $K\alpha$ -emission line and a cold reflection emission it is interesting to point out the fact that the spatial scale of the obscuring material in NGC 4507 is consistent with the distance of the reflector observed with *Chandra* in the nearby Compton-thick Sy2 NGC 4945 (Marinucci et al. 2012).

The existence of a more complex structure surrounding the central engine of AGN rather than the one predicted by the unification model has been proposed and widely discussed in the past few years (Maiolino & Rieke 1995; Elvis 2000; Matt 2000) and recently in Bianchi et al. (2007); Risaliti & Elvis (2010); Bianchi et al. (2012); Elvis (2012).

Accordingly to these models, only absorbing matter on very different scales can be responsible for the wide phenomenology of column density variations, leading to an overall scenario where different absorbers/reflectors are responsible for the spectral changes in the Seyfert 2 galaxies observed so far.

The column density variation we measured in NGC 4507 is a further piece that can be added to the puzzle. In our analysis the lack of any variation on short time scales (hours, days) excludes an absorber located in the BLR while the change on time scales of months leads to an absorber much farther from the X-ray source, differently with respect to other variable objects (e.g. NGC 1365, NGC 4151, UGC 4203: Risaliti et al. 2005, 2007, 2009; Puccetti et al. 2007; Risaliti et al. 2010) on long time scales (months, years) and rapidly changing on short ones observed so far. Our analysis provides further evidence that a universal circumnuclear structure of absorbing matter is therefore not suited for taking into account all the observed phenomenology on absorption variability in AGN. While it is true that absorption must occur on different scales, not all the objects present evidence of absorption from all the possible scales.

#### 3.2.4 The circumnuclear environment

We reported the analysis of 5 XMM-Newton observations spanning a period of 6 weeks and a Chandra observation performed 4 months afterwards of the obscured AGN in NGC 4507. This source had shown strong column density variations in time scales of years (from 1990 until 2007) and none in shorter time scales during the 3 days of Suzaku monitoring. We therefore investigated time scales ranging from 1.5 up to 4 months, looking for absorbing structures located farther from the innermost X-ray source.

Our results can be summarized as follows:

- a column density variation of  $|\Delta N_{\text{H}}| = 2.5 \times 10^{23} \text{ cm}^{-2}$  at a  $3\sigma$  confidence level on a time interval between 1.5 and 4 months has been measured. Such time scales lead to distances of the absorber ranging from  $R = (7 - 40) M_{7.65} R_{10}^{-2} \text{ pc}$  with corresponding velocities of  $70 - 170 \text{ km/s}$   $M_{7.65}$ . These distances imply that the obscuring material is located well outside the BLR, and suggest a much more complex environment of absorbing structures;
- the distances we inferred suggest that a single, universal structure of the absorber is not enough to reproduce the X-ray absorption variability of this AGN. Different reflectors/absorbers are responsible for the observed X-ray features.

In the next future, following the results presented in Risaliti (2002), a monitoring of all the sources that have shown changes on time scales of years but none on shorter (hours-days) can be performed. A broad band, time-resolved study of

### **Chapter 3. The circumnuclear geometry of Sy2 galaxies**

---

AGN is fundamental for a better understanding of the complex circumnuclear material and its interaction and response to the primary radiation.

# Chapter 4

## Conclusions

The aim of this thesis was to investigate the complex circumnuclear environment of AGN by analyzing the X-ray spectra of Seyfert 2 galaxies. The peculiar features arising from the reprocessing of the nuclear radiation by such a circumnuclear material provide unique information on the physics of accretion onto the central SMBH and the geometrical structure of AGN.

In the framework of the first topic we studied the connection between the presence of Polarized Broad Lines and the accretion rate in a sample of 39 Seyfert 2s. We tested the model proposed by Nicastro (2000) in the least possible biased observational way, by collecting the 'cleanest' possible sample of Seyfert 2 galaxies with the best spectropolarimetric data available at the moment, and robust estimates of their BH masses performed homogeneously on the basis of the observed stellar velocity dispersion. Our results can be summarized as follows:

- **The accretion rate is the main parameter which drives the presence of HBLRs in Seyfert 2 galaxies.** We find that the separation between HBLR and non-HBLR Compton-thin sources is highly significant both in accretion rate ( $\log \lambda_{edd} = -1.9$ ) and bolometric luminosity ( $\log L_{bol} = 43.90$ ): a two-sample Kolmogorov-Smirnov test gives probabilities of 0.1% and 0.5% that the two classes are taken from the same parent population, respectively. In particular, no HBLR is found below the threshold Eddington rate  $\log \lambda_{edd} = -1.9$ , and no non-HBLR above the same limit.
- **The inclusion of Compton-thick sources blurs the separation between HBLR and non-HBLR, but still no HBLR source falls below the Eddington ratio threshold.** When Compton-thick sources are included, probabilities of chance separation rise to 1.0% and 1.8%, for Eddington ratio and bolometric luminosity, but no HBLR is still found at accretion rates lower than the threshold.

- **The seminal observational results presented in Nicastro et al. (2003) has been significantly expanded in our work.** Our results agree with the ones discussed in their work but with a much higher statistical significance, due to the larger sample used, and a greater robustness due to the more reliable estimates of the BH masses that we derive here. BH masses can be derived through a variety of different means (e.g. FWHM[OIII],  $\sigma^*$ ). Using all of these possible means, obviously allows for large samples to be assembled. However, building samples with black-hole mass determinations derived with different methods introduces significant sources of uncertainties, which may wash out possible correlations among important physical parameters, like the source accretion rate or luminosity.
- **Non-HBLR Compton-thick sources with high accretion rate may possess a BLR, but their heavy absorption is preventing us from observing it even in polarized light.** A significant fraction (64%) of Compton-thick non-HBLRs have accretion rates higher than the threshold found for Compton-thin sources ( $\log \lambda_{edd} = -1.9$ ). We speculate that this is not due to the lack of BLRs, but to heavy line-of-sight absorption preventing us from observing not only the direct line emission, but also their polarized light scattered by an, at least partly, obscured population of warm electrons.
- **[OIV] emission line luminosities, even if they are still an indirect proxy of the nuclear continuum emission, are more reliable than [OIII] luminosities as tracers of the intrinsic nuclear emission.** We compared the results obtained from our X-ray analysis with the ones derived by using different proxies of the nuclear emission: [OIII] and [OIV] emission line luminosities. A large number of sources in our sample (32 out of 39) have [OIV] measurements and both bolometric luminosities and accretion rates can be inferred. The two classes show a more significant separation in accretion rate than in bolometric luminosity (probability of chance separation of 1.1% and 10.4%, respectively). Both HBLR and non-HBLR Compton thick sources are included in the sample and the separation between the two different populations in accretion rate resembles the one inferred from our X-ray analysis. The same analysis performed by using [OIII] luminosities does not show any separation between the two samples. This suggests that the efforts to use standard extinction correction for [OIII] are not always reliable, as already discussed in Goulding & Alexander (e.g. 2009); LaMassa et al. (e.g. 2010).

While the first part of my work is focused on the statistical study of a small, accurately selected, sample of galaxies in the second one we investigated the circum-nuclear geometrical structure of two bright, nearby galaxies, by studying X-ray

---

absorption variability in their spectra. Indeed, a powerful tool to investigate structure, composition and distance from the central nucleus of the several absorbers is the study of column density variability through time-resolved X-ray spectroscopy.

## NGC 4945

A time, spectral and imaging analysis of the X-ray inner structure of NGC 4945 has been performed, revealing its geometrical structure with unprecedented detail. Such a monitoring has been possible thanks to a new *Suzaku* campaign of 5 observations spanning 6 months, together with past *XMM-Newton*, *Chandra* and *Swift* observations. In the following we summarize our results:

- **The innermost reflecting structure in NGC 4945 is at a distance greater than 35 pc.** The work presented here expands the results presented in the past, through the comparison between the intrinsic variability *above* 10 keV (from *Swift/BAT* observations), and the reflection variability *below* 10 keV (from a set of 8 *XMM-Newton* and *Suzaku* observations over a period of  $\sim 10$  years). Comparing the observed reflection variability, constrained to be within 4%, with the variability observed at higher energies we calculate the minimum distance of the reflecting material, needed to smooth out such a high energy variability.
- **The central 30 pc account for about 50% of the whole neutral reflection emission.** The *Chandra* image, obtained combining two observations performed in 2000 and 2004, reveals an extended hard emission on projected scales of  $\sim 200 \times 100$  pc. The spectrum of this emission is entirely reproduced by a cold reflection model.
- **We show one of the first X-ray images of the inner reflector of an AGN.** A complementary way to demonstrate that the hard X-ray emission is dominated by the reflected, diffuse component is by comparing the image in the full hard X-ray spectral interval (2-10 keV), with the “iron line image” obtained filtering only the 6.2-6.7 keV spectral interval. The striking match between these two images demonstrates that the cold reflection and the iron emission lines originate exactly from the same circumnuclear material and we are actually able to take a screenshot of the inner reflecting structure.
- **The inner reflecting region is clumpy and inhomogeneous.** The neutral reflected emission originates from an inhomogeneous structure, with visible clumps and empty regions with sizes of the order of tens of parsecs. The differences in counts among these sub-regions are highly significant (same area regions of  $10 \times 10$  pixels contain from  $< 10$  to  $> 100$  counts). A



smaller-scale clumpiness of these structures, not resolved by *Chandra*, may explain the low covering factor ( $<10\%$ ) of the reflector, as estimated from the high intrinsic variability above 10 keV, and from the low ratio between the reflected and intrinsic components.

## NGC 4507

This source has showed strong column density variations on time scales of years (from 1990 until 2007) but none on shorter time scales (3 days observation with *Suzaku*). This argues against a possible sub-parsec scale absorbing structure, but leaves the actual size and distance of the absorber largely unconstrained. In this work we reported the study of five XMM-Newton observations spanning a period of 6 weeks, between June and August 2010, and a Chandra observation performed 4 months later, in December 2010. This observational campaign has been designed to fill the time gap between days and years in the previous observations, so constraining the location of the absorber. Let us summarize the main results of our analysis in the following.

- **Two different photoionised phases and a collisional one are needed to model the 0.5-3.0 keV spectra of NGC 4507.** We showed that the soft X-ray emitting gas has not varied during the monitoring. This suggests that the absorbing material, responsible for the column density variation between June and December 2010, might be much closer to the X-ray source than the circumnuclear matter responsible for the soft emission. As already discussed in Bianchi et al. (2006) and Bianchi & Guainazzi (2007) this gas is likely coincident with the NLR.
- **No column density variations occurred in the 1.5 months XMM-Newton monitoring.** No significant variation with respect to the best fit value for the whole data set ( $9.0 \pm 0.5 \times 10^{23} \text{ cm}^{-2}$ ) has been found. This result brings further evidence to the argument that absorption variability on short time scales (hours-days) can be ruled out in our analysis of this source. If the intervening absorbing material had varied on such short time scales we would not have measured a constant column density in a 1.5 months monitoring. The measured values would have been completely scattered over the range of values observed in the past ( $4 - 9 \times 10^{23} \text{ cm}^{-2}$ ).
- **A column density variation of  $|\Delta N_{\text{H}}| = 2.5 \times 10^{23} \text{ cm}^{-2}$  at a  $3\sigma$  confidence level on a time interval between 1.5 and 4 months has been measured.** Such time scales lead to distances of the absorber ranging from  $R = (7 - 40) M_{7.65} R_{10}^{-2} \text{ pc}$  with corresponding velocities of  $70 - 170 \text{ km/s } M_{7.65}$ . These distances imply that the obscuring material is located well outside the BLR:

- 
- to be consistent with the BLR location the obscuring cloud should have a much bigger linear size, not consistent with the typical BLR ones.
- **The spatial scale of the obscuring material is consistent with the distance of the reflector observed in NGC 4945.** Since the presence of a Compton-thick material around the nucleus is invariably accompanied by a neutral Iron narrow  $K\alpha$ -emission line and a cold reflection emission it is interesting to point out the fact that the spatial scale of the obscuring material in NGC 4507 is consistent with the distance of the reflector observed with *Chandra* in NGC 4945.
  - **Our analysis provides further evidence that a simple, universal circum-nuclear structure of absorbing matter is therefore not able to take into account all the observed phenomenology on absorption variability in AGN.** The column density variation we measured is a further piece that can be added to the puzzle. In our analysis the lack of any variation on short time scales (hours, days) excludes an absorber located in the BLR while the change on time scales of months leads to an absorber much farther from the X-ray source, differently with respect to other variable objects such as NGC 1365, NGC 4151, UGC 4203 on long time scales (months, years) and rapidly changing on short ones observed so far. While it is true that absorption must occur on different scales, not all objects present evidence of absorption from all possible scales.

In conclusion, we addressed two different, complementary, approaches to study the circumnuclear medium of AGN: a statistical analysis of a small sample of both Compton Thin and Compton Thick Seyfert 2 galaxies and via a detailed X-ray spectral investigation of two among the brightest Seyfert 2 galaxies known. The observational evidence discussed in this thesis leads to a geometry of the absorbing material much more complex than the one postulated by the Unification Model. A uniform, single absorbing medium is likely not enough to explain all the observational features of a AGN and hence multiple absorbers should be present around the central source, possibly distributed on different physical scales.



# Chapter 5

## Future perspectives

In the following, we will briefly outline the main topics that will be investigated in the near future, with both longer observations performed with Chandra and with new generation X-ray satellites.

### Longer Chandra observations

The innovative imaging and spectral analysis presented in this thesis opens a new window in observing the circumnuclear medium of nearby Seyfert 2 galaxies. In Fig. 5.1 and Fig 5.2 we present very preliminary studies on the Compton Thick AGN in the Circinus galaxy, using the same approach described in the case of NGC 4945, with a 250 ks Chandra ACIS-S observation. The source presents an extended emission in the 6.2-6.7 keV and in the 2-10 keV energy bands (Fig. 5.1, bottom panels), the two regions are very different from each other and in the top panel of Fig. 5.1 the ratio between the former and the latter is shown. This image emphasizes the region of the Iron  $K\alpha$  emission with respect to the one of the reflected continuum emission: the gas responsible for such a spectral component is clumpy and symmetric with respect to the nucleus, leading to a scenario where the geometry is the fundamental ingredient in the Iron  $K\alpha$  emission. The spectra obtained from the central 4 boxes (Fig 5.2, top panel) and from the lateral 4 boxes (Fig 5.2, bottom panel) allow us to perform a complete mapping of the emitting region and show a variation in EW of the Iron  $K\alpha$  line that can reach a factor of 3. The simple model used to fit the data consists in a reflection continuum (PEXRAV, Madgziarz & Zdziarski 1995) and two Gaussian emission lines for neutral and ionized iron. We are currently investigating if such a variation may be due to different scattering angles between the reflected emission and the line of sight.

NGC 4945 is one of the few AGNs with a neutral Iron emission extended well outside the central nucleus and a clear evidence of a clumpy inhomogeneous

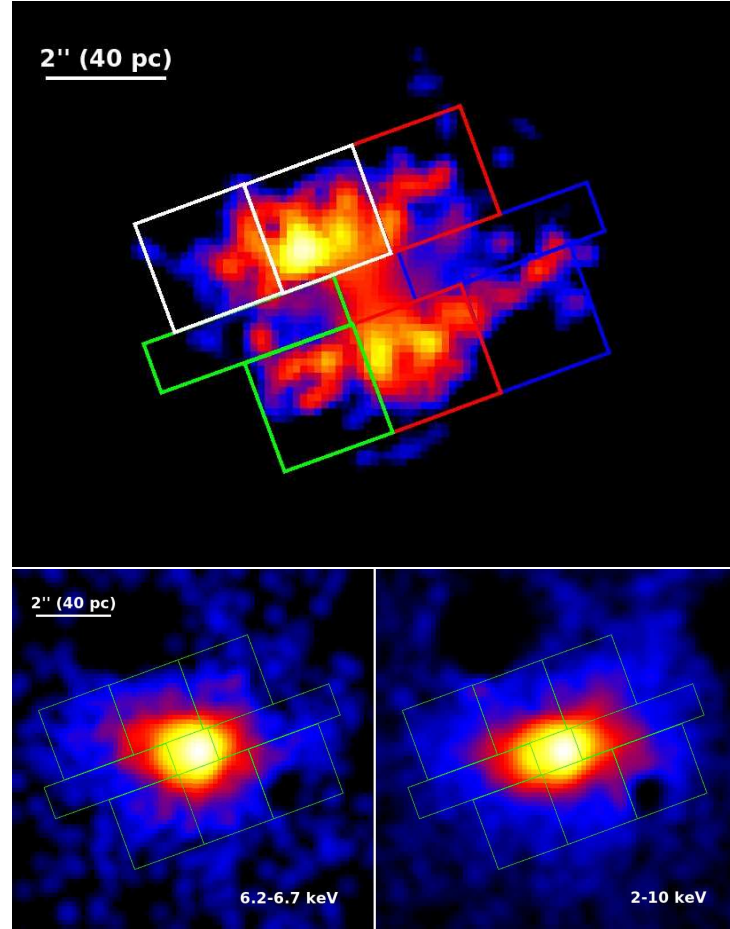


**Figure 5.1:** Images in the 6.2-6.7 keV and 2-10 keV energy bands are shown in the bottom panel. Ratio between the images in the 6.2-6.7 keV and the 2-10 keV energy bands (top panel): the emitting region is clumpy and symmetric with respect to the nuclear region.

structure of the reflector/absorber. Its small distance makes it the best target to investigate these inhomogeneities at the smallest possible spatial scales (by comparison, NGC 1068, with an even higher flux, is at a distance  $\sim 5$  times larger, not allowing a spatially resolved analysis of regions smaller than  $\sim 100$  pc). Our group has successfully applied for 200 ks of observing time of this source during the fourteenth year of activity of *Chandra*.

We tried to investigate the spectral differences within the extended region shown in Fig. 5.3, through a spectral analysis of three regions. The spectra obtained from the three boxes are shown in Fig. 5.4. The visual impression is supported by the spectral analysis, but the variations are barely significant. With the granted

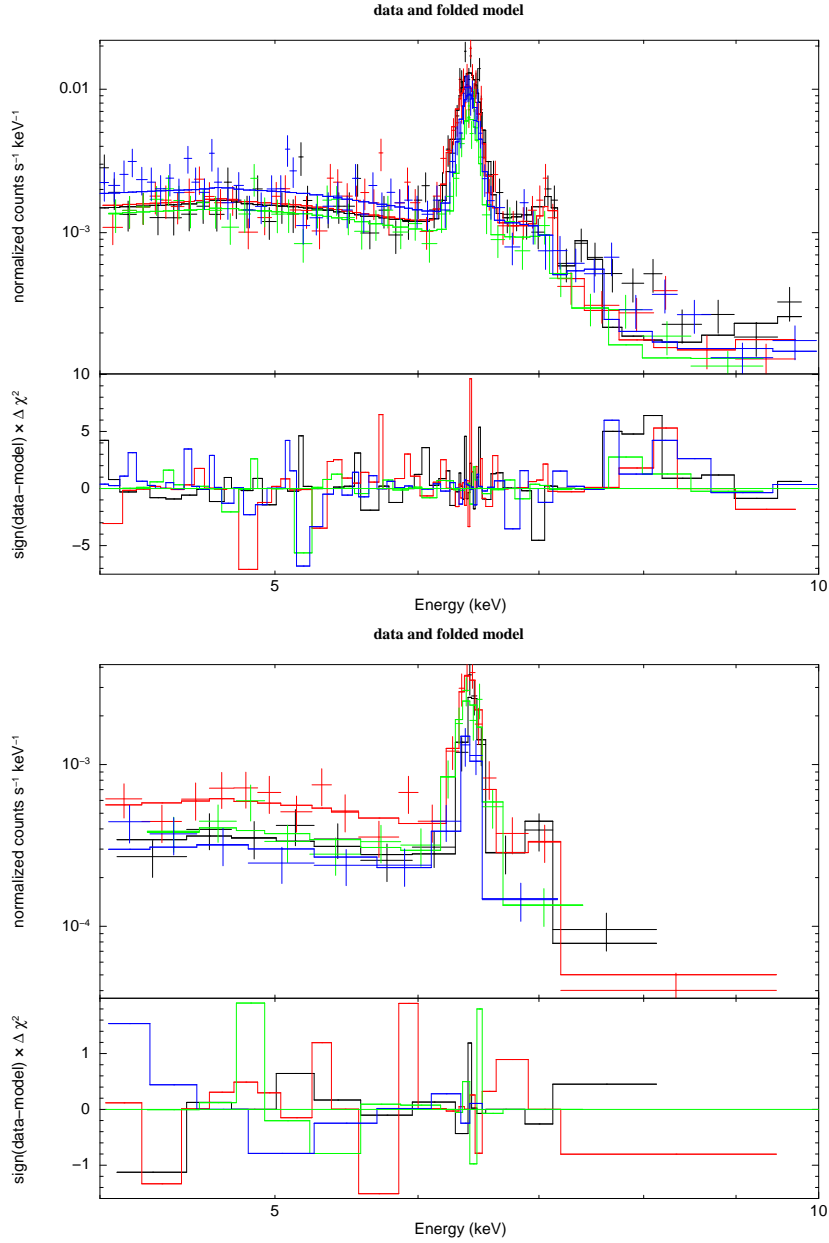


**Figure 5.2:** Top panel: best fits of the 4 spectra obtained from the central regions. Bottom panel: best fits of the 4 spectra obtained from the lateral regions. Colors match the ones in Fig. 5.1.

200ks ACIS-S observation we will have  $\sim 3$  times more counts at the line energy, enough to:

- confirm and better characterize (at a  $\sim 5\sigma$  level) the tentative detections of

variations in the extraction regions;

- firmly establish (at a  $> 3\sigma$  level) possible differences in continuum flux, line energy and line flux, among every  $\sim 0.8''$  (15 pc) region.

Such measurements may become a cornerstone in the X-ray study of the circum-nuclear material in AGN and in particular will be the first spatially resolved spectroscopy of the torus.

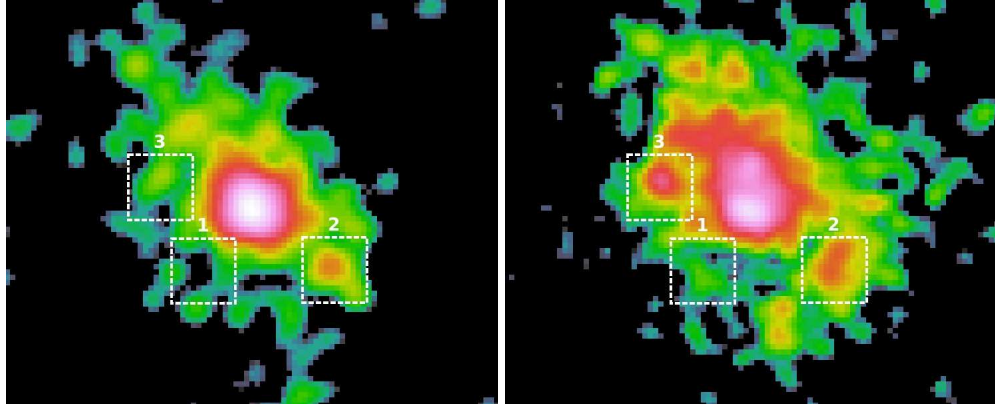


**Figure 5.3:** *Chandra* images of the central region in the Iron  $K\alpha$  band (6.2-6.7 keV, left) and in the hard X-ray band (right), from Marinucci et al. 2012.

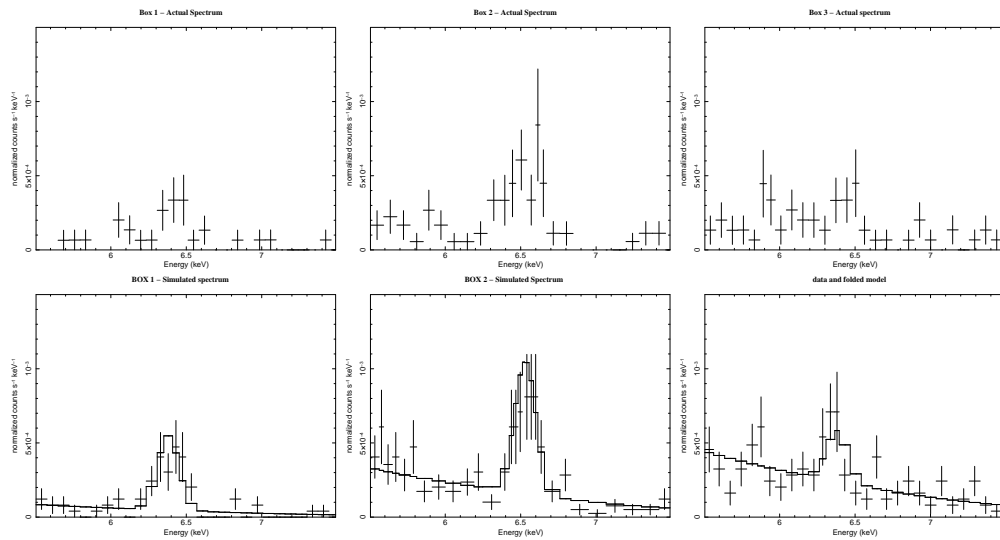


**Figure 5.4:** Spectra from the three boxes shown in Fig. 5.3, obtained with the currently available (top panel) and simulated *Chandra* data (bottom panel).

## New observing opportunities

In the near future, using emission and absorption features produced by the circumnuclear medium of AGN, we will be able to measure the sizes and velocity structures of the emitting regions. A narrow component of the iron  $K\alpha$  line is almost invariably present in the X-ray spectra of AGN. As already seen throughout this thesis, this line originates from reflection of the primary component by the circumnuclear gas; hence it is a powerful tool to establish the location of this gas (either the Broad Line Region, a parsec-scale torus, or the Narrow Line Region), depending on the line width. In current observations the line is typically unresolved, with FWHM upper limits of the order of magnitude of thousands of km/s, compatible with any of the possible locations. The unprecedented spectral resolution of future X-ray missions, together with the large effective area, will allow us to easily measure the FWHM and any bulk velocity flows using the neutral iron  $K\alpha$  line in tens of sources (Fig. 5.5). Reverberation mapping of these lines will reveal their physical location and, combined with line profiles and shifts, can be used to determine the large-scale flows responsible for fueling of SMBHs in the centre of galaxies.

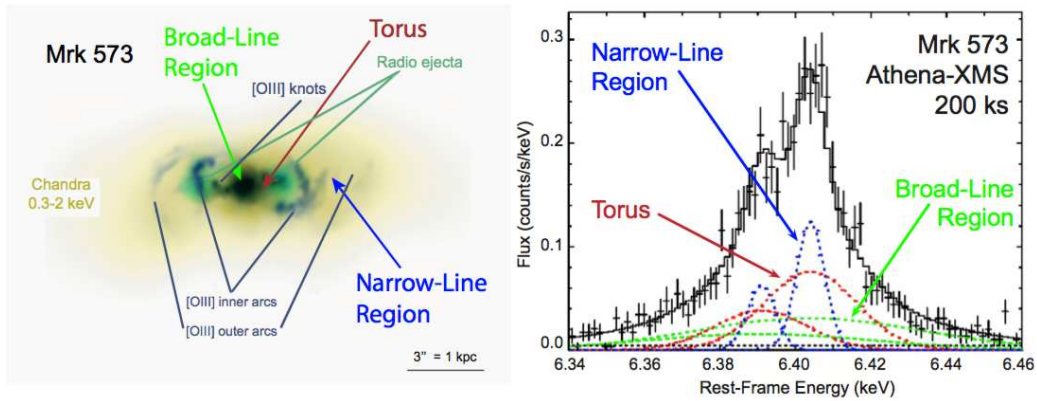


**Figure 5.5:** The Seyfert 2 Mrk 573. Left: multi-wavelength image combining soft X-ray (Chandra: yellow), radio 6 cm (VLA: green), and [O III] emission (HST: dark blue). The approximate locations of the main line-emitting regions are shown (some of them are not actually resolved in this image). Right: Simulated 200 ks Athena-XMS observation of the neutral iron  $K\alpha$  line (actually a doublet) arising from material at different distances from the black hole. The three components can be easily deconvolved if present in a total profile.



A Small Explorer (SMEX) X-ray mission was launched on June 13, 2012 this year. The Nuclear Spectroscopic Telescope Array (NuSTAR) is a NASA mission that carries the first focusing hard X-ray (3-80 keV) telescope in orbit. NuSTAR will offer a factor 50-100 sensitivity improvement compared to previous collimated or coded mask imagers that have operated in this energy band. In addition, NuSTAR provides sub-arcminute imaging with good spectral resolution over a 12-arcminute field of view. Due to its unprecedented high effective area in hard X-rays (see Fig. 5.8 for a comparison with other present X-ray satellites) it is the perfect instrument to observe NGC 4945 in the high energy band, trying to investigate its variability even better. Due to its large energy interval it would be possible to simultaneously observe variations in the hard X-rays (10-80 keV)

### Obscured AGN

Target	R.A.	Dec.	ExpTime	ObsDate
NGC 1365	53.40166667	-36.14027778	3x120 ks	2012 Jul+
NGC 1068	40.66958334	-0.013333333	2x150 ks	2012 Dec+
NGC 4945	196.36458333	-49.46833333	3x50 ks	TBD
Circinus	213.29166667	-65.33916667	2x60 ks	TBD
WISE 1814+3412	151.85875000	12.81555555	21 ks	2012 Oct
WISE 2207+1939	331.93262501	19.66086111	21 ks	2012 Oct
WISE 2238+2653	354.54250000	26.88891667	20 ks	TBD
WISE 2357+0328	359.29500000	3.46761111	20 ks	TBD
PG 1004+130	151.85875000	12.81555555	62 ks	2012 Oct
PG 1700+518	255.35333333	51.82222222	86 ks	2012 Sep
Mrk 231	194.05916667	56.87361111	46 ks	2012 Aug
Arp 220	233.73791666	23.50305556	2x33 ks	TBD
Mrk 273	206.17541666	55.88694444	2x33 ks	TBD
IRAS 05189-2524	80.25583333	-25.36250000	33 ks	TBD
Super Antennae	292.83916667	-72.65500000	2x33 ks	TBD
IRAS 08572+3915	135.10583333	39.06500000	20 ks	TBD
IRAS 09022-3615	136.05291667	-36.45027778	20 ks	TBD
IRAS 10565+2448	164.82541667	24.54277778	20 ks	TBD
IRAS 13120-5453	198.77625000	-55.15638889	20 ks	TBD
IRAS 14378-3651	220.24583333	-37.07555556	20 ks	TBD
IC 2560	154.08041666	-33.56472222	50 ks	TBD
SDSS 0815+4304	123.78083333	43.07416667	20 ks	TBD
SDSS 1157+6003	179.32666667	60.06277778	20 ks	2012 Oct
[NGC 7582]	349.597870	-42.370583	15 ks	2012 Sep

**Figure 5.6:** Long term NuSTAR observing schedule of obscured AGN, from [www.srl.caltech.edu](http://www.srl.caltech.edu).

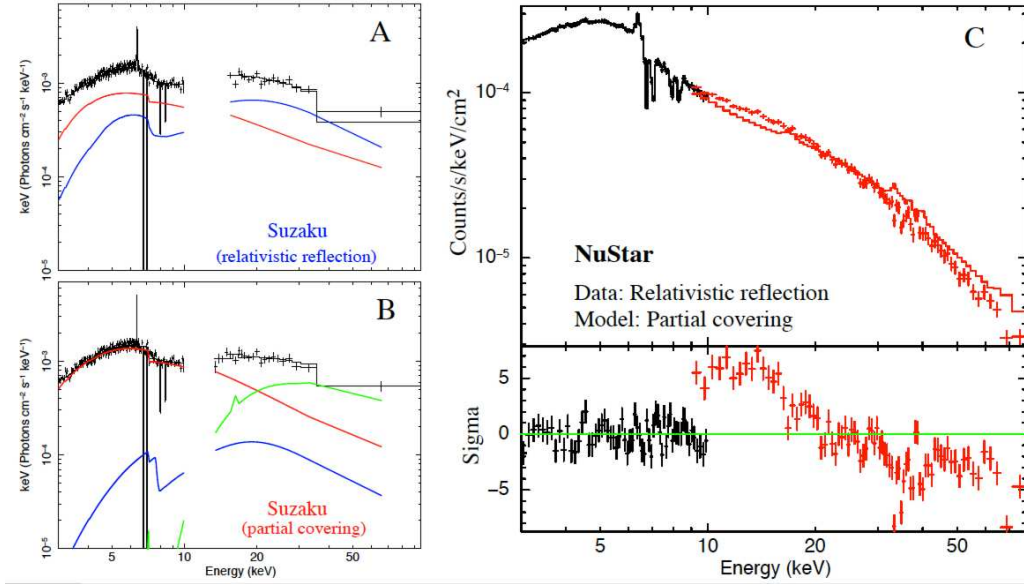


**Figure 5.7:** Left panels: spectra obtained from a  $\sim 150$  ks Suzaku observation of NGC 1365, with two different, equally satisfactory best fit models: one with a strong, relativistically blurred reflection, dominant at energies above 10 keV (panel A, blue line), and one with a partial covering with  $N_H \sim 2 \times 10^{24} \text{ cm}^{-2}$  (panel B, green line). In both cases the intrinsic continuum is shown as a red line. Right panel: Simulation of a simultaneous 100 ks XMM-Newton+NuSTAR spectrum of NGC 1365 assuming the relativistically blurred model, and then compared with the partial covering model. Lower panel: residuals in units of  $\sigma$ .

and a possible response from the circumnuclear material (5-10 keV). Very accurate measurements of the absorbing column density will be possible both in NGC 4945 and NGC 4507, searching for possible variations with respect to the values observed so far. In Fig. 5.6 the long term observing schedule of the Obscured AGN sample is shown and several sources discussed in this thesis, such as NGC 1365, NGC 4945 and the Circinus galaxy are included. In the particular case of NGC 1365 the simultaneous XMM-Newton+NuSTAR observational campaign will be fundamental to discriminate between the two different, equally satisfactory, physical scenarios proposed so far: one with a strong, relativistically blurred reflection, dominant at energies above 10 keV (Fig. 5.7 panel A, blue line), and one with a partial covering with  $N_H \sim 2 \times 10^{24} \text{ cm}^{-2}$  (Fig. 5.7 panel B, green line). With the expected launch of ASTRO-H in 2014 a new era for X-ray astronomy will begin. Among all other instruments, it will take onboard the Soft X-ray Spectrometer (SXS), thanks to its microcalorimeter an unprecedented energy resolution in the energy range between 0.5 and 12 keV will be reached. Thanks to its effec-

tive area of  $210 \text{ cm}^2$  at 6 keV (see Fig. 5.8) and its energy resolution of  $\sim 5 \text{ eV}$  at 6 keV we will be able to fully resolve Iron  $K\alpha$  emission features in the two Seyfert 2s analyzed in this thesis, constraining the distance where the line is emitted and therefore investigating the dynamics of the material responsible for its production.

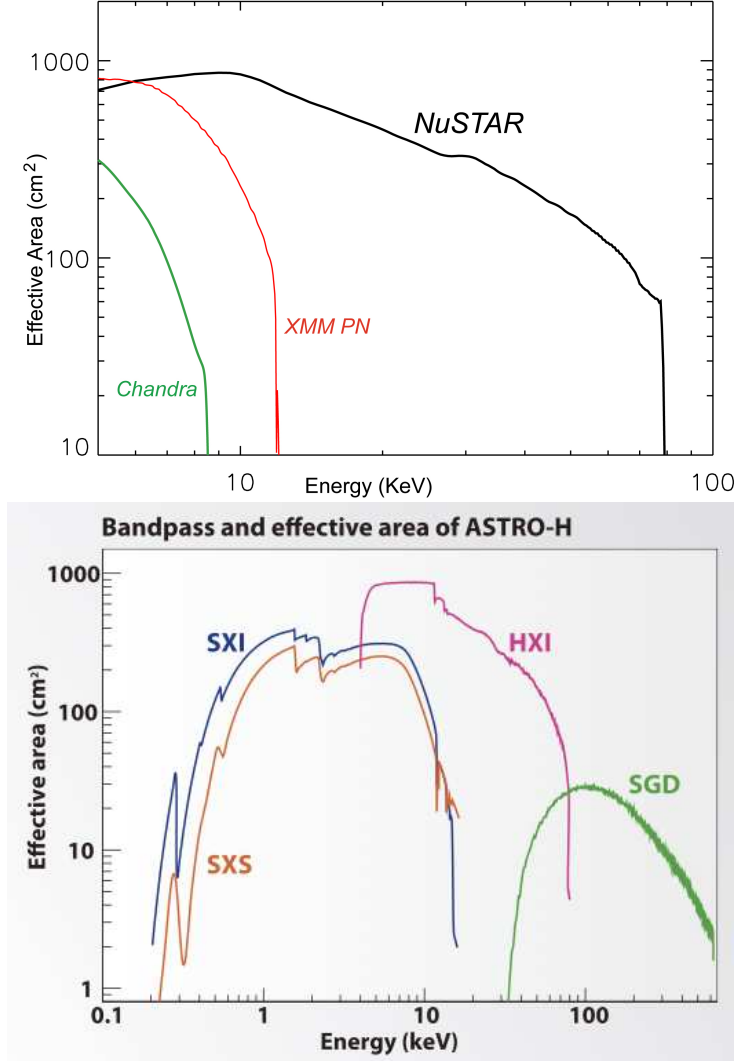


**Figure 5.8:** Effective area of NuSTAR and ASTRO-H X-ray missions, in comparison with present X-ray satellites.

# Appendix A

## X-ray Satellites

### A.1 XMM-Newton

The X-ray Multi-Mirror satellite is the second ‘Cornerstone’ mission of the European Space Agency. Renamed XMM-Newton, it was launched with an Ariane 5 spacecraft from Kourou, French Guyana, on 10 December 1999, and put into an highly elliptical orbit, with an apogee of about 114 000 km and a perigee of about 7000 km. This choice for the orbit allows for long, continuous exposures unaffected by Earth blockage and avoids degradation to the CCD cameras, since the spacecraft does not pass through the Earth’s proton belt. However, XMM-Newton is known to be affected by particle induced background, which can be very high in some orbital phases, depending upon many factors, such as the altitude of the satellite, its position with respect to the magnetosphere, and the amount of solar activity.

The satellite consists of three X-ray telescopes, each composed by 58 Wolter I grazing-incidence mirrors which are nested in a coaxial and cofocal configuration:

1. **European Photo Imaging Cameras (EPIC):** These cameras are CCDs of two different types: two MOS and a pn (see table A.1). They work approximately in the same band (0.1-15 keV), but differ for the geometry arrays, the readout times and the quantum efficiencies. They are installed behind the X-ray telescopes that are equipped with the gratings of the Reflection Grating Spectrometers (RGS). The gratings divert about half of the telescope incident flux towards the RGS detectors such that (taking structural obscuration into account) about 44% of the original incoming flux reaches the MOS cameras. The third X-ray telescope has an unobstructed beam; the EPIC instrument at the focus of this telescope uses pn CCDs and is referred to as the pn camera.

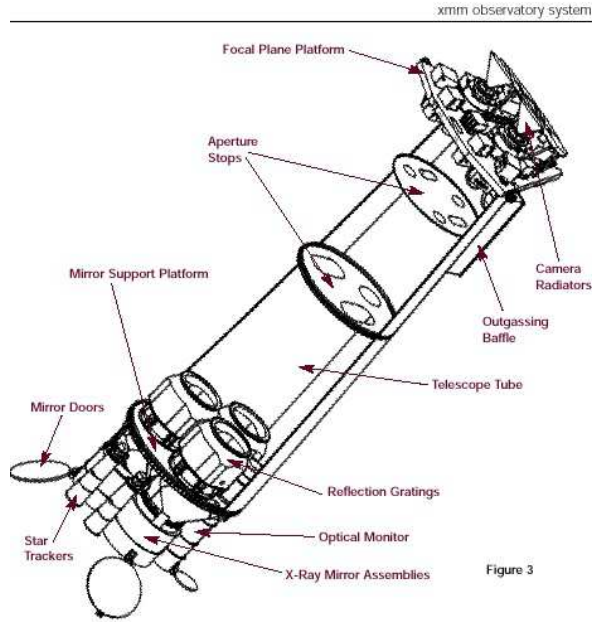


**Figure A.1:** The XMM-Newton observatory

2. **Reflection Grating Spectrometer (RGS):** behind two of the three telescopes, about half of the X-ray light is utilized by the Reflection Grating Spectrometers (RGS). Each RGS consists of an array of reflection gratings which diffracts the X-rays to an array of dedicated charge coupled devices (CCD) detectors. The RGS instruments achieve high resolving power (150 to 800) over a range from 5 to 35 Å [0.33 to 2.5 keV] (in the first spectral order). The effective area peaks around 15 Å [0.83 keV] (first order) at about 150 cm<sup>2</sup> for the two spectrometers.
3. **Optical Monitor (OM):** the XMM-OM is mounted on the mirror support platform of XMM-Newton alongside the X-ray mirror modules. It provides coverage between 170 nm and 650 nm of the central 17 arc minute square region of the X-ray field of view, permitting routine multiwavelength observations of XMM targets simultaneously in the X-ray and ultraviolet/optical bands.

## A.2 Chandra

The Advanced X-ray Astrophysics Facility (AXAF) is a major NASA mission (Fig. A.2). It was launched by the Space Shuttle Columbia on July 23, 1999, and

## A.2. *Chandra*

Instrument	Main Purpose	Energy Range/ Bandwidth	Spectral Resolution ( $E/\Delta E$ )	Spatial Resolution (arcsec)	Sensitivity	Total Mass/Power
EPIC	High-throughput non-dispersive imaging/ spectroscopy	0.1 - 15 keV 1 - 120 Å	5 - 60	14 (Half Energy Width)	$10^{-14}$ erg/cm <sup>2</sup> sec	235 kg 240 W
OM	Optical/UV imaging	160 - 600 nm	50 - 100 (with grisms)	1	< 24 magnitude	82 kg 60 W
RGS	High-resolution dispersive spectroscopy	0.35 - 2.5 keV 5 - 35 Å	200 - 800 (400/800 at 15 Å in 1st/2nd order)	N.A.	$3 \times 10^{-13}$ erg / cm <sup>2</sup> s	248 kg 140 W

**Table A.1:** Characteristics of the instruments onboard XMM-*Newton* (from Bagdasarian et al. 1999).

renamed ‘Chandra’ after the Indian-American Nobel physicist, Subrahmanyan Chandrasekhar. The highly elliptical orbit has a perigee at 16,000 kilometers from Earth and lasts 64 hours and 18 minutes. This choice lets the spacecraft spend 85% of its orbit above the belts of charged particles, allowing uninterrupted observations as long as 55 hours. The mirror consists of four pairs of nested reflecting surfaces, arranged in the usual Wolter type 1 geometry but with an unprecedented resolution of 0.5 arcseconds.

The complete *Chandra* suite of science instruments therefore comprises two imaging/readout devices (HRC and ACIS) on two different focal planes and two gratings (LETG and HETG), the produced spectra are dispersed in space at the focal plane, using either the ACIS array or the HRC to record data (Table A.2):

1. the **High Resolution Camera (HRC)**, best used for high resolution imaging, has an unprecedented resolution of 0.5 arcseconds, equivalent to the ability of reading a newspaper at a distance of 1.5 km. The primary components of the (HRC) are two Micro-Channel Plates (MCP). They each consist of a 10-cm square cluster of 69 million tiny lead-oxide glass tubes that are about 10  $\mu\text{m}$  in diameter and 1.2 mm long. The camera is shielded from UV photons and the tubes have a special coating that causes electrons to be released when the tubes are struck only by X-rays;
2. the **Advanced CCD Imaging Spectrometer (ACIS)** offers the capability to simultaneously acquire high-resolution images and moderate resolution spectra. ACIS contains 10 planar,  $1024 \times 1024$  pixel CCDs: four arranged in a  $2 \times 2$  array (ACIS-I) used for imaging, and six arranged in a  $1 \times 6$  array (ACIS-S) used either for imaging or as a grating readout.
3. two transmission grating spectrometers, formed by sets of gold gratings



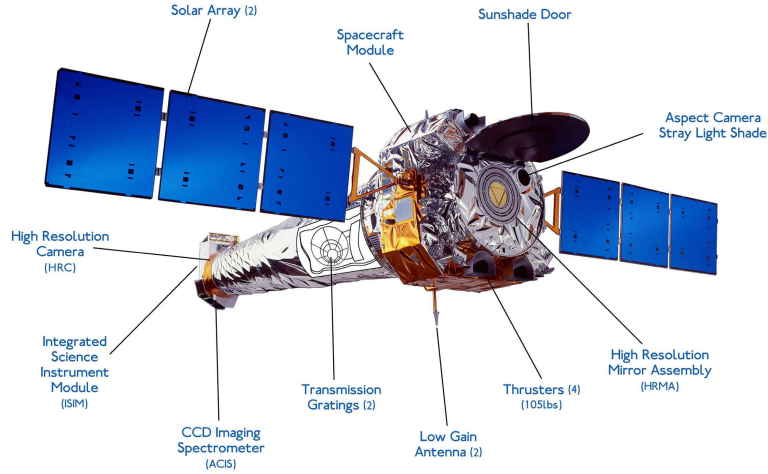


**Figure A.2:** The *Chandra* X-ray observatory (from CXC/NGST).

<b>HETGS range</b>	0.4 - 10.0 keV (31 - 1.2 )
High Energy Grating (HEG) range	0.8 - 10.0 keV (15 - 1.2 )
Medium Energy Grating (MEG) range	0.4 - 5.0 keV (31 - 2.5 )
<b>Effective area (MEG+HEG first orders, with ACIS-S)</b>	
@ 0.5 keV	7 cm <sup>2</sup>
@ 1.0 keV	59 cm <sup>2</sup>
@ 1.5 keV	200 cm <sup>2</sup>
@ 6.5 keV	28 cm <sup>2</sup>
<b>Resolving power (<math>\frac{E}{\Delta E}</math>)</b>	
HEG	65 - 1070 (1000 @ 1 keV, 12.4 )
MEG	80 - 970 (660 @ 0.826 keV, 15 )
<b>Resolution</b>	
$\Delta\lambda$ , HEG	0.012 FWHM
$\Delta\lambda$ , MEG	0.023 FWHM
<b>Absolute wavelength accuracy</b>	
HEG	$\pm 0.006$
MEG	$\pm 0.011$
<b>Wavelength scale</b>	
HEG	0.0055595 / ACIS pixel
MEG	0.0111185 / ACIS pixel

**Table A.2:** Characteristics of *Chandra* HETG.

facets mounted on an assembly can be placed just behind the mirrors. They are best used for high resolution spectroscopy: one set is optimized for low energies (**Low Energy Transmission Gratings: LETG**) and the other for high energies (**High Energy Transmission Gratings: HETG**). The lat-

ter is constituted by the high-energy gratings (HEG: 0.8 - 10.0 keV), and the medium-energy gratings (MEG: 0.4 - 5.0 keV), with spectral resolving powers ( $E/\Delta E$ ) up to 1000. The produced spectra are dispersed in space at the focal plane, using either the ACIS array or the HRC to record data.

## A.3 Suzaku

Suzaku, formerly Astro-E2, was developed at the Institute of Space and Astronautical Science of Japan Aerospace Exploration Agency (ISAS/JAXA), Japan, in collaboration with U.S. (NASA/GSFC, MIT) and Japanese institutions, and launched on 2005 July 10. Suzaku is the recovery mission for ASTRO-E, which did not achieve orbit during launch in February 2000.

Suzaku (Fig. A.3) covers the energy range 0.2 - 700 keV with the three instruments: an X-ray micro-calorimeter (X-ray Spectrometer, or XRS), four X-ray CCDs (the X-ray Imaging Spectrometers, or XISs), and a hard X-ray detector, or HXD (Table A.3). The XRS is a non-dispersive (thus, high-efficiency) imaging (30-element) spectrometer (about 6.5 eV FWHM). It is cryogenically cooled by an adiabatic diamagnetic refrigerator within a helium dewar. The detector array sits behind a conical foil mirror (X-ray Telescope, or XRT) assembly, with spatial resolution of about 1.8' half power diameter (HPD). The effective area of this

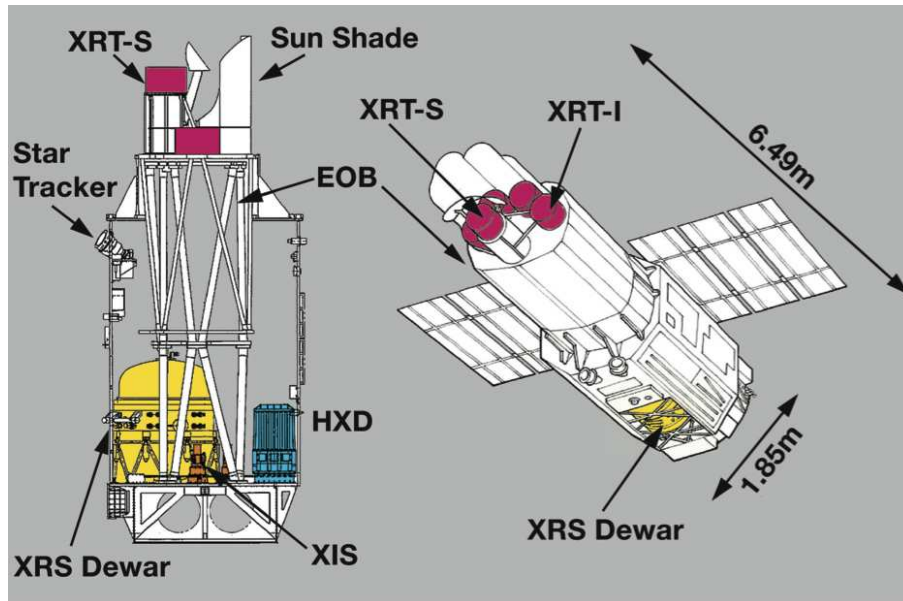


**Figure A.3:** The Suzaku X-ray satellite (from NASA/GSFC ).



	XRS	XIS	HXD
<b>Energy Range</b>	0.3-12 keV	0.2-12 keV	10 - 600 keV
<b>Number of Sensors</b>	1	4 (one CCD chip/sensor)	1 (16 identical units)
<b>Number of Pixels</b>	30 pixels (6x6 geometry)	1024 x 1024 for each CCD	-
<b>Pixel Size</b>	625 micron x 625 micron	24 micron x 24 micron	-
<b>Effective area per sensor</b>	100 cm <sup>2</sup> @1 keV	400 cm <sup>2</sup> @1.5 keV	160 cm <sup>2</sup> @15 keV
	150 cm <sup>2</sup> @6 keV	250 cm <sup>2</sup> @6 keV	300 cm <sup>2</sup> @120 keV
<b>Energy Resolution (FWHM)</b>	6.5 eV	120 eV @6keV	3 keV (10-30 keV)
		50 eV @1 keV	9% (at 662 keV)
<b>Field of View</b>	2.9'x2.9'	19'x19'	0.56 deg x 0.56 deg (E<100 keV)
			4.6 deg x 4.6 deg (E>200 keV)
<b>Imaging Capability</b>	Limited by the pixel size	Full	None (collimated)
<b>Spatial Resolution</b>	~1.8' (HPD of XRT PSF)		-
<b>Others</b>	~2.5 yr lifetime	-	also observe gamma-ray bursts

**Table A.3:** Characteristics of the instruments onboard Suzaku (from NASA/GSFC).

system at 6 keV is about 150 cm<sup>2</sup>. However, XRS prematurely lost all its liquid helium cryogen and is no longer operative. Suzaku is complementary to Chandra and XMM-Newton observatories due to its large collecting area and very large simultaneous bandwidth. Suzaku has two major instruments. These are:

1. Four units of **X-ray Imaging Spectrometer (XIS)**. Each XIS consists of four X-ray CCD cameras, each combined with a single X-ray Telescope (XRT). Each CCD camera has a single CCD chip with 1024 × 1024 pixels, and covers a 18 arcmin×18 arcmin region on the sky. Each pixel is a 24 micron square, and the size of the CCD chip is 25 mm×25 mm. One unit of XIS is equipped with a back-side illuminated CCD chip, while the rest contain a front-side illuminated CCD each.
2. The **Hard X-ray Detector (HXD)** is a non-imaging instrument provided by a Japanese consortium led by the University of Tokyo and ISAS/JAXA. It is a hard X-ray (of order 10-600 keV) collimated system of "well" detectors, namely the GSO (> 50 keV) and the silicon PIN diodes (< 50 keV). The HXD is characterized by the low background of  $\sim 10^{-5}$  cts/s/cm<sup>2</sup>/keV; its sensitivity is higher than any past missions in the energy range from a few tens keV to several hundreds keV. The anti-counters, whose main purpose is to reject particle background, are also expected to detect transient high energy phenomena such as the gamma-ray bursts.

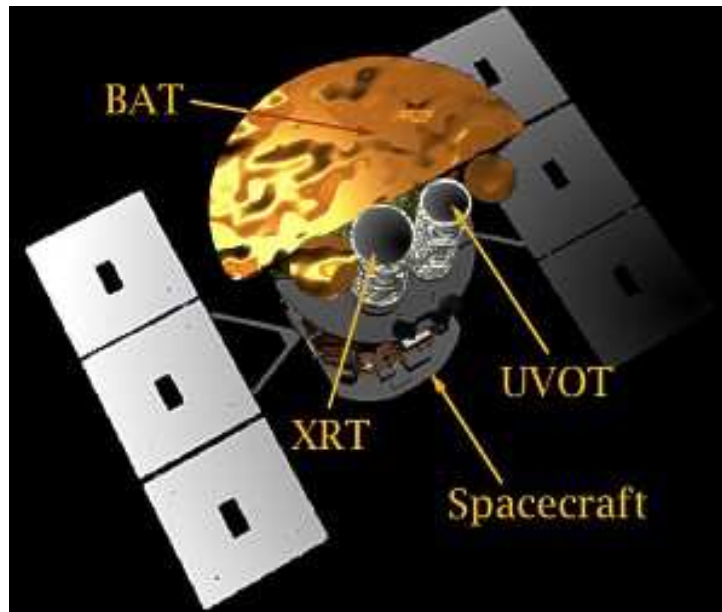


**Figure A.4:** The Swift X-ray satellite (from NASA/GSFC ).

## A.4 Swift

Swift is a NASA medium sized explorer mission, developed in collaboration with UK and Italy (Fig. A.4). It was successfully launched on November 20, 2004 from Cape Canaveral (USA). The primary scientific objectives are to determine the origin of Gamma Ray Bursts (GRB) and to pioneer their use as probes of the early universe. Swift is a multiwavelength observatory carrying three instruments: the Burst Alert Telescope working in the 15-150 keV energy range, the X-ray Telescope between 0.2 and 10 keV and the Ultraviolet/Optical Telescope (170-650 nm):

1. the Burst Alert Telescope (BAT) covers a large fraction of the sky (over one steradian fully coded, three steradians partially coded). It locates the position of each event with an accuracy of 1 to 4 arc-minutes within 15 seconds. This crude position is immediately relayed to the ground, and some wide-field, rapid-slew ground-based telescopes can catch the GRB with this information. The BAT uses a coded-aperture mask of 52,000 randomly placed 5 mm lead tiles, 1 meter above a detector plane of 32,768 four mm CdZnTe hard X-ray detector tiles;
2. the X-ray Telescope (XRT) provides more precise location of the GRB, with a typical error circle of approximately 2 arcseconds radius. The XRT is also

used to perform long-term monitoring of GRB afterglow light-curves for days to weeks after the event, depending on the brightness of the afterglow. The XRT uses a Wolter Type I X-ray telescope with 12 nested mirrors, focused onto a single MOS charge-coupled device (CCD) similar to those used by the XMM-Newton EPIC MOS cameras. On-board software allows fully automated observations, with the instrument selecting an appropriate observing mode for each object, based on its measured count rate;

3. the Ultraviolet/Optical Telescope (UVOT) is used to detect an optical afterglow. The UVOT provides a sub-arcsecond position and provides optical and ultra-violet photometry through lenticular filters and low resolution spectra through the use of its optical and UV grisms. The UVOT is also used to provide long-term follow-ups of GRB afterglow light curves. The UVOT is based on the XMM-Newton mission's Optical Monitor (OM) instrument, with improved optics and upgraded onboard processing computers.

# Acknowledgements

First of all I would like to thank all the people who helped me during these three years to make this thesis possible. In particular Giorgio Matt, for his constant support throughout this work and Stefano Bianchi, for his advices and patience. I am grateful to my supervisors at the Cfa: Guido Risaliti, who showed me how to use the fundamental tools to perform the analysis in this thesis and Martin Elvis, for his precious comments and suggestions. I would finally like to thank Massimo Cappi for his useful comments and all the people I had the chance to collaborate with during the preparation of this thesis: Fabrizio Nicastro, Pepi Fabbiano, Junfeng Wang, and Emanuele Nardini.



# References for this thesis

## Chapter 2

**Marinucci A.<sup>1</sup>, Bianchi S.<sup>1</sup>, Nicastro F.<sup>2</sup>, Matt G.<sup>1</sup>, Goulding A. C.<sup>3</sup>**, “*The link between the HBLR and the accretion rate in Sy2 galaxies*”, 2012, ApJ, 748, 130M

## Chapter 3

**Marinucci A.<sup>1</sup>, Risaliti G.<sup>3,4</sup>, Wang J.<sup>3</sup>, Bianchi S.<sup>1</sup>, Elvis M.<sup>3</sup>, Matt G.<sup>1</sup>, Nardini E.<sup>3</sup>**, “*X-ray absorption variability in NGC 4507*”, arXiv:1212.4151

**Marinucci A.<sup>1</sup>, Risaliti G.<sup>3,4</sup>, Wang J.<sup>3</sup>, Nardini E.<sup>3</sup>, Elvis M.<sup>3</sup>, Fabbiano G.<sup>3</sup>, Bianchi S.<sup>1</sup>, Matt G.<sup>1</sup>**, “*The X-ray reflector in NGC 4945: a time- and space-resolved portrait*”, 2012, MNRAS, 423, L6

1. Dipartimento di Fisica, Università degli Studi “Roma Tre”, Via della Vasca Navale 84, I-00146 Roma, Italy
2. INAF - Osservatorio Astronomico di Roma, via Frascati 33, Monteporzio (Rm) I00040 Italy
3. Harvard-Smithsonian Center for Astrophysics, 60 Garden st., Cambridge, MA 02138, USA
4. INAF - Osservatorio Astrofisico di Arcetri, Largo E. Fermi 5, 50125 Firenze, Italy



# Bibliography

- Abramowicz M. A., Chen X., Kato S., Lasota J., Regev O., 1995, *ApJ*, 438, L37
- Adams T. F., 1977, *ApJS*, 33, 19
- Anders E., Grevesse N., 1989a, *Geochim. Cosmochim. Acta*, 53, 197
- Anders E., Grevesse N., 1989b, *Geochim. Cosmochim. Acta*, 53, 197
- Antonucci R., 1993, *ARA&A*, 31, 473
- Antonucci R. R. J., Miller J. S., 1985, *ApJ*, 297, 621
- Arnaud K. A., 1996, in *ASP Conf. Ser. 101: Astronomical Data Analysis Software and Systems V XSPEC: The First Ten Years*. p. 17
- Awaki H., Kunieda H., Tawara Y., Koyama K., 1991, *PASJ*, 43, L37
- Bagnasco G., Eggel H. G. F., Thürey S., 1999, *ESA Bulletin Number 100* (<http://esapub.esrin.esa.it/bulletin/bullet100/bagna100.htm>)
- Bambynek W., Crasemann B., Fink R. W., Freund H.-U., Mark H., Swift C. D., Price R. E., Rao P. V., 1972, *Reviews of Modern Physics*, 44, 716
- Barbosa F. K. B., Storchi-Bergmann T., Cid Fernandes R., Winge C., Schmitt H., 2009, *MNRAS*, 396, 2
- Barth A. J., Ho L. C., Sargent W. L. W., 2002, *AJ*, 124, 2607
- Bassani L., Dadina M., Maiolino R., Salvati M., Risaliti G., della Ceca R., Matt G., Zamorani G., 1999, *ApJS*, 121, 473
- Baum S. A., Gallimore J. F., O’Dea C. P., Buchanan C. L., Noel-Storr J., Axon D. J., Robinson A., Elitzur M., Dorn M., Staudaher S., 2010, *ApJ*, 710, 289
- Bearden J. A., 1967, *Reviews of Modern Physics*, 39, 78



- Bian W., Gu Q., 2007, *ApJ*, 657, 159
- Bianchi S., Balestra I., Matt G., Guainazzi M., Perola G. C., 2003, *A&A*, 402, 141
- Bianchi S., Chiaberge M., Evans D. A., Guainazzi M., Baldi R. D., Matt G., Piconcelli E., 2010a, *MNRAS*, pp 418–+
- Bianchi S., Chiaberge M., Evans D. A., Guainazzi M., Baldi R. D., Matt G., Piconcelli E., 2010b, *ArXiv e-prints*
- Bianchi S., Chiaberge M., Piconcelli E., Guainazzi M., 2007, *MNRAS*, 374, 697
- Bianchi S., Corral A., Panessa F., Barcons X., Matt G., Bassani L., Carrera F. J., Jiménez-Bailón E., 2008, *MNRAS*, 385, 195
- Bianchi S., Guainazzi M., 2007, in di Salvo T., Israel G. L., Piersant L., Burderi L., Matt G., Tornambe A., Menna M. T., eds, *The Multicolored Landscape of Compact Objects and Their Explosive Origins* Vol. 924 of *American Institute of Physics Conference Series*, The nature of the soft X-ray emission in obscured AGN. pp 822–829
- Bianchi S., Guainazzi M., Chiaberge M., 2006, *A&A*, 448, 499
- Bianchi S., Guainazzi M., Matt G., Fonseca Bonilla N., 2007, *A&A*, 467, L19
- Bianchi S., Guainazzi M., Matt G., Fonseca Bonilla N., Ponti G., 2009, *A&A*, 495, 421
- Bianchi S., Maiolino R., Risaliti G., 2012, *Advances in Astronomy*, 2012
- Bianchi S., Matt G., Balestra I., Guainazzi M., Perola G. C., 2004, *A&A*, 422, 65
- Bianchi S., Matt G., Balestra I., Perola G. C., 2003, *A&A*, 407, L21
- Bianchi S., Miniutti G., Fabian A. C., Iwasawa K., 2005, *MNRAS*, 360, 380
- Bianchi S., Panessa F., Barcons X., Carrera F. J., La Franca F., Matt G., Onori F., Wolter A., Corral A., Monaco L., Ruiz A., Brightman M., 2012, *ArXiv e-prints*
- Bianchi S., Piconcelli E., Chiaberge M., Bailón E. J., Matt G., Fiore F., 2009, *ApJ*, 695, 781
- Blustin A. J., Page M. J., Fuerst S. V., Branduardi-Raymont G., Ashton C. E., 2005, *A&A*, 431, 111

## BIBLIOGRAPHY

---

- Braitto V., Ballo L., Reeves J. N., Ptak A., Risaliti G., Turner T. J., 2012, ArXiv e-prints
- Brightman M., Nandra K., 2008, MNRAS, 390, 1241
- Brinkman A. C., Kaastra J. S., van der Meer R. L. J., Kinkhabwala A., Behar E., Kahn S. M., Paerels F. B. S., Sako M., 2002, A&A, 396, 761
- Cappi M., 2006, Astronomische Nachrichten, 327, 1012
- Cappi M., Tombesi F., Bianchi S., Dadina M., Giustini M., Malaguti G., Maraschi L., Palumbo G. G. C., Petrucci P. O., Ponti G., Vignali C., Yaqoob T., 2009, A&A, 504, 401
- Chartas G., Brandt W. N., Gallagher S. C., 2003, ApJ, 595, 85
- Clavel J., Wamsteker W., Glass I. S., 1989, ApJ, 337, 236
- Comastri A., Vignali C., Cappi M., Matt G., Audano R., Awaki H., Ueno S., 1998, MNRAS, 295, 443
- Crummy J., Fabian A. C., Gallo L., Ross R. R., 2006, MNRAS, 365, 1067
- Czerny B., Róžańska A., Kuraszkiewicz J., 2004, A&A, 428, 39
- Diamond-Stanic A. M., Rieke G. H., Rigby J. R., 2009, ApJ, 698, 623
- Dickey J. M., Lockman F. J., 1990, ARA&A, 28, 215
- Done C., Davis S. W., Jin C., Blaes O., Ward M., 2012, MNRAS, 420, 1848
- Elitzur M., Ho L. C., 2009, ApJ, 701, L91
- Elitzur M., Shlosman I., 2006, ApJ, 648, L101
- Elvis M., 2000, ApJ, 545, 63
- Elvis M., 2012, ArXiv e-prints
- Elvis M., Risaliti G., Nicastro F., Miller J. M., Fiore F., Puccetti S., 2004, ApJ, 615, L25
- Elvis M., Wilkes B. J., McDowell J. C., Green R. F., Bechtold J., Willner S. P., Oey M. S., Polonski E., Cutri R., 1994, ApJS, 95, 1
- Fabian A. C., Iwasawa K., Reynolds C. S., Young A. J., 2000, PASP, 112, 1145

- Fabian A. C., Miniutti G., 2005, ArXiv Astrophysics e-prints
- Fabian A. C., Ross R. R., 2010, *Space Sci. Rev.*, 157, 167
- Ferland G. J., 2000, in *Revista Mexicana de Astronomia y Astrofisica Conference Series Cloudy 94 and Applications to Quasar Emission Line Regions*. pp 153–157
- Ferrarese L., Merritt D., 2000, *ApJ*, 539, L9
- Fruscione A., McDowell J. C., Allen G. E., Brickhouse N. S., Burke D. J., Davis J. E., Durham N., Elvis M., Galle E. C., Harris D. E., Huenemoerder D. P., Houck J. C., Ishibashi B., Karovska M., Nicastro F., Noble M. S., Nowak M. A., Primini F. A., 2006, in *Observatory Operations: Strategies, Processes, and Systems*. Edited by Silva, David R.; Doxsey, Rodger E.. *Proceedings of the SPIE*, Volume 6270, pp. 62701V (2006). Vol. 6270 of *Presented at the Society of Photo-Optical Instrumentation Engineers (SPIE) Conference, CIAO: Chandra's data analysis system*
- Gabriel C., Denby M., Fyfe D. J., Hoar J., Ibarra A., Ojero E., Osborne J., Saxton R. D., Lammers U., Vacanti G., 2004, in F. Ochsenbein, M. G. Allen, & D. Egret ed., *Astronomical Data Analysis Software and Systems (ADASS) XIII* Vol. 314 of *Astronomical Society of the Pacific Conference Series, The XMM-Newton SAS - Distributed Development and Maintenance of a Large Science Analysis System: A Critical Analysis*. pp 759–+
- Gallagher S. C., Brandt W. N., Laor A., Elvis M., Mathur S., Wills B. J., Iyomoto N., 2001, *ApJ*, 546, 795
- Garcia-Rissmann A., Vega L. R., Asari N. V., Cid Fernandes R., Schmitt H., González Delgado R. M., Storchi-Bergmann T., 2005, *MNRAS*, 359, 765
- Garmire G. P., Bautz M. W., Ford P. G., Nousek J. A., Ricker G. R., 2003, in *X-Ray and Gamma-Ray Telescopes and Instruments for Astronomy*. Edited by Joachim E. Truemper, Harvey D. Tananbaum. *Proceedings of the SPIE*, Volume 4851, p. 28-44 *Advanced CCD imaging spectrometer (ACIS) instrument on the Chandra X-ray Observatory*
- George I. M., Fabian A. C., 1991, *MNRAS*, 249, 352
- Ghisellini G., Haardt F., Matt G., 1994, *MNRAS*, 267, 743
- Goulding A. D., Alexander D. M., 2009, *MNRAS*, 398, 1165

## BIBLIOGRAPHY

---

- Goulding A. D., Alexander D. M., Lehmer B. D., Mullaney J. R., 2010, MNRAS, 406, 597
- Granato G. L., Danese L., Franceschini A., 1997, ApJ, 486, 147
- Greene J. E., Ho L. C., 2005, ApJ, 627, 721
- Gu Q., Huang J., 2002, ApJ, 579, 205
- Guainazzi M., 2002, MNRAS, 329, L13
- Guainazzi M., Matt G., Fiore F., Perola G. C., 2002, A&A, 388, 787
- Guilbert P. W., Rees M. J., 1988, MNRAS, 233, 475
- Gültekin K., Richstone D. O., Gebhardt K., Lauer T. R., Tremaine S., Aller M. C., Bender R., Dressler A., Faber S. M., Filippenko A. V., Green R., Ho L. C., Kormendy J., Magorrian J., Pinkney J., Siopis C., 2009, ApJ, 698, 198
- Haardt F., Maraschi L., 1991, ApJ, 380, L51
- Haardt F., Maraschi L., Ghisellini G., 1994, ApJ, 432, L95
- Haas M., Siebenmorgen R., Schulz B., Krügel E., Chini R., 2005, A&A, 442, L39
- Ho L. C., 2008, ARA&A, 46, 475
- Hönig S. F., Kishimoto M., 2010, A&A, 523, A27
- Huchra J., Burg R., 1992, ApJ, 393, 90
- Ichimaru S., 1977, ApJ, 214, 840
- Kewley L. J., Heisler C. A., Dopita M. A., Lumsden S., 2001, ApJS, 132, 37
- Kinkhabwala A., Sako M., Behar E., Kahn S. M., Paerels F., Brinkman A. C., Kaastra J. S., Gu M. F., Liedahl D. A., 2002, ApJ, 575, 732
- Komossa S., 2000, ArXiv Astrophysics e-prints
- Konigl A., Kartje J. F., 1994, ApJ, 434, 446
- Korista K., Baldwin J., Ferland G., Verner D., 1997, ApJS, 108, 401
- Kraemer S. B., Schmitt H. R., Crenshaw D. M., Meléndez M., Turner T. J., Guainazzi M., Mushotzky R. F., 2011, ApJ, 727, 130
- Kriss G. A., Canizares C. R., Ricker G. R., 1980, ApJ, 242, 492

- Krolik J. H., Begelman M. C., 1988, *ApJ*, 329, 702
- Krongold Y., Nicastro F., Brickhouse N. S., Elvis M., Liedahl D. A., Mathur S., 2003, *ApJ*, 597, 832
- Lal D. V., Ho L. C., 2010, *AJ*, 139, 1089
- LaMassa S. M., Heckman T. M., Ptak A., Martins L., Wild V., Sonnentrucker P., 2010, *ApJ*, 720, 786
- Lamastra A., Bianchi S., Matt G., Perola G. C., Barcons X., Carrera F. J., 2009, *A&A*, 504, 73
- Laor A., 2003, *ApJ*, 590, 86
- Lawrence A., 1991, *MNRAS*, 252, 586
- Leahy D. A., Creighton J., 1993, *MNRAS*, 263, 314
- Liang E. P. T., 1979, *ApJ*, 231, L111
- Liang E. P. T., Price R. H., 1977, *ApJ*, 218, 247
- Lightman A. P., White T. R., 1988, *ApJ*, 335, 57
- Lobban A. P., Reeves J. N., Porquet D., Braito V., Markowitz A., Miller L., Turner T. J., 2010, *MNRAS*, 408, 551
- Lumsden S. L., Alexander D. M., 2001, *MNRAS*, 328, L32
- Magdziarz P., Zdziarski A. A., 1995, *MNRAS*, 273, 837
- Maiolino R., Rieke G. H., 1995, *ApJ*, 454, 95
- Maiolino R., Risaliti G., Salvati M., Pietrini P., Torricelli-Ciamponi G., Elvis M., Fabbiano G., Braito V., Reeves J., 2010, *A&A*, 517, A47
- Maiolino R., Salvati M., Bassani L., Dadina M., della Ceca R., Matt G., Risaliti G., Zamorani G., 1998, *A&A*, 338, 781
- Malkan M. A., Gorjian V., Tam R., 1998, *ApJS*, 117, 25
- Marconi A., Risaliti G., Gilli R., Hunt L. K., Maiolino R., Salvati M., 2004, *MNRAS*, 351, 169
- Marinucci A., Bianchi S., Matt G., Fabian A. C., Iwasawa K., Miniutti G., Piconcelli E., 2011, *A&A*, 526, A36+

## BIBLIOGRAPHY

---

- Marinucci A., Bianchi S., Nicastro F., Matt G., Goulding A. D., 2012, *ApJ*, 748, 130
- Marinucci A., Risaliti G., Wang J., Nardini E., Elvis M., Fabbiano G., Bianchi S., Matt G., 2012, *MNRAS*, 423, L6
- Martocchia A., Matt G., 2002, in I. Cagnoni ed., *Inflows, Outflows, and Re-processing around Black Holes On the nature of hidden broad line regions in Seyfert 2 galaxies*. pp 34–+
- Matt G., 2000, *A&A*, 355, L31
- Matt G., 2002, *MNRAS*, 337, 147
- Matt G., Bianchi S., D’Ammando F., Martocchia A., 2004, *A&A*, 421, 473
- Matt G., Fabian A. C., Ross R. R., 1993, *MNRAS*, 262, 179
- Matt G., Fabian A. C., Ross R. R., 1996, *MNRAS*, 278, 1111
- Matt G., Guainazzi M., Maiolino R., 2003, *MNRAS*, 342, 422
- Matt G., Perola G. C., Piro L., 1991, *A&A*, 247, 25
- Matt G., Pompilio F., La Franca F., 1999, , 4, 191
- McElroy D. B., 1995, *ApJS*, 100, 105
- Meléndez M., Kraemer S. B., Armentrout B. K., Deo R. P., Crenshaw D. M., Schmitt H. R., Mushotzky R. F., Tueller J., Markwardt C. B., Winter L., 2008, *ApJ*, 682, 94
- Merritt D., Ferrarese L., 2001, *ApJ*, 547, 140
- Miller J. S., Antonucci R. R. J., 1983, *ApJ*, 271, L7
- Miller L., Turner T. J., Reeves J. N., 2008, *A&A*, 483, 437
- Moran E. C., 2007, in L. C. Ho & J.-W. Wang ed., *The Central Engine of Active Galactic Nuclei Vol. 373 of Astronomical Society of the Pacific Conference Series, Spectropolarimetry Surveys of Obscured AGNs*. p. 425
- Moran E. C., Barth A. J., Kay L. E., Filippenko A., 2000, *ApJ*, 540, L73
- Narayan R., Yi I., Mahadevan R., 1995, *Nature*, 374, 623
- Nardini E., Risaliti G., 2011, *MNRAS*, 417, 2571

- Nelson C. H., Whittle M., 1995, *ApJS*, 99, 67
- Nenkova M., Sirocky M. M., Ivezić Ž., Elitzur M., 2008, *ApJ*, 685, 147
- Nicastro F., 2000, *ApJ*, 530, L65
- Nicastro F., Martocchia A., Matt G., 2003, *ApJ*, 589, L13
- Ogle P. M., Brookings T., Canizares C. R., Lee J. C., Marshall H. L., 2003, *A&A*, 402, 849
- Oliva E., Origlia L., Maiolino R., Moorwood A. F. M., 1999, *A&A*, 350, 9
- Osterbrock D., Ferland G. J., 2006, *Astrophysics of gaseous nebulae and active galactic nuclei*
- Osterbrock D. E., 1989, *Astrophysics of gaseous nebulae and active galactic nuclei*
- Otani C., Kii T., Reynolds C. S., Fabian A. C., Iwasawa K., Hayashida K., Inoue H., Kunieda H., Makino F., Matsuoka M., Tanaka Y., 1996, *PASJ*, 48, 211
- Panessa F., Bassani L., 2002, *A&A*, 394, 435
- Panessa F., Carrera F. J., Bianchi S., Corral A., Gastaldello F., Barcons X., Bassani L., Matt G., Monaco L., 2009, *MNRAS*, 398, 1951
- Pereira-Santaella M., Diamond-Stanic A. M., Alonso-Herrero A., Rieke G. H., 2010, *ApJ*, 725, 2270
- Perola G. C., Matt G., Cappi M., Fiore F., Guainazzi M., Maraschi L., Petrucci P. O., Piro L., 2002, *A&A*, 389, 802
- Peterson B. M., 2007, in Ho L. C., Wang J.-W., eds, *The Central Engine of Active Galactic Nuclei Vol. 373 of Astronomical Society of the Pacific Conference Series, The Masses of Black Holes in Active Galactic Nuclei*. p. 3
- Petrucci P.-O., Paltani S., Malzac J., Kaastra J. S., Cappi M., Ponti G., De Marco B., Kriss G. A., Steenbrugge K. C., Bianchi S., Branduardi-Raymont G., Mehdipour M., Costantini E., Dadina M., Lubinski P., 2012, *ArXiv e-prints*
- Piconcelli E., Jimenez-Bailón E., Guainazzi M., Schartel N., Rodríguez-Pascual P. M., Santos-Lleó M., 2004, *MNRAS*, 351, 161
- Pier E. A., Krolik J. H., 1992, *ApJ*, 399, L23

## BIBLIOGRAPHY

---

- Pogge R. W., 1988, *ApJ*, 328, 519
- Porquet D., Dubau J., 2000, *A&AS*, 143, 495
- Pounds K. A., Page K. L., 2005, *MNRAS*, 360, 1123
- Prieto M. A., Pérez García A. M., Rodríguez Espinosa J. M., 2001, *A&A*, 377, 60
- Pringle J. E., 1981, *ARA&A*, 19, 137
- Protassov R., van Dyk D. A., Connors A., Kashyap V. L., Siemiginowska A., 2002, *ApJ*, 571, 545
- Puccetti S., Fiore F., Risaliti G., Capalbi M., Elvis M., Nicastro F., 2007, *MNRAS*, 377, 607
- Reynolds C. S., 1997, *MNRAS*, 286, 513
- Reynolds C. S., 1999, in *ASP Conf. Ser. 161: High Energy Processes in Accreting Black Holes Compton Reflection and Iron Fluorescence in Active Galactic Nuclei and Galactic Black Hole Candidates*. pp 178—+
- Reynolds C. S., Fabian A. C., Nandra K., Inoue H., Kunieda H., Iwasawa K., 1995, *MNRAS*, 277, 901
- Reynolds C. S., Nowak M. A., 2003, *Phys. Rep.*, 377, 389
- Reynolds C. S., Ward M. J., Fabian A. C., Celotti A., 1997, *MNRAS*, 291, 403
- Rigby J. R., Diamond-Stanic A. M., Aniano G., 2009, *ApJ*, 700, 1878
- Risaliti G., 2002, *A&A*, 386, 379
- Risaliti G., 2011, *Memorie della Societa Astronomica Italiana Supplementi*, 17, 118
- Risaliti G., Elvis M., 2010, *A&A*, 516, A89
- Risaliti G., Elvis M., Bianchi S., Matt G., 2010, *MNRAS*, 406, L20
- Risaliti G., Elvis M., Fabbiano G., Baldi A., Zezas A., 2005, *ApJ*, 623, L93
- Risaliti G., Elvis M., Fabbiano G., Baldi A., Zezas A., Salvati M., 2007, *ApJ*, 659, L111
- Risaliti G., Elvis M., Nicastro F., 2002, *ApJ*, 571, 234



- Risaliti G., Miniutti G., Elvis M., Fabbiano G., Salvati M., Baldi A., Braito V., Bianchi S., Matt G., Reeves J., Soria R., Zezas A., 2009, *ApJ*, 696, 160
- Risaliti G., Nardini E., Salvati M., Elvis M., Fabbiano G., Maiolino R., Pietrini P., Torricelli-Ciamponi G., 2011, *MNRAS*, 410, 1027
- Risaliti G., Salvati M., Marconi A., 2011, *MNRAS*, 411, 2223
- Ross R. R., Fabian A. C., 1993, *MNRAS*, 261, 74
- Rush B., Malkan M. A., Spinoglio L., 1993, *ApJS*, 89, 1
- Sako M., Kahn S. M., Paerels F., Liedahl D. A., 2000, *ApJ*, 543, L115
- Sambruna R. M., Netzer H., Kaspi S., Brandt W. N., Chartas G., Garmire G. P., Nousek J. A., Weaver K. A., 2001, *ApJ*, 546, L13
- Sanders D. B., Phinney E. S., Neugebauer G., Soifer B. T., Matthews K., 1989, *ApJ*, 347, 29
- Schmidt M., 1963, *Nature*, 197, 1040
- Shakura N. I., Sunyaev R. A., 1973, *A&A*, 24, 337
- Shapiro S. L., Teukolsky S. A., 1983, *Black holes, white dwarfs, and neutron stars: The physics of compact objects*
- Shaw M., Wilkinson A., Carter D., 1993, *A&A*, 268, 511
- Shi Y., Rieke G. H., Smith P., Rigby J., Hines D., Donley J., Schmidt G., Diamond-Stanic A. M., 2010, *ApJ*, 714, 115
- Shu X. W., Wang J. X., Jiang P., Fan L. L., Wang T. G., 2007, *ApJ*, 657, 167
- Shu X. W., Yaqoob T., Wang J. X., 2011, *ApJ*, 738, 147
- Simpson C., 2005, *MNRAS*, 360, 565
- Smith R. K., Brickhouse N. S., Liedahl D. A., Raymond J. C., 2001, *ApJ*, 556, L91
- Stephens M. A., 1970, *Journal of the Royal Statistical Society. Series B (Methodological)*, 32, pp. 115
- Strüder L., Briel U., Dennerl K., Hartmann R., Kendziorra E., Meidinger N., Pfeffermann E., Reppin C., Aschenbach B., Bornemann W., Bräuninger H., Burkert W., Elender M., 2001, *A&A*, 365, L18

## BIBLIOGRAPHY

---

- Sunyaev R. A., Churazov E. M., 1996, *Astronomy Letters*, 22, 648
- Tadhunter C., Tsvetanov Z., 1989, *Nature*, 341, 422
- Terlevich E., Diaz A. I., Terlevich R., 1990, *MNRAS*, 242, 271
- Tombesi F., Cappi M., Reeves J. N., Palumbo G. G. C., Braitto V., Dadina M., 2011, *ApJ*, 742, 44
- Tombesi F., Cappi M., Reeves J. N., Palumbo G. G. C., Yaqoob T., Braitto V., Dadina M., 2010, *A&A*, 521, A57
- Tran H. D., 1995, *ApJ*, 440, 565
- Tran H. D., 2001, *ApJ*, 554, L19
- Tran H. D., 2003, *ApJ*, 583, 632
- Tran H. D., Miller J. S., Kay L. E., 1992, *ApJ*, 397, 452
- Tremaine S., Gebhardt K., Bender R., Bower G., Dressler A., Faber S. M., Filippenko A. V., Green R., Grillmair C., Ho L. C., Kormendy J., Lauer T. R., Magorrian J., Pinkney J., Richstone D., 2002, *ApJ*, 574, 740
- Trouille L., Barger A. J., 2010, *ApJ*, 722, 212
- Trump J. R., Impey C. D., Kelly B. C., Civano F., Gabor J. M., Diamond-Stanic A. M., Merloni A., Urry C. M., Hao H., Jahnke K., Nagao T., Taniguchi Y., Koekemoer A. M., Lanzuisi G., Liu C., Mainieri V., Salvato M., Scoville N. Z., 2011, *ApJ*, 733, 60
- Turner M. J. L., Abbey A., Arnaud M., Balasini M., Barbera M., Belsole E., Bennie P. J., Bernard J. P., Bignami G. F., Boer M., Briel U., Butler I., Cara C., Chabaud C., Cole R., Collura A., Conte M., Cros A., Denby 2001, *A&A*, 365, L27
- Vasudevan R. V., Fabian A. C., 2007, *MNRAS*, 381, 1235
- Vasudevan R. V., Fabian A. C., 2009, *MNRAS*, 392, 1124
- Walter R., Fink H. H., 1993, *A&A*, 274, 105
- Weaver K. A., Meléndez M., Mushotzky R. F., Kraemer S., Engle K., Malumuth E., Tueller J., Markwardt C., Bergeha C. T., Dudik R. P., Winter L. M., Armus L., 2010, *ApJ*, 716, 1151

- Wilson A. S., Tsvetanov Z. I., 1994, *AJ*, 107, 1227
- Wu Y., Zhang E., Liang Y., Zhang C., Zhao Y., 2011, *ApJ*, 730, 121
- Young M., Elvis M., Risaliti G., 2010, *ApJ*, 708, 1388
- Young S., Hough J. H., Efstathiou A., Wills B. J., Bailey J. A., Ward M. J., Axon D. J., 1996, *MNRAS*, 281, 1206
- Zdziarski A. A., Fabian A. C., Nandra K., Celotti A., Rees M. J., Done C., Coppi P. S., Madejski G. M., 1994, *MNRAS*, 269, L55
- Zheng W., Kriss G. A., Davidsen A. F., Lee G., Code A. D., Bjorkman K. S., Smith P. S., Weistrop D., Malkan M. A., Baganoff F. K., Peterson B. M., 1995, *ApJ*, 444, 632